DOT/FAA/AR-xx/xx

Federal Aviation Administration
William J. Hughes Technical Center
Aviation Research Division
Atlantic City International Airport
New Jersey 08405

The FAA's Center of Excellence for UAS Research
ASSURE
Alliance for System Safety of UAS through Research Excellence

Task A17: Airborne Collision Severity Evaluation – Engine Ingestion

Dr. Kiran D'Souza, A17 Principal Investigator – dsouza.60@osu.edu, Director of Nonlinear Dynamics and Vibration Lab, Associate Director of Gas Turbine Lab, The Ohio State University (OSU)

Dr. Gerardo Olivares, National Institute for Aviation Research (NIAR), Wichita State University (WSU) Principal Investigator – gerardo.olivares@wichita.edu, Director of Computational Mechanics and Crash Dynamics Lab, NIAR – WSU

Mr. David Arterburn, University of Alabama in Huntsville (UAH) Principal Investigator - arterbd@uah.edu, Director, Rotorcraft Systems Engineering and Simulation Center, (UAH)

11/07/2022

Final Report

This document is available to the U.S. public
through the National Technical Information
Services (NTIS), Springfield, Virginia 22161.

This document is also available from the
Federal Aviation Administration William J. Hughes
Technical Center at actlibrary.tc.faa.gov.

U.S. Department of Transportation
Federal Aviation Administration

NOTICE

This document is disseminated under the sponsorship of the U.S. Department of Transportation in the interest of information exchange. The U.S. Government assumes no liability for the contents or use thereof. The U.S. Government does not endorse products or manufacturers. Trade or manufacturers' names appear herein solely because they are considered essential to the objective of this report. The findings and conclusions in this report are those of the author(s) and do not necessarily represent the views of the funding agency. This document does not constitute FAA policy. Consult the FAA sponsoring organization listed on the Technical Documentation page as to its use.

This report is available at the Federal Aviation Administration William J. Hughes Technical Center's Full-Text Technical Reports page: actlibrary.tc.faa.gov in Adobe Acrobat portable document format (PDF).

Legal Disclaimer: The information provided herein may include content supplied by third parties. Although the data and information contained herein has been produced or processed from sources believed to be reliable, the Federal Aviation Administration makes no warranty, expressed or implied, regarding the accuracy, adequacy, completeness, legality, reliability or usefulness of any information, conclusions or recommendations provided herein. Distribution of the information contained herein does not constitute an endorsement or warranty of the data or information provided herein by the Federal Aviation Administration or the U.S. Department of Transportation. Neither the Federal Aviation Administration nor the U.S. Department of Transportation shall be held liable for any improper or incorrect use of the information contained herein and assumes no responsibility for anyone's use of the information. The Federal Aviation Administration and U.S. Department of Transportation shall not be liable for any claim for any loss, harm, or other damages arising from access to or use of data or information, including without limitation any direct, indirect, incidental, exemplary, special or consequential damages, even if advised of the possibility of such damages. The Federal Aviation Administration shall not be liable to anyone for any decision made or action taken, or not taken, in reliance on the information contained herein.

Technical Report Documentation Page

1. Report No. FAA A11L.UAS.58	2. Government Accession No.	3. Recipient's Catalog No.
4. Title and Subtitle Task A17: Airborne Collision Severity Evaluation – Engine Ingestion 2018-2022		5. Report Date (month and year printed) 6. Performing Organization Code ASSURE: OSU
7. Author(s) Professor Kiran D'Souza, The Ohio State University (OSU) Dr. Gerardo Olivares, National Institute for Aviation Research (NIAR) Mr. David Arterburn, University of Alabama in Huntsville (UAH)		8. Performing Organization Report No.
9. Performing Organization Name and Address The Ohio State University Aerospace Research Center 2300 West Case Road Columbus, OH 43235		10. Work Unit No. (TRAIS) 11. Contract or Grant No.
12. Sponsoring Agency Name and Address U.S. Department of Transportation Federal Aviation Administration Office of Aviation Research Washington, DC 20591		13. Type of Report and Period Covered Final Report 14. Sponsoring Agency Code 5401

15. Supplementary Notes

The Federal Aviation Administration Aviation William J. Hughes Technical Center Research Division COR was

16. Abstract

The A17 study completed three main tasks: (1) creating a fan assembly model with a fan having representative structural features of a high bypass ratio fan commonly used in aircraft engines for commercial transport; (2) validating the UAS model developed in A3 with experiments that are representative of a UAS being ingested into an engine; and (3) using the representative fan assembly model and validated UAS model to conduct a number of simulations to understand what the interaction of the fan and UAS will look like in an engine ingestion scenario for a variety of cases. Based on the findings the research team concluded that the rotational speed of the fan is the critical parameter in the ingestion with higher speeds leading to significantly more damage. The second most important parameter is the location along the radial span with the outer radial impact leading to more damage to the fan. The relative translational velocity and orientation of the UAS during the impact do play a role in the damage sustained to the fan, but are much less significant. Significant damage to the fan was sustained in many of the conditions studied in this work; however, with regards to fan damage, all cases were within the engine certification envelope.

17. Key Words Crashworthiness, Engine Ingestion, UAS, Ohio State University, OSU	18. Distribution Statement This document is available to the U.S. public through the National Technical Information Service (NTIS), Springfield, Virginia 22161. This document is also available from the Federal Aviation Administration William J. Hughes Technical Center at actlibrary.tc.faa.gov.

19. Security Classif. (of this report) Unclassified	20. Security Classif. (of this page) Unclassified	21. No. of Pages	22. Price

Form DOT F 1700.7 (8-72) Reproduction of completed page authorized

ACKNOWLEDGEMENTS

The following researchers in addition to the respective university Principal Investigators shown on the title page have made fundamental contributions to the content. The individuals who supported the work from The Ohio State University include: post doctoral researchers Dushyanth Sirivolu and Eric Kurstak; graduate student Troy Lyons; and undergraduate researchers Mitchell Wong, Keaton Nichols, Freeman Gao, and Tony Kuenzli. Individuals from National Institute for Aviation Research who supported the work include Luis Gomez and Hoa Ly. Finally, the individuals from University of Alabama Huntsville who supported the work include Chris Duling, Mark Zwiener, and Zach Perrin.

The A17 team would also like to recognize the valuable contributions of the industry participants that supported this project with the development of the fan model, technical support and guidance throughout the project: Nick Kray from GE Aviation, Steve Conner from Pratt & Whitney, Costas Vogiatzis and Cheikh Cissé from Honeywell, James Finlayson and Julian Reed from Rolls Royce, and Duane Revilock from NASA Glenn.

The authors would like to acknowledge the FAA's Center of Excellence for Unmanned Aircraft Systems, ASSURE, for supporting this work. The A17 team also recognizes the vital importance of the leadership at ASSURE in the completion of this project. Steve Luxion and Hannah Thach with the ASSURE Leadership have been strong supporters of the team throughout this project and participated actively in a number of events.

The authors would also like to acknowledge the Ohio Super Computer Center[1] and the OSU SimCenter, which provided additional computing resources used to run the simulations presented in this work.

Finally, the A17 team would like to thank all the FAA personnel that have been involved in this research project. In particular, the authors would like to thank Sabrina Saunders-Hodge, Hector Rea, Nick Lento, Jorge Fernandez, and Melanie Flavin for their support throughout the project.

TABLE OF CONTENTS

LIST OF FIGURES

LIST OF TABLES

LIST OF ACRONYMS

ARF	Aerophysics Research Facility
ASSURE	Alliance for System Safety of UAS through Research Excellence
AWG	LS-DYNA Aerospace Working Group
CAD	Computer-Aided Design
DIC	Digital Image Correlation
EO	Engine Order
FAA	Federal Aviation Administration
FBO	Fan Blade Out
FE	Finite Element
LE	Leading Edge
NIAR	National Institute for Aviation Research
OEM	Original Equipment Manufacturer
OSU	The Ohio State University
RPM	Revolutions per Minute
UAH	University of Alabama, Huntsville
UAS	Unmanned Aerial System
UAV	Unmanned Aerial Vehicle
WSU	Wichita State University

EXECUTIVE SUMMARY

The A17 Airborne Collision Severity Evaluation – Engine Ingestion research built off the small engine ingestion study in the A3 project that used a generic mid-sized business jet fan assembly model and the Unmanned Aerial System (UAS) model developed for the airborne collision work. The A17 study focused on three main tasks: (1) creating a fan assembly model with a fan having representative structural features of a high bypass ratio fan commonly used in aircraft engines for commercial transport; (2) validating the UAS model developed in A3 with experiments that are representative of a UAS being ingested into an engine; and (3) using the representative fan assembly model and validated UAS model to conduct a number of simulations to understand what the interaction of the fan and UAS will look like in an engine ingestion scenario for a variety of cases. The A17 team consisted of The Ohio State University (OSU), the National Institute for Aviation Research (NIAR) at Wichita State University (WSU) and the University of Alabama in Huntsville (UAH).

OSU worked with industrial partners to complete the first task. The industrial partners provided a model of an industrial fan blade and disk that had been scaled to the desired size and removed of certain proprietary aerodynamic features. OSU worked with the industry partners to define the rest of the fan assembly (i.e., blade retention mechanisms, casing, nose cone, and shaft) to provide appropriate boundary conditions for the fan and UAS during the ingestion event. Also, OSU carried out a series of dynamic and structural simulations (e.g., bird ingestion) to ensure the fan assembly model is representative of the structural and vibratory characteristics of current fans that are certified for flight. NIAR and UAH completed the second task. UAH was responsible for conducting a series of experiments launching key UAS components (i.e., motor, camera, battery) and the full UAS at titanium test articles representative of a UAS being sliced by fan blades at the outer radius. These test articles were stationary and the UAS components had to be launched at over 700 knots at a precisely controlled point to obtain the needed data. NIAR used the experimental data to update and validate the computational model of the key UAS components and the full UAS model. OSU worked with the industrial partners to complete the third task. Several ingestion simulations were carried out to understand which parameters are most important in the ingestion with respect to damage and imbalances in the fan, energy imparted to the casing, and forces on the retention systems. The studied ingestion parameters include rotational speed of the fan, relative translational velocity of the UAS, impact location on the fan, and orientation of the UAS. The sensitivity study enabled the selection of potential worst case impact cases for different phases of flight.

Based on the findings the research team concluded that the rotational speed of the fan is the critical parameter in the ingestion with higher speeds leading to significantly more damage. The second most important parameter is the location along the radial span with the outer radial impact leading to more damage to the fan. The relative translational velocity and orientation of the UAS during the impact do play a role in the damage sustained to the fan but are much less significant. Significant damage to the fan was sustained in many of the conditions investigated in this work; however, no case study produced damage, or structural loads, that exceeded the current worst case certification requirements of a fan blade out event.

The research has also improved the UAS model for specific engine ingestion conditions. Also, the model can be used by industrial partners to study ingestions with their own proprietary models. Moreover, it has led to the development of a representative fan rig model that can be used to investigate the ingestion of various foreign objects (birds, ice slabs, etc.).

1. BACKGROUND

There has been a significant increase in the use of UASs in recent years. As the number of UASs sold continues to increase, proper integration of UASs into the airspace is a major safety concern due to potential UAS-airplane collisions. Recreational users are the highest safety concern since they may be unaware or unconcerned with regulations and rules on restricted operation of their devices in certain airspaces. These UASs tend to be relatively small and have the potential to be ingested into an engine. There is a considerable body of knowledge related to bird and ice ingestions (*soft* FOD – foreign object debris) into engines; however, there is much less information about *harder* objects being ingested into engines. This research effort is focused on investigating the effects of the harder components of UASs (i.e., motor, battery, and camera) in particular during an ingestion event.

Earlier studies performed by the Alliance for System Safety of UAS through Research Excellence (ASSURE) that provided the direction of the A17 Airborne Collision Severity Evaluation – Engine Ingestion research was given in the A3 Airborne Collision Severity Evaluation work[2, 3]. This previous work involved the development of a computational model of a quadcopter that was validated by a series of static and dynamic experiments including blunt impacts of quadcopter components against aluminum plates[2]. Ingestion simulations were conducted with this quadcopter model into a generic mid-sized business class fan assembly model that was not copied from any particular OEM design[3, 4]. While the funding and scope of this initial study was limited, the study did show that UAS cause more damage than birds of similar size and the need for keeping UAS away from manned aircraft.

Following the Federal Aviation Administration (FAA) sponsored Peer Review, a workshop was held at OSU with ASSURE team members, FAA and the National Aeronautics and Space Administration personnel, and industrial partners to define the key research questions that need to be addressed in the next phase of the research. The key research questions identified in this study are: (1) to understand what the interaction of an Unmanned Aerial Vehicle (UAV) with a representative high bypass ratio fan (typically used in large commercial transport) will look like, and (2) to define best practices and fan models for use in further studies. Addressing these questions can: (i) facilitate the development of mitigation strategies including procedures, training, etc., but not the new development nor any changes to existing engine certification standards; (ii) lead to understanding of critical design features of UAVs to possibly influence design procedures in this nascent industry; and (iii) provide an open source fan model for further studies. Additionally, a critical point analysis will be carried out on a representative fan model to determine the sensitivity of blade failure and energy imparted to a containment case to different impact scenarios. Moreover, determining the worst case scenarios will give industry a starting point to focus on when conducting an analysis with their proprietary models.

2. SCOPE

The research was conducted over a four-year period and included peer reviews at the beginning of the research and after completion of final reports at the end of the research program. The research was broken into three main research tasks, which were each subdivided into several sub-tasks in order to answer the key research questions.

2.1 TASK A: CREATE A REPRESENTATIVE HIGH BYPASS RATIO FAN MODEL (OSU, INDUSTRY)

The objective of this task was to develop a fan model that has representative structural and vibratory features of a modern high-bypass ratio fan. The model has a diameter of 62 inches and uses solid titanium blades. Industry experts worked with OSU to develop the fan model and ensure that the blade geometry, structural and vibratory properties meet the standards of current industrial fans of this size. It was a scaled version of a previous design, so some aerodynamic features are present but some proprietary aerodynamic features are removed. In addition to the fan model, an appropriate casing and nose cone geometry were developed in collaboration with the industrial partners to study the interaction with fan elements and the UAS during the collision. An appropriate initial test matrix for UAS ingestion simulations was also determined as a part of this task.

Research Questions

1. What are the key vibratory features of a representative modern high-bypass ratio fan that is structurally operational?
2. What range of rotational velocities would be experienced by the fan modeled in this project?
3. What type of UAS ingestion simulations should be performed with this fan model to complete a critical point analysis of the ingestion event?

Assumptions and Limitations - The research assumed the following operating limitations:

1. The representative fan model has not been constructed nor is it currently used in the fleet.
2. The fan model will be representative of the structural properties of a modern high-bypass ratio fan, but not the aerodynamic features nor the aeroelastic response.
3. Material models used for the fan model will be from previously developed FAA or open-source material models of titanium and will not be generated in this project. The manufacturing process determines the plastic and failure properties of titanium alloy material[5]. For a ¼ inch Ti-6Al-4V plate, material anisotropy may vary the plastic and failure behavior. Due to material model availability, an isotropic model will be considered in this study.
4. Fan rig assembly model does not contain most of the downstream components of the fan (i.e., compressor, combustor and turbine), and therefore any damage in these components is outside the scope of this research.

2.2 TASK B: EXPERIMENTAL VALIDATION OF COMPONENT AND FULL QUADCOPTER MODEL (UAH, WSU)

The objective of this task was to conduct individual components (camera, motor, and battery) and full quadcopter model collision testing with titanium wedges, and update an existing UAS quadcopter model[2] accordingly. Impact tests were conducted in the range of 425-710 knots on an angled titanium plate to obtain contact conditions similar to an engine ingestion. Fully charged batteries were used in this study to provide some insight on potential fire hazards during an ingestion. Finite Element (FE) models developed in the previous FAA project[2] for individual components and the full quadcopter model were used in this research project. An appropriate mesh size to be used for FE simulations of the ingestion was also suggested based on the experiments and computational modeling. Simulations to confirm integration of the UAS model with the fan model developed in Task A were also conducted.

Research Questions

1. What modifications are needed for the quadcopter components (the motor, camera, or battery) and full quadcopter models for higher speed slicing impacts into titanium?
2. What velocities should be used in the experiments, to capture the relative velocities in an ingestion event (considering the fan rotational velocity, airspeed of the airplane, and velocity of the quadcopter)?
3. How can the full quadcopter be accelerated to the desired speed and should the quadcopter components be tested at a higher speed?

Assumptions and Limitations - The research assumed the following operating limitations:

1. Procurement of materials and manufacturing of titanium wedges will be dependent on initial fan design.
2. Fan model from Task A will be completed for integration with the UAS model.

2.3 TASK C: SENSITIVITY ANALYSIS OF PARAMETERS TO THE INGESTION (OSU)

The objective of this task was to conduct numerical simulations to understand the effect of various parameters on the ingestion event. FE simulations were carried out in LS-DYNA and included a fixed fan model with blades rotating at a prescribed speed. The dynamics, stresses, and element failure in the fan were studied during the ingestion simulations. Additionally, impact energies on the casing, imbalance loads on the shaft, and forces on the retention systems were determined during the ingestion simulations. The simulations were used for a critical point analysis to understand which parameters lead to the worst outcomes.

Research Questions:

1. What are the important parameters for UAS ingestions (i.e., fan speed, orientation of impact)?
2. What are the worst-case scenarios for a critical point analysis?

Assumptions and Limitations - The research assumed the following operating limitations:

1. The representative fan model will be one data point for understanding the interaction of the fan and the UAS, and will not capture all the configurations used in the fleet for modern high-bypass ratio fans.
2. The nose cone is used to capture the boundary conditions of the ingestion event and will be rigid during the simulations.
3. The casing will not be used to assess containment, rather it will be used to setup the boundary conditions for the ingestion and assess the expected loads on the containment casing.
4. There is no validation experiment of the quadcopter with the actual fan at the operating conditions.
5. Aeroelastic effects due to fan damage will not be assessed.
6. The simulations are dependent on the completion of Tasks A and B.

3. OVERVIEW OF RESEARCH

The research was carried out in close collaboration with engine industry manufacturers to create FE models that will capture critical features of a UAV-fan impact. Wherever feasible, the FE models were developed with pre-existing material models to leverage past work in the field. Also, the UAS model was shared with industry partners to maximize the impact of the research. The ingestion simulations were carried out in LS-DYNA (a finite element analysis software specialized in highly nonlinear transient dynamic analysis) for a variety of impact scenarios that were determined in consultation with industry partners and the FAA management team. The ingestion scenarios were simulated following the best practices set forth by the LS-DYNA Aerospace Working Group[6] (AWG).

3.1 TASK A

The objective of this task was to create a fan model that has representative structural and vibratory features of a modern high-bypass ratio fan (commonly used in commercial transport). This task was carried out in close collaboration with engine industry manufacturers to maximize its utility. To this end, a series of workshops and teleconferences were arranged at various stages of the development of the model.

The developed fan model is representative of certain features (structural and vibratory) of a modern high-bypass ratio fan but does not match a specific fan currently in the fleet. It has a diameter of 62 inches and uses solid titanium blades. The blade geometry was defined with industry to ensure that its characteristics (thickness of blade, angle of blade from root to tip, etc.) are representative of current industrial fans of this size. The blade material used a *MAT_224 TI-6Al-4V model that was developed and validated with a series of experiments in a previous FAA project[5]. The model was also analyzed to ensure that it captures the critical structural and vibratory features of a representative high-bypass ratio fan during foreign object ingestion (i.e., checking the modal properties of the fan, pre-stress of the fan at operating speeds, and response to bird ingestions). Experts from the industrial collaborators provided feedback on the reasonableness of the model simulations with past experience as well as comparisons with past published works[7, 8].

The other key components of the fan model were the fan containment ring and nose cone. The purpose of the inclusion of these components was to understand how they interact with the fan and UAV during the collision. However, due to the myriad of architectures for these components a representative structure is not truly feasible. Therefore, these models were designed to have reasonable geometries for the representative fan but remained linear elastic without failure. The reasonable geometries and elastic material models provide appropriate boundary conditions for the fan during the ingestion of the UAV for this short duration impact, and enabled the computation of the expected loads on these parts. This allowed for the determination of ingestion scenarios where the greatest energy and/or strain was imparted to these components and will enable industry to focus on these ingestion scenarios when using their actual proprietary designs.

3.2 TASK B

The objective of this research task was to conduct component level tests on the key quadcopter components (battery, motor, and camera) as well as full quadcopters and to validate the corresponding FE models at conditions that would occur in an engine ingestion. The quadcopter was chosen based on the availability of a partially validated FE model developed in a previous FAA project[2], which was originally chosen based on its popularity at the time. The quadcopter component models were previously validated at lower speeds from 100 to 250 knots with blunt force impacts against thin aluminum plates that were representative of the skin of an airplane. In contrast, the impact speeds during an engine ingestion could be much higher, surpassing 700 knots, and would be a slicing impact as opposed to a blunt force impact.

The validation tests were designed to be representative of a variety of component and full quadcopter impacts during an engine ingestion. The three UAV components and full quadcopter were launched at multiple speeds in the range of 425-710 knots. Instead of blunt flat plate impacts, the components impacted angled Ti-6Al-4V plates with similar thickness to the fan blade to validate the deformation at the expected conditions during an ingestion. The batteries were launched in a fully charged state to assess the likelihood of a fire in a slicing impact. The plates were held at the bottom during the experiments to mimic the connection of a blade to the disk. The experiments were filmed with a high-speed camera to measure the projectile state (i.e., velocity, and orientation) prior to impact, which enabled the simulations to accurately replicate experimental impact conditions. Furthermore, additional load information was measured for the validation of the computational simulations; including: strain gauges on the Ti-6Al-4V plates, load cells on the test stand, and Digital Image Correlation (DIC) on the front and back of the Ti-6Al-4V plates.

The data from the experiments were collected and analyzed to update the key UAV component level models and the integrated full UAV model. The possibility of a fire from the UAV battery during an ingestion was also considered. Additionally, the mesh sizing of the titanium plate was investigated during these component impacts. This investigation helped choose the appropriate mesh size of the fan blades in the region of the impact to maximize fidelity while minimizing computational cost.

WSU leveraged lessons learned from the first phase of the airborne collision work[2], as well as additional tests that occurred in the rotorcraft research for A16 UAS Airborne Collision Severity Evaluation – Rotorcraft Structural Impact. In particular, for the rotorcraft work, WSU and UAH conducted additional component impacts against aluminum panels and full aircraft tests with the UAS against helicopter components at velocities up to 500 knots. The final quadcopter numerical model that was used in this project included all these updates.

3.3 TASK C

The objective of this research task was to conduct a series of ingestion simulations to understand the effect of various parameters on the ingestion event. The ingestion simulations were conducted in LS-DYNA using the updated validated UAV model developed from tests with similar conditions to what is expected in an engine ingestion and described in Section 3.2 Task B. The fan model into which the UAV was ingested is discussed in Section 3.1 Task A, and the mesh sizing in the impact areas were informed by the quadcopter tests discussed in Section 3.2 Task B. For each of the ingestion simulations, failure of elements in the fan was captured, and expected strain and impact energies were obtained for the casing (using linear elastic models with no failure).

The ingestion simulation consisted of the fan model that is fixed in space with the fan rotating at a prescribed speed, which did not slow down during the course of this relatively short ingestion simulation. The deformation and stresses in the fan due to the centrifugal loading were accounted for by running an implicit dynamic relaxation on the rotating fan model. The UAV model was given the relative velocity of the plane and UAV, and directed at a specific location of the fan with a specified orientation.

The parameters of the ingestion that were investigated included the rotational speed of the fan, the relative translational velocity of the UAV with respect to the plane, the orientation of the UAV during the impact, and the radial location of the UAV impact along the fan. Additional simulations were explored based on the initial findings. The data from the ingestions focused on the failure in the elements of the fan model and the fan's plastic deformation as well as the energy imparted to the casing during the ingestion. The simulations were carefully monitored to ensure the validity of the results. Particular care for the contact modeling as well as monitoring the energy of the individual components to ensure the accuracy of the simulations.

The results from these simulations helped determine a parameter space where one can decide which ingestion parameters lead to the worst outcome for the fan blades, fan disk, or containment. The data points for the blade out and bird ingestion simulations for this specific fan model provide additional data points of events that have been extensively researched.

4. ORGANIZATION OF THIS REPORT

The report is organized with a cover report and separate university reports that are Annexes to the cover report. The cover report summarizes the collective research results of the entire research team and the university reports detail the individual research efforts of each university.

4.1 COVER REPORT

The cover report summarizes the results of the overall research effort for Task A17 and highlights the most important conclusions and recommendations. All tests and research were conducted as a Task A17 team in accordance with Section 2 and Section 3 and were approved by the FAA. Reviews of data and analysis were conducted monthly at technical interchange meetings with the FAA and industry experts. A peer review of the data was conducted with the principal researchers from each of the universities on 10 January 2023. Members of the FAA and industry experts participated in this review to identify specific issues or concerns related to the development of test data and the assessment of conclusions and recommendations. The cover report is not intended to serve as a cross reference for all the available data within the report but to summarize the most important results and identify the reports that contain more detailed information by reference to the respective university annexes.

4.2 INDIVIDUAL UNIVERSITY REPORTS

Individual university reports provide the contributions of each university to the overall task A17 research. The university reports provide specific details regarding the computational simulations, experimental methods and data, and data analysis conducted by the respective universities without a broad discussion of how results and analysis may complement the details of another university's report. Individual university reports are arranged in Annexes to the cover report and enable each university to use their respective report formats. Moreover, each university was responsible for their own internal peer reviews in accordance with their respective university policy.

5. REPRESENTATIVE HIGH BYPASS RATIO FAN MODEL FOR FOREIGN OBJECT INGESTION

One of the key objectives of this research program is to create an open fan model that has representative structural and vibratory features of modern high-bypass ratio fans (typically used in commercial transport). This open fan model can then be used in this study to investigate UAV impacts with fans and could also be used in future computational investigations. The fan was not designed to match the aerodynamic features nor the aeroelastic response of modern engines. This task was carried out in close collaboration with engine Original Equipment Manufacturers (OEMs) to maximize its utility. Other key components of the fan-rig model were also created in close collaboration with industry and these include: the fan containment ring, nose cone, shaft, and blade retention systems. The purpose of the inclusion of these components is to provide reasonable boundary conditions for the fan and UAV interactions during the collision. They will provide additional insights into the expected forces and energies that are transmitted into these systems. However, trying to determine failure in components outside of the UAV and fan blade/disk is not a focus of this fan rig model.

5.1 JUSTIFICATION

There are a variety of fan designs that have been created for a number of engine architectures and each engine OEM tends to have their own preferences and designs. The type of fan chosen for this work consists of solid titanium blades, which all OEMs have familiarity with, and are appropriate for the 1.57 m (62 in) fan diameter.

The fan geometry was created from scaling a smaller fan geometry up to the 1.57 m (62 in) fan diameter and removing proprietary features that were related to the aerodynamics and not the structural properties of the fan. Since building a truly representative containment ring and nose cone is not feasible due to the myriad of existing architectures, these models were included only to provide appropriate boundary conditions for the ingestion. The containment ring and nose cone models were designed with input from engine OEMs to have reasonable geometries for this representative fan. The containment ring was modeled with a linear elastic material with no failure to understand the expected loads it might encounter. The shaft was modeled as a rigid body.

5.2 Computer-Aided Design (CAD) MODELS

5.2.1 Representative Fan Geometry

The generic fan developed for this project is representative of the structural and vibratory properties of a modern high bypass ratio fan commonly used for commercial transport. The fan diameter is 1.57 m (62 in). The fan assembly includes an airfoil, dovetail, retainer, retention ring, disk, and disk flange, which are all shown in Figure 1. In these types of fans, the airfoil and dovetail are a single unit, called a blade, that can be pulled out of their slot in the disk and replaced if damage or failure occurs (e.g., after a bird strike). A total of 24 blades were used in this representative fan model. Due to the nature of the disk flange, a two blade model is needed to define a single cyclic sector model; therefore there are 12 cyclic sectors that are repeated to form the 24 blade model.

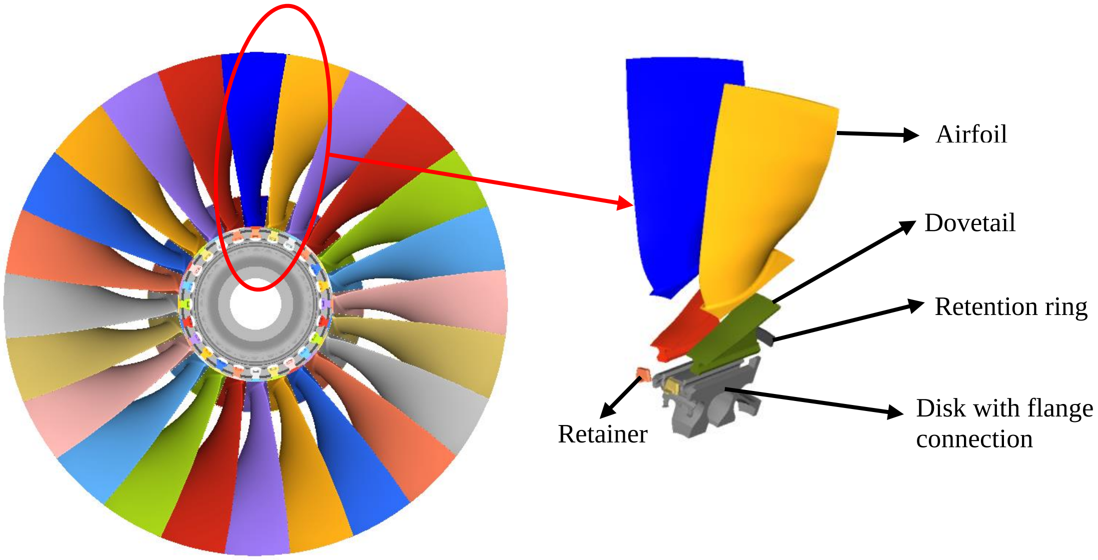

Figure 1. Components of the representative fan model.

The airfoil retainer is used to secure the dovetail into the disk after it is installed. This retainer prevents the blade from moving forward in the axial direction. The retention ring, which is connected to the disk on the rear side of the fan, prevents the blades from sliding axially further than intended. The flange on the front of the disk provides a way to bolt the nose cone to the disk. Due to the design of the flange, a cyclic symmetric model of the fan requires two blades instead of one, which corresponds to including one full bolt hole and two half holes in the flange.

The radial distance from the root of the disk to tip of the airfoil is 693 mm (27.3 in). The root of the airfoil is on an incline causing the radial span at the Leading Edge (LE) (549 mm) to be larger than the radial span at the trailing edge (442 mm) of the airfoil, as shown in Figure 2.

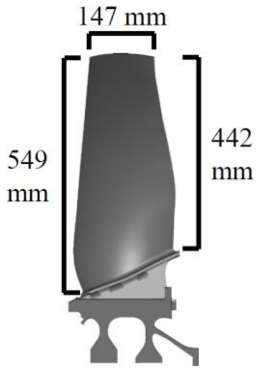

Figure 2. Side profile of blade with airfoil dimensions.

5.2.2 Casing

Engine fans are contained within a casing to optimize airflow through the engine, protect the engine from foreign object debris, and contain fan blades during a blade-out event or other engine failure. The casing used for the fan assembly model created in this project is shown in Figure 3 and has a total length of 1.580 m (62.2 in) and an internal diameter of 1.586 m (62.44 in). A hot clearance (i.e., clearance when the fan is spinning at its nominal rotational speed) of 3.81 mm (0.15 in) is used between the airfoil and the internal diameter of the casing. The thickness of the casing at the inlet and outlet is 4.1 mm (0.16 in).

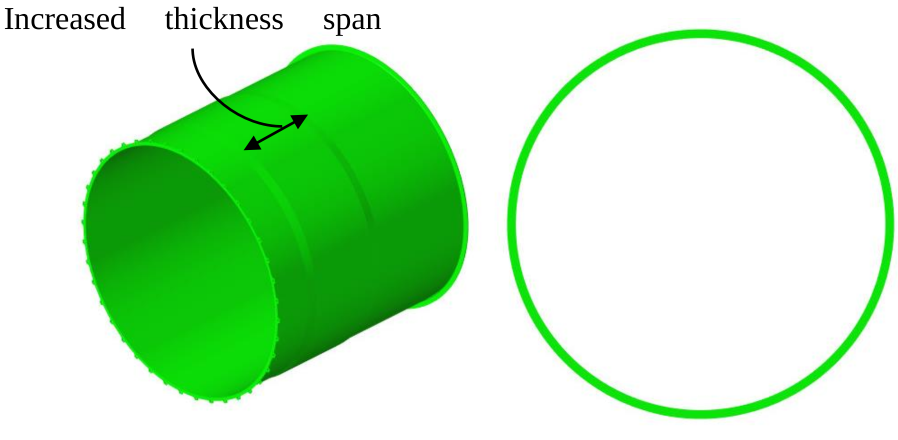

(a) (b)

Figure 3. Fan casing (a) isometric view, and (b) front view.

The portion of the casing around the fan is designed to withstand a fan blade-out event to protect the aircraft in the event of a blade failure. The containment design often starts with an energy balance approach[6, 9, 10] to calculate the minimum thickness of the casing in the impact region. Engine manufacturers have a variety of containment architectures for different engine types and sizes with the intent of maximizing durability while minimizing weight. The engine manufacturers generally design the casing using their proprietary architectures and proprietary material models and run simulations in nonlinear transient dynamic simulation tools, like LS-DYNA, to build confidence in the design before bench tests and full certification tests are conducted on a prototype. In this model, the primary purpose of the casing is to provide an appropriate boundary condition for the fan to capture first order effects of the UAS ingestion, while also maximizing the parameter space for how the ingestions can occur (i.e., not having an inlet smaller than the fan diameter, which would restrict the UAV's entry into the engine). For this reason, the casing thickness around the fan was determined using the energy balance approach[6, 9, 10], which is detailed in Annex A[11].

5.2.3 Nose Cone

The type of nose cone selected for the representative fan assembly model is a bi-conic like design, shown in Figure 4. The nose cone was modeled as aluminum, which is consistent with previous UAV engine ingestion work[3] and is a representative light weight material often used in aeronautical applications. The forward cone has a length L_1 = 211.4 mm (8.3 in) and a base radius

R_1 = 182 mm (7.16 in), and is stacked on a frustum of a cone of length L_2 = 115.5 mm (4.47 in) and base radius of R_2 = 239.5 mm (9.42 in). The overall thickness of the nose cone is 2.5 mm (0.1 in), a clearance of 2.5 mm is maintained between the nose cone and the dovetail region, and a tip radius of 2.5 mm is used. The nose cone is rigidly connected to the fan assembly through 24 bolt connections at the disk flange located on the front of the fan.

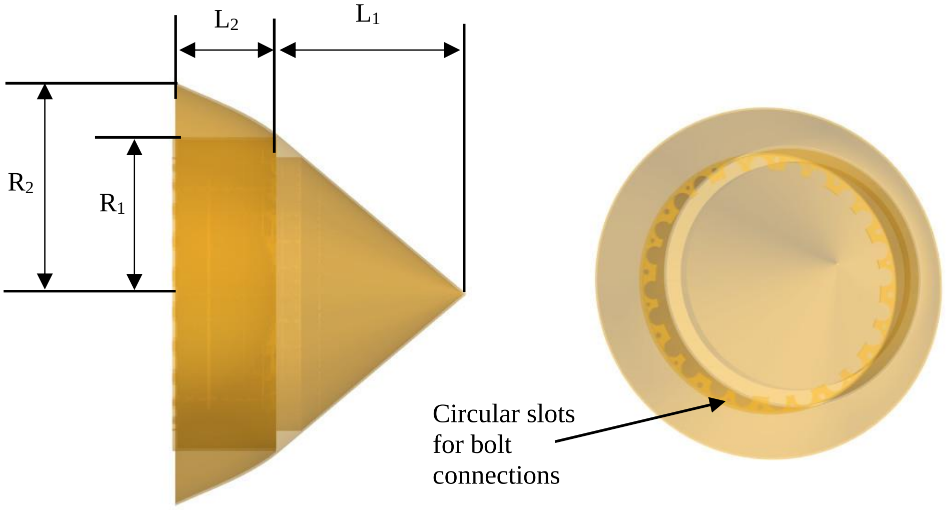

(a) (b)

Figure 4. (a) Side view of the biconic nose cone (b) front oblique transparent view of biconic nose cone.

5.2.4 Shaft

The low-pressure shaft connects the fan to the low-pressure turbine to form the low-pressure spool of the engine. The low-pressure turbine extracts energy from the flow to drive the fan through the low-pressure shaft. The CAD model for the shaft was based on drawings of the CFM56[12], a high bypass ratio turbofan. The shaft was modeled with a steel that is representative of the shaft material often used in turbofan engines. The cylindrical shaft had a total length of 0.915 m (36 in) and is shown in Figure 5. The shaft has an internal diameter of 83.8 mm (3.3 in) and a thickness of 5 mm (0.2 in) along the majority of its length. There was a rapid expansion in diameter towards the forward face of the shaft where it meets the disk. The outer diameter of the front face of the shaft is 241.9 mm (9.5 in) and the holes on this face have a diameter of 18 mm (0.7 in).

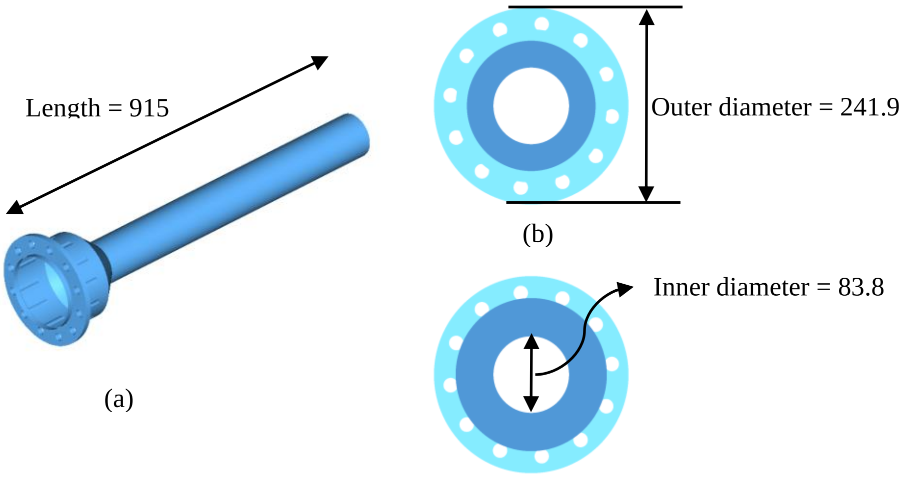

(a)

(b)

(c)

Figure 5. Shaft (a) isometric (b) front and (c) back views.

5.3 FINITE ELEMENT MODELS

5.3.1 Fan Assembly

The fan assembly is composed of the disk, disk flange, dovetail, airfoil, retainer, and retention ring. The disk, disk flange, and retention ring are treated as single contiguous parts while the dovetail, airfoil, and retainer are repeated parts for each of the 24 fan blades.

The disk, dovetail, airfoil, and retention ring are composed of a titanium alloy (Ti-6Al-4V) and were modelled using the *MAT_TABULATED_JOHNSON_COOK (*MAT_224) material model in LS-DYNA. The retainer is also composed of the same titanium alloy but was modelled as elastic using the *MAT_ELASTIC keyword. Material information for the Ti-6Al-4V alloy was obtained from a publicly available material model created in previous FAA projects[5, 13] and made available by the AWG [14, 15].

All components of the fan assembly were meshed using solid hexahedron elements and defined with a constant stress solid element (ELFORM=1) in their section cards. This under-integrated element formulation has the consequence of nonphysical, zero-energy modes of deformation called hourglass modes. To inhibit these hourglass modes there exist algorithms in LS-DYNA that can be invoked using the *HOURGLASS keyword. Each part with constant stress solid elements also had hourglass control defined with the type IHQ = 6 and the coefficient QM = 0.1.

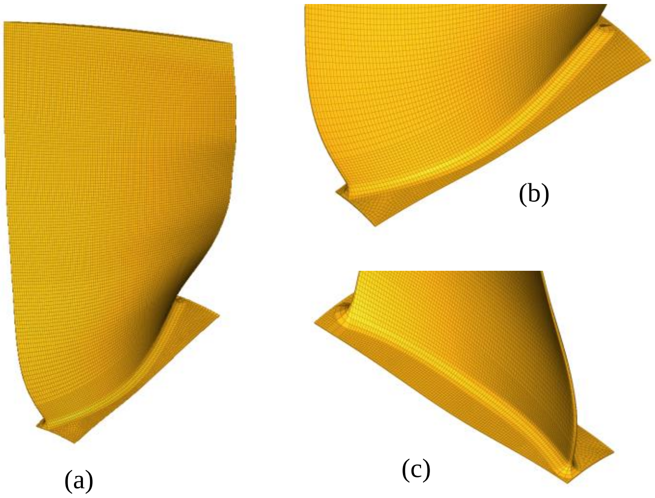

Figure 6. Airfoil mesh with three elements through the thickness (a) isometric view (b) suction side of the airfoil root and (c) pressure side of the airfoil root.

A key consideration in constructing the mesh for the model is the level of refinement in the mesh. In particular, the level of refinement in the mesh airfoils where the UAV impacts is of utmost importance. A refinement study was conducted to determine the level of refinement in the airfoils to reach convergence from models of the angled titanium wedges used for the validation of the UAS model. The results of this refinement study are included in the Appendix B of Annex A[11]. Note that during the validation of the UAS model (detailed in Annex B[16]) with the experimental data (discussed in Annex C[17]), it was determined that three elements through the thickness of the airfoil was optimal for matching the mesh of the airfoil with the mesh of the UAV model (as discussed in the appendix to Annex B[16]). A mesh of the airfoil with part of the platform is shown in Figure 6.

The mesh of the dovetail and blade platform is shown in

Figure 7. Note that due to the complexity of the geometry of both the airfoil and the dovetail, these parts were split into two components and meshed separately to provide well-behaved hexahedral meshes. Additionally, the airfoil shown in Figure 6 does include the top of the platform. The part was partitioned in this manner to move the contact region defined between the two parts below the higher stress region where the airfoil transitions into the platform. Erroneous element deletion did occur in preliminary analysis of the blade in the fillet region of the airfoil during impact simulations when the blade was partitioned where the airfoil meets the platform. The contact card defined between the airfoil and the platform is *CONTACT_TIED_SURFACE_TO_SURFACE. This contact formulation was the same across all simulations.

Figure 7. Mesh of dovetail and blade platform.

The disk was meshed to have a similar mesh density as the blade platform near the contact points and is shown in Figure 8.

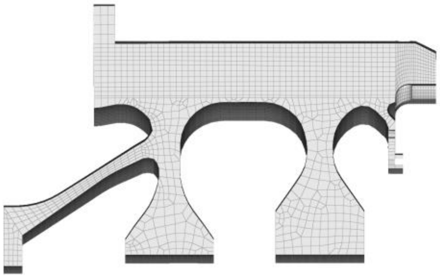

Figure 8. Side view of a sector of the fan disk mesh.

The disk flange was originally modeled as a separate part and its mesh is shown in Figure 9. The flange was then integrated with the disk part, and modeled as a single part in all the simulations.

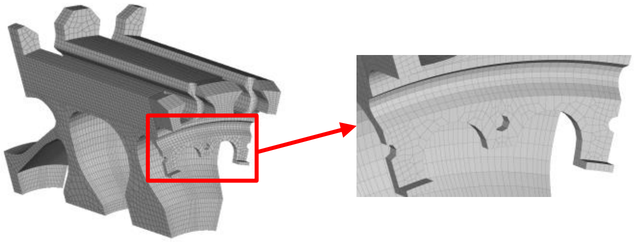

Figure 9. Disk flange mesh.

The retainer and single sector of the retention ring mesh is shown in Additional properties of the meshes of key components of the fan assembly are described in Annex A[11].

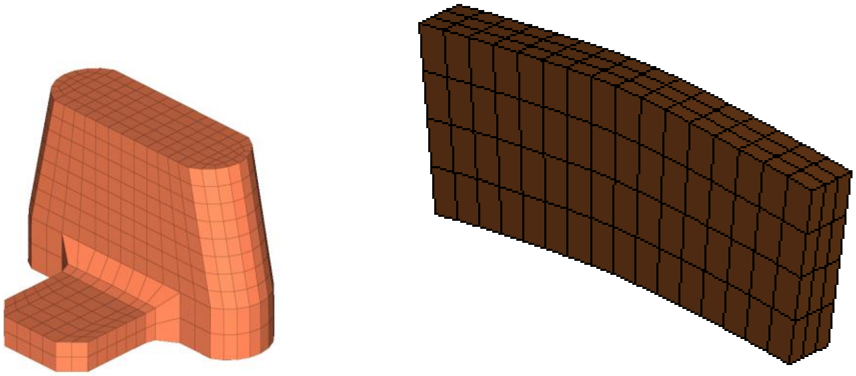

Figure 10. These parts had relatively simple geometries and the mesh density was selected to have a few elements through the thickness while maintaining good aspect ratios. Additional properties of the meshes of key components of the fan assembly are described in Annex A[11].

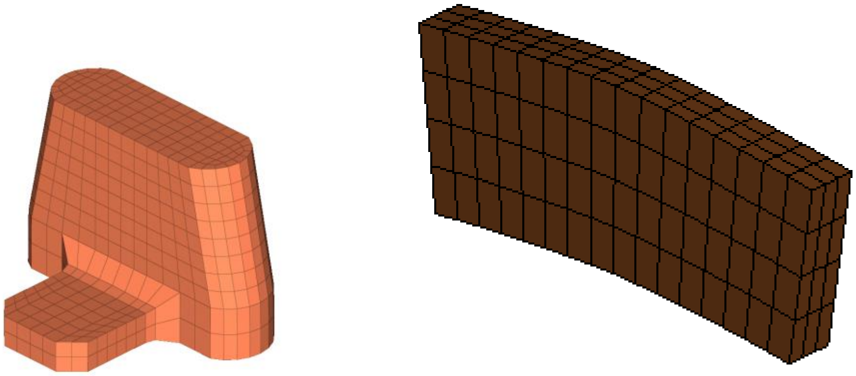

Figure 10. Single retainer mesh and portion of retention ring mesh.

5.3.2 Casing

The casing was modeled with the Ti-6Al-4V alloy elastic material model using the *MAT_ELASTIC keyword with the exact same properties as the retainer. The casing was meshed with quadrilateral shell elements. In the preliminary simulations, the default Belytschko-Tsay shell element formulation (ELFORM=2) was used but due to unstable energies in the casing due to the UAS impact, the element formulation was changed to a fully integrated shell element (ELFORM=16). The hourglass control type selected was IHQ=4 with coefficient QM=0.1 for the finalized UAS ingestion simulations. The casing model was not developed to evaluate containment during the ingestion. It was included to provide an appropriate boundary condition during the ingestion and to extract out energies imparted to the casing during the ingestion events. This simple geometry and material model can adequately address these needs at a low computational cost.

5.3.3 Nose Cone

The bi-conic nose cone was composed of the aluminum 2024 alloy and was modelled as elastic using the *MAT_ELASTIC keyword. Material information for aluminum 2024 was obtained from prior FAA projects[18] with the material models being made available by AWG[19]. The nose cone was meshed using solid hexahedron elements, and the element formulation used was the constant stress solid element (ELFORM=1). In the same manner as the fan assembly parts with the constant stress elements, the nose cone had hourglass control defined with the type IHQ = 6 and the coefficient QM = 0.1.

5.3.4 Shaft

The shaft was modeled as a rigid body using the *PART_INERTIA keyword with mass and inertia properties included. The shaft used the default Belytschko-Tsay shell element formulation (ELFORM=2), and hourglass controls IHQ=2 and QM=0.1. The keyword *MAT_RIGID was used to define the material for the shaft and the material properties were that of stainless steel[20]. The rotation of the shaft at various speeds for different cases in this report required the *BOUNDARY_PRESCRIBED_MOTION_RIGID keyword to be defined along with a vector in the direction of the rotational axis.

Due to the model being restricted to the fan assembly and no available information on the other downstream components that connect to the shaft (i.e., bearings, compressor stages and turbine stages), the shaft was modeled as a rigid body moving with the prescribed speed. Since the shaft is rigid, no contact was applied at the disk interface and instead the disk is simply driven with the same prescribed motion where it would interface with the shaft. Not including the shaft-disk contact simplifies the computational model without affecting the results. Note that the shaft is included only as a visual reference in the simulations.

5.4 DYNAMIC SIMULATIONS

Dynamic simulations were conducted on the fan model to ensure that it meets the key structural and vibratory requirements of a fan to meet certification requirements and provide reference information for further analysis.

5.4.1 Modal Analysis

A key structural requirement of the fan model was that the first bending mode of the fan does not experience a resonance condition under an Engine Order (EO) one excitation. A resonance condition would cause the fan blades to experience large vibrational amplitudes, leading to fatigue problems. Only the first bending mode was examined due to the higher likelihood of being excited by the incoming air. Similarly, only EO one excitation was considered during the modal analysis post-processing.

The modal analysis included only the blade and excluded any portion of the disk. The blade dovetail region was fully constrained, allowing only the airfoil to move. Blade-alone modeling of the system and the accompanying constraints were chosen based on recommendations by participating engine manufacturers to better match their internal analysis best-practices. The rotational speed of the fan influences the final vibratory response of the system due to rotational speed effects such as stress-stiffening and spin-softening. For the purposes of running a pre-stressed modal analysis, the fan model was imported into ANSYS Mechanical APDL and a static structural analysis was run with a specified rotational speed.

The blade-alone, pre-stressed modal analyses were calculated at multiple rotational speeds between 0 and 6,000 Revolutions Per Minute (RPM) to capture the full non-linear effects. The resulting Campbell diagram is depicted in Figure 11 where the first bending mode natural frequency (black line) is shown to be increasing quadratically with rotational speed. Also depicted in Figure 11 are the first 10 EO excitation lines, shown in blue. Three specific rotational speeds were of concern: 1) take off speed of 5175 RPM; 2) cruise speed of 4658 RPM; and 3) descent speed of 1139 RPM. There is no expected resonance of the blade at any of the three operating rotational speeds of the fan, or at any rotational speed within the operational speed range of the fan.

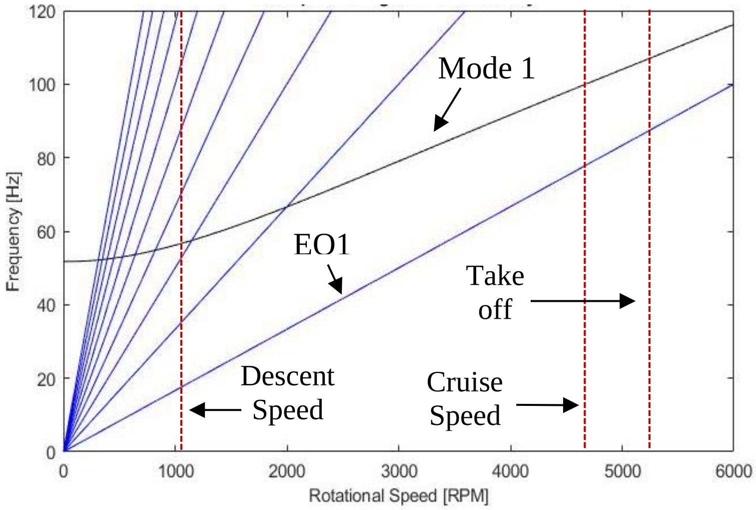

Figure 11. Blade-alone Campbell diagram.

5.4.2 Pre-stress Analysis

During operation of the engine, the fan can be rotating at a number of speeds. The higher the rotation speed the larger the stresses in the blade and disk due to centrifugal loads. The fan design must be able to withstand these forces without any permanent plastic deformation. The stress in the fan and corresponding blade deflections can be computed using an explicit and/or implicit process. In this work, the implicit method used to conduct the pre-stress analysis will be discussed. This analysis will be used not only to compute the stresses in the blades to ensure the validity of the design, but also as a starting point for future dynamic simulations that will be discussed in this report (i.e., blade-out, bird ingestion, and UAV ingestion).

The intended result of the pre-stress analysis was twofold: (1) to ensure the fan design can withstand the centrifugal loads; and (2) to have a rotating fan model where further dynamic simulations could be performed. Before using the results an explicit step, where the fan underwent two rotations, was conducted in LS-DYNA. The purpose of these two rotations was to monitor the element stresses present at both the root of the fan blade and at the mid-span location. These stresses should be relatively constant with some computational noise expected. Figure 12 shows the stress as a function of time at the blade mid-span, for the two-sector model, for the highest rotation case where the fan is rotating at 5175 RPM (ω =541.9247 rad/s). Note that the implicit and explicit analysis were conducted for each rotational speed analyzed in this report and similar results were found for each case.

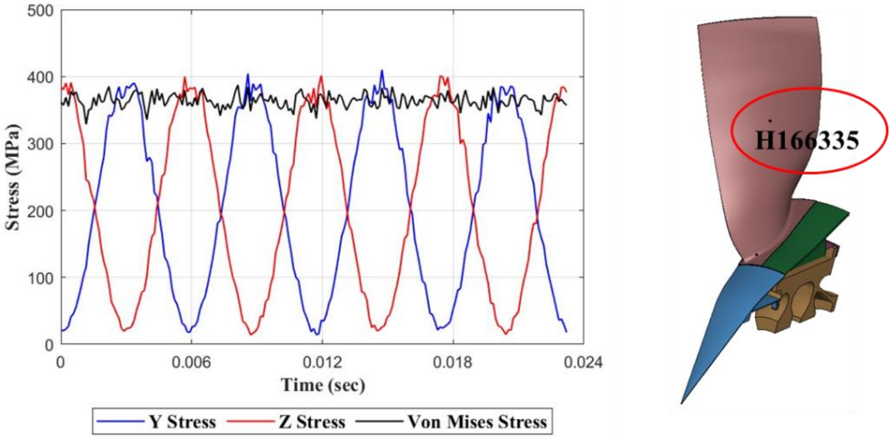

Figure 12. Element stress at blade mid-span for two-sector model.

The blade was rotating about the x-axis so there was a sinusoidal variation in the Y-Stress (σ_{yy}) and Z-Stress (σ_{zz}) measured using global coordinates. The von Mises stress had relatively small variation due to rotation, as expected.

The corresponding von Mises stress contour of the whole fan sector is shown in Figure 13. The highest stress location in the blade is indicated and it is well below the yield strength of the titanium alloy Ti-6Al-4V used for the fan, which is 1150 MPa[13].

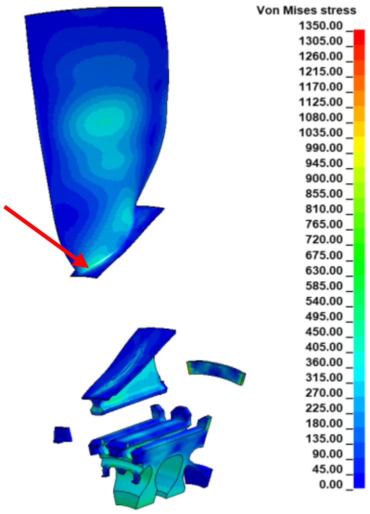
Maximum von Mises stress in the blade (437 MPa)

Figure 13. Stress in single sector after pre-stress analysis at highest rotational speed of 5175 rpm.

5.4.3 Bird Ingestion Simulations

From 1990-2019, 191,571 bird strike events involving civil aircraft were reported to the FAA with 11% of those instances involving striking of the aircraft engines[21]. Despite only 11% of those bird strikes involving the aircraft engines, 26% of the bird strikes involving damage to the aircraft component occurred when the engines were struck[21]. Bird ingestion events occur with enough regularity despite the FAA mitigation efforts that bird ingestion tests are required to be performed as part of the airworthiness certification process for aircraft engines. The details and requirements of these tests are found in the Title 14 Code of Federal Regulations 33.76[22]. In summary, there is a large bird ingestion test and medium flocking bird ingestion test with the weight and number of birds dependent on the inlet area of the engine. There are specified thrust profiles that the engine must follow for each test and hazardous engine effects that are not permitted.

These bird ingestion tests involve full engines and are very expensive for OEMs to complete; thus there is a strong motivation to be successful on the first attempt. Therefore, bird ingestion simulations are performed throughout the design phase to avoid failures during the certification tests. The fan blades are usually the most critical components, and their most critical location is targeted to be the impact area for the bird. The fan model developed for this research was designed to have structural characteristics comparable to high bypass ratio fans used commonly in commercial transport and would be expected to be able to pass these certification tests. To provide evidence of this, simulations of bird ingestion events were performed and analyzed to confirm the fan model would meet important test criteria and be in line with industrial experience. Certain requirements such as the exact thrust profiles and an uncontrolled fire were beyond the scope of this work, but the damage caused by the impact of the bird and resulting plastic deformation could be modeled. Extreme damage to the blades would suggest the possibility of uncontained high-energy debris and excessive plastic deformation could block the flow path, thus reducing the thrust below allowable levels.

The bird ingestion simulations performed were setup to model the large single bird ingestion test. Based on the inlet area of the fan rig model, the appropriate bird weight was 2.75 kg (6.05 lbs). The selection of an appropriate bird model is important for obtaining useful simulation results at a reasonable computational cost. The bird model selected for the bird ingestion simulations was taken and modified from the AWG website[23]. The model was validated by comparing LS-DYNA simulations to Hopkinson bar experimental results[24]. The bird was discretized using the smoothed-particle hydrodynamics method rather than the Lagrangian elements used for the fan rig model.

For the bird ingestion simulations, six fan sectors and corresponding sections of the nose cone and shaft were used along with the casing and two dovetails, one at each end of the six fan sectors, to model the fan rig. The decision to model the fan rig with multiple fan sectors for the bird ingestion simulations was based on best practices set forth by the AWG[6]. The two additional dovetails were included to give an appropriate boundary condition at the ends of the six fan sectors and prevent any nonphysical behavior in the simulations. These two dovetails are slightly different than the other dovetail parts because they follow the exact geometry of the dovetail rather than including some of the platform in the blade part. The additional dovetails were prescribed to rotate about the rotational axis of the fan at 5175 RPM (ω =541.9247 rad/s) and were constrained in the axial direction.

Three different bird ingestion cases were conducted at different radial locations along the blade (i.e., blade root, blade midspan, blade tip). The kinematics of the bird ingestion at the blade tip are shown in Figure 14 and the resulting plastic deformation in the fan is shown in Figure 15.

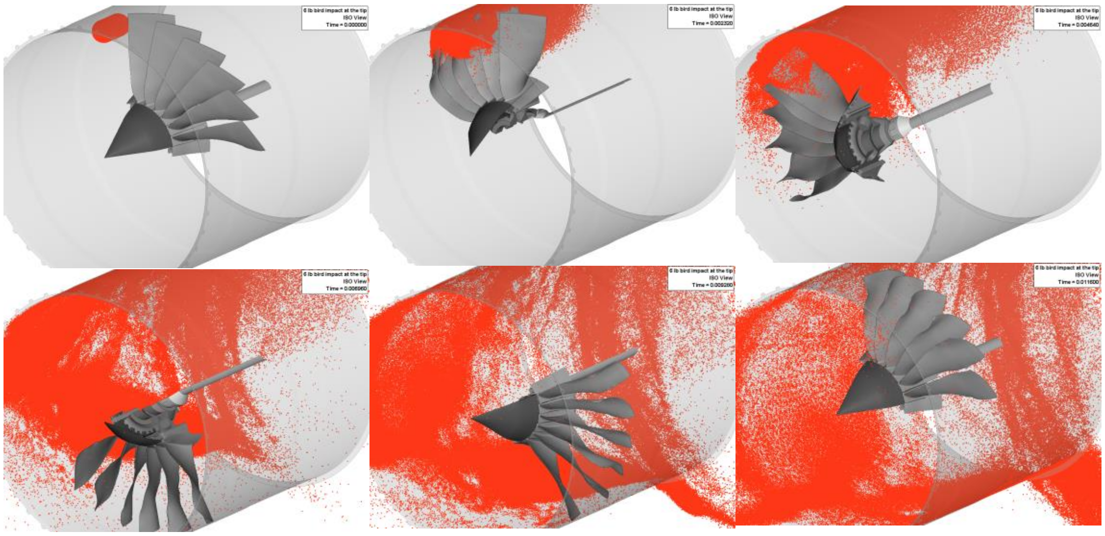

Figure 14.Kinematics of bird ingestion near blade tip.

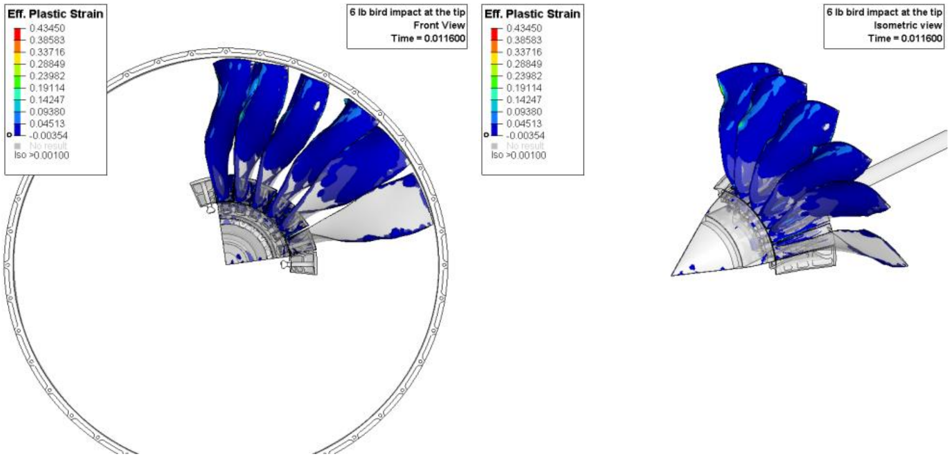

Figure 15. Resulting plastic deformation in fan from large bird ingestion near blade tip.

The bird ingestion simulations show that there is some plastic deformation in the blades from the ingestion, with no signs of cracking or significant material loss in any of the cases. Also, there are no high root strains in the blades. This is consistent with industry experience with certified designs.

6. QUADCOPTER MODEL VALIDATION FOR ENGINE INGESTION CONDITIONS

The UAS quadcopter model that was selected for use in the ingestion simulations was developed by NIAR using a physics-based Building Block Approach that was initially developed in the A3 Airborne Collision Studies[2], and validated experimentally for a wide range of conditions. This section discusses the experimental validation of the key components and full UAS at conditions equivalent to an actual engine ingestion. The experiments were conducted at UAH by launching UAS components and full UAS at titanium alloy (Ti-6Al-4V) wedge shaped test articles at high velocity (202-371 m/s) to capture the relative velocity of the slicing impact of a UAS on a fan blade during ingestion.

6.1 UAS COMPONENT LEVEL EXPERIMENTS

Similar to the A3 Airborne Collision Studies[2], three critical UAS components were subjected to impact tests for the current research component level validation. These components consisted of the motor, the camera, and the battery. After discussing the worst UAS engine impact scenarios with industry partners and NIAR, OSU developed the component level test matrix shown in Table 1. Each UAS component had two different test configurations, one each to simulate an 80% and 50% radial span impact of the fan blade. Each test configuration had three repetitions to help quantify variability between tests due to differences in projectile, target, and desired impact conditions for each test. Unfortunately, the machining process damaged one of the blades for the 50% span motor tests, which reduced the total number of tests from 18 to 17.

Table 1. Component level test matrix.

Test Case	Test Number	Projectile	Target	Span (%)	Relative Angle (°)	Impact Location	Designed Speed	Performed Speed
M80L7-001	20-188	Motor	It Blade OPT A-2 Rev 2	80	25	LE	710.98 kts (365.76 m/s)	716 kts (368.34 m/s)
M80L7-002	20-189	Motor	Ti Blade OPT A-2 Rev 2	80	25	LE	710.98 kts (365.76 m/s)	713 kts (366.8 m/s)
M80L7-003	20-190	Motor	Ti Blade OPT A-2 Rev 2	80	25	LE	710.98 kts (365.76 m/s)	715 kts (367.83 m/s)
M50L5-004	20-183	Motor	Ti Blade OPT B-5 Rev 2	50	30	LE	562.86 kts (289.56 m/s)	569 kts (292.72 m/s)
M50L5-005	20-184	Motor	Ti Blade OPT B-5 Rev 2	50	30	LE	562.86 kts (289.56 m/s)	569 kts (292.72 m/s)
B80A5-007	20-200	Battery	Ti Blade OPT A-2 Rev 2	80	25	5'' aft LE	562.86 kts (289.56 m/s)	547 kts (281.4 m/s)
B80A5-008	20-201	Battery	Ti Blade OPT A-2 Rev 2	80	25	5'' aft LE	562.86 kts (289.56 m/s)	550 kts (282.94 m/s)
B80A5-009	20-202	Battery	Ti Blade OPT A-2 Rev 2	80	25	5'' aft LE	562.86 kts (289.56 m/s)	549 kts (282.43 m/s)
B50L7-010	20-210	Battery	Ti Blade OPT B-5 Rev 2	50	30	LE	710.98 kts (365.76 m/s)	533 kts (274.2 m/s)
B50L7-011	20-211	Battery	Ti Blade OPT B-5 Rev 2	50	30	LE	710.98 kts (365.76 m/s)	539 kts (277.29 m/s)
B50L7-012	20-214	Battery	Ti Blade OPT B-5 Rev 2	50	30	LE	710.98 kts (365.76 m/s)	532 kts (273.68 m/s)
C80L7-013	20-191	Camera	Ti Blade OPT A-2 Rev 2	80	25	LE	710.98 kts (365.76 m/s)	722 kts (371.43 m/s)

C80L7-014	20-192	Camera	Ti Blade OPT A-2 Rev 2	80	25	LE	710.98 kts (365.76 m/s)	711 kts (365.77 m/s)
C80L7-015	20-196	Camera	Ti Blade OPT A-2 Rev 2	80	25	LE	710.98 kts (365.76 m/s)	719 kts (369.89 m/s)
C50L5-016	20-185	Camera	Ti Blade OPT B-5 Rev 2	50	30	LE	562.86 kts (289.56 m/s)	571 kts (293.75 m/s)
C50L5-017	20-186	Camera	Ti Blade OPT B-5 Rev 2	50	30	LE	562.86 kts (289.56 m/s)	569 kts (292.72 m/s)
C50L5-018	20-187	Camera	Ti Blade OPT B-5 Rev 2	50	30	LE	562.86 kts (289.56 m/s)	568 kts (292.72 m/s)

The name of each test case in Table 1 was proposed to provide a brief label that accurately describes each combination of UAS component, span and relative angle of the blade, location of the impact, and the impact speed. Every impact condition is coded using eight characters (AijBk-mnl):

- A – Distinguishes between UAS components:
  - Motor (M)
  - Battery (B)
  - Camera (C)
- ij – Distinguishes between span and relative angle of Titanium blade:
  - 80% and 25 deg (80)
  - 50% and 30 deg (50)
- B – Distinguishes between impact location:
  - Leading Edge (L)
  - 5 inches aft of leading edge (A)
- k – Distinguishes between impact speed:
  - 710.98 kts (7)
  - 562.86 kts (5)
- mnl – Distinguishes between the number of the test:
  - 001 (Test 1)
  - 002 (Test 2)
  - …
  - 018 (Test 18)

Example of M80L7-001:

- Motor
- 80% and 25 deg
- Leading edge
- 710.98 kts
- Test 1

Details on the component level titanium test article are given in Table 2 for the 80% and 50% radial span impact cases and models of the test articles are shown in Figure 16.

Table 2. Component level targets details.

Target Description	Material	Target size [mm]	Instrumentation	Quantity Needed
Titanium Blade Opt A-2 (for 80% radial impact)	Ti-6Al-4V	254 x 457.2 (including 76.2 mm extension for bolts connection)	Linear Strain Gauge and DIC	9
Titanium Blade Opt B-5 (for 50% radial impact)	Ti-6Al-4V	254 x 457.2 (including 76.2 mm extension for bolts connection)	Linear Strain Gauge and DIC	8

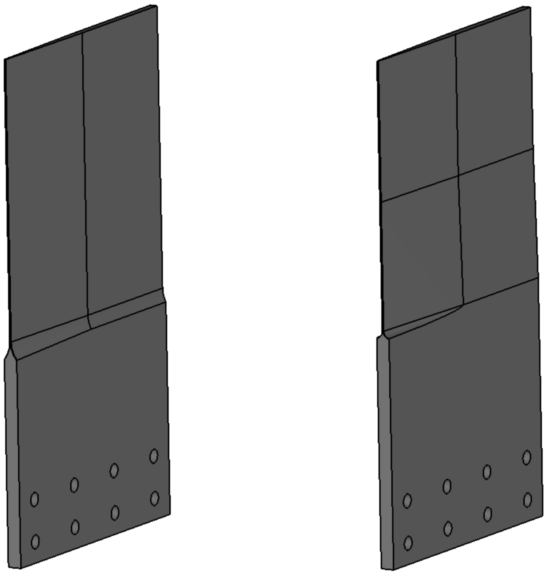

Figure 16. Titanium blade opt A-2 (left) and titanium blade opt B-5 (right).

An existing single stage compressed gas gun was modified for accelerating the motor, camera, and battery components of the UAS to the desired equivalent impact velocity. This gun utilized a 11.6 m (38 ft) long, 90 mm (3.54 in) inside diameter barrel adapted to an impact test section configured with orthogonal and Digital Image Correlation System camera ports, a scrubber system for hazardous gas removal, cable feed throughs for load cell, strain gauge, and lighting power cables (Figure 17). The full system consists of a bulk gas manifold, which provides compressed gas storage and supplies gas to the pressure reservoir. While the magnitude of the pressure in the reservoir represents the maximum capability of the gun to accelerate a projectile, the timing or rate of opening the valve provides control over the rate of acceleration of the projectile. Based on the requirement to fire the UAS battery which is significantly larger and heavier than the UAS motor and camera, an alternate gas pressure reservoir and larger ball valve were installed in the system at the end of the component test period to accelerate the larger, heavier, and more compliant batteries and mitigate battery deformation. The barrel was mounted and aligned on a heavy I-beam structure using adjustable stanchions. Stanchions mounted on the I-beam to support the barrel enabled barrel alignment and have roller interfaces with the barrel that allow for barrel movement up and down range to adjust the projectile and sabot fly-out distance. Fly-out distance, in conjunction with projectile velocity and sabot design, was critical to provide enough flight time for air loads to separate the sabot from the projectile in flight.

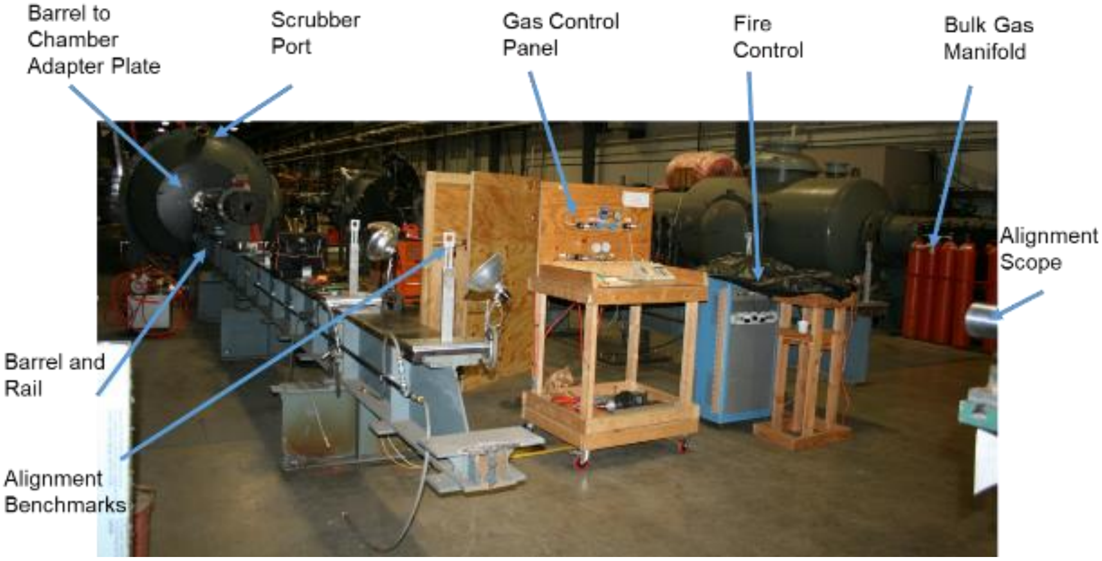

Figure 17. UAS component impact test range setup (reservoir not shown).

The titanium test articles are mounted to a support frame using a steel tabletop and stainless-steel brackets (Figure 18). Load cells (set of four ICP® quartz force ring, PCB Piezotronics 204C, with a 40,000 lbf compressive capacity and an upper frequency limit of 55,000 Hz) are beneath the tabletop mounted on the four studs that protrude up through the tabletop surface in Figure 18. The load cells are in compression prior to the test, so that tensile loads can be calculated based on the decrease in the static compressive force.

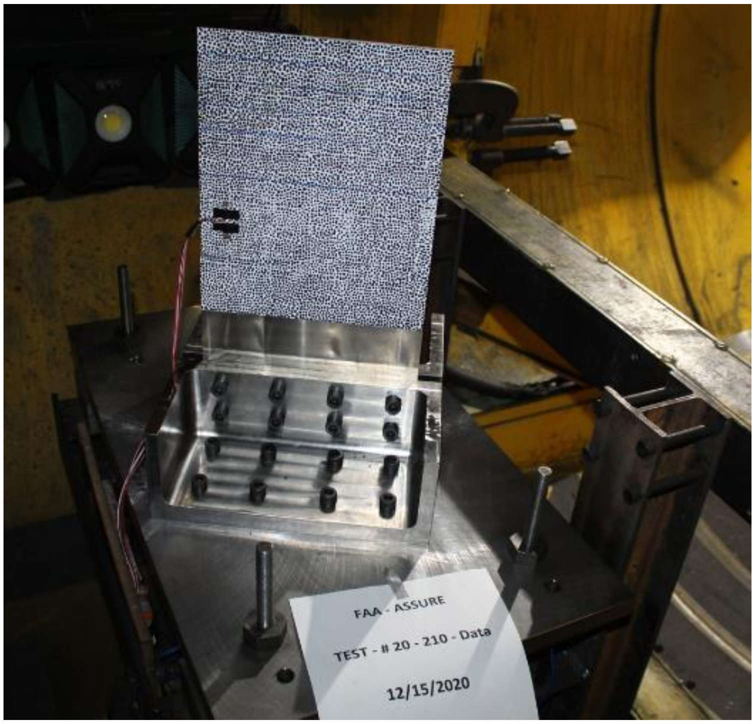

Figure 18. Titanium test article, stainless steel bracket, and tabletop mount.

High-Speed Video Cameras were used to record the projectiles in flight and the resulting impact on the target. Photron FASTCAM SA-Z high speed cameras were used. These cameras can provide a one-megapixel (1024x1024) image resolution at 20,000 frames per second or frame rates beyond 2 million fps at reduced image resolution. The Task A17 impact testing used two sets of Digital Image Correlation System cameras to measure surface strain fields on the up range and downrange sides of the titanium blade targets (Figure 19). A speckle pattern was applied to both sides of the test articles to allow use of Digital Image Correlation for visual strain field measurement (Figure 18). There was also a pair of orthogonal cameras used in the testing, which were Cameras 1 and 6 in Figure 19. The Photron FASTCAM Viewer 4 software was used to perform post-processing of the raw files. Projectile velocity was measured using FASTCAM Viewer 4. The data from Cameras 1 and 6 were used to measure velocity. Markers were placed on the projectile and the movement of the markers over 10 frames was observed in the software during velocity estimation. A scale factor for each projectile was measured prior to any testing and applied to each high-speed video to determine impact velocity.

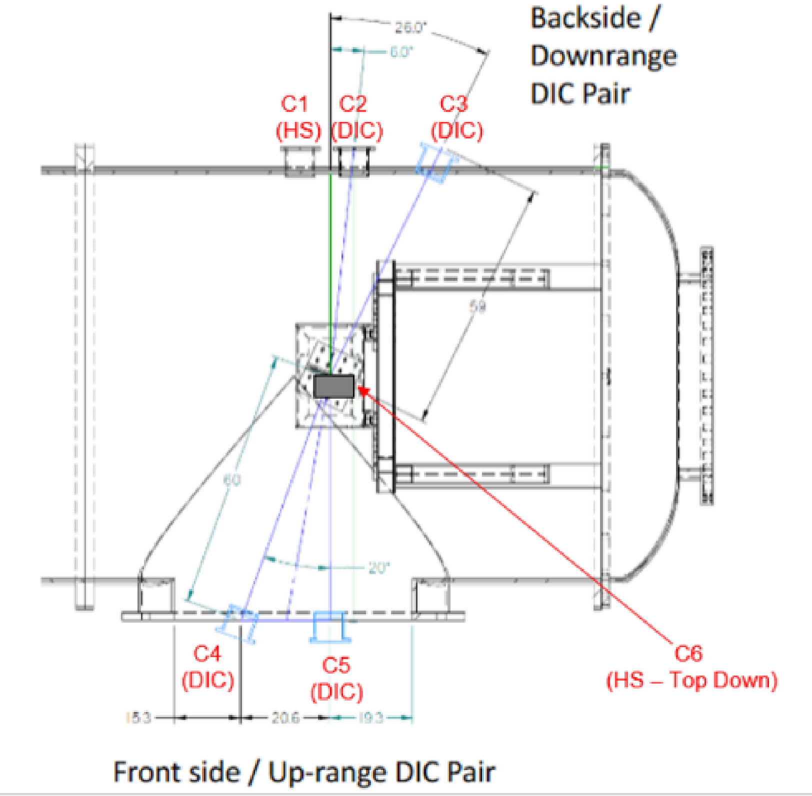

Figure 19. High speed camera locations inside the test chamber (top down view).

All the equipment and sensors were calibrated in the mornings on days when tests were performed. Just before testing began, the gas gun was cleaned and prepared. After verifying that the pre-test procedures were completed and all checks completed, the actual component was placed inside the sabot and fired on the target. The data capture by the equipment and sensors was verified. The titanium blade was removed from the fixture and a 3D scan was performed. The chamber was then cleaned and prepared for the next test. All raw and processed data was transferred to NIAR after testing to begin the validation process of the UAS component models.

6.2 UAS COMPONENT LEVEL VALIDATION

The experimental data from each of the component level experiments were compared with computational simulations and the component computational models were adjusted to improve the match. The details of all the validation results are provided in Annex B to Task A17[16]. Below is an example of the validation effort matching the kinematics, load cell, and DIC experimental data for the M80L7 test configuration.

For this test configuration, the motor impacts the leading edge of the titanium blade Opt A-2 at the desired velocity of 365.26 m/s (710 knots). The impact location is at 80% radial span of the blade, and the blade is angled at 25 degrees relative to the impact direction. Three repetitions – M80L7-001, M80L7-002, and M80L7-003 – were conducted. Out of these three repetitions, M80L7-002 was selected to corroborate with the simulation. Figure 20 shows the schematic setup of the M80L7 test configuration.

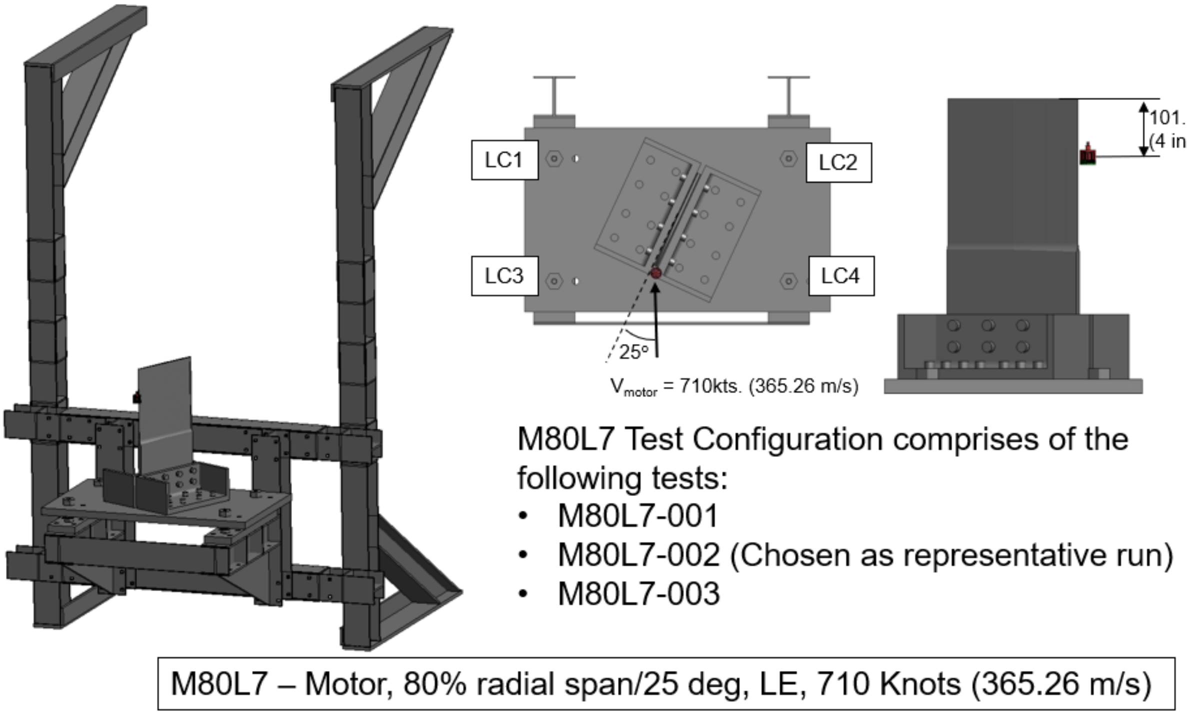

M80L7 Test Configuration comprises of the following tests:

- M80L7-001
- M80L7-002 (Chosen as representative run)
- M80L7-003

M80L7 – Motor, 80% radial span/25 deg, LE, 710 Knots (365.26 m/s)

Figure 20. M80L7 test configuration setup.

To match the conditions of the M80L7-002 test, the FE simulation was set up with the initial projectile velocity of 366.8 m/s (713 knots). The motor's orientation was adjusted to a pitch of -6.1 degrees, a roll of 0 degrees, and yaw of 0 degrees. The impact location to the motor's center of gravity was 106.68 mm (4.2 inches) measured from the top of the blade, which deviated from the desired impact location by 5.08 mm (0.2 inches) shown in Figure 20.

Figure 21 and Figure 22 show the top and side view kinematics comparison between the test and simulation from the start to the end of the impact. Three instances were compared. The first instance at t=0s is the start of the simulation before the impact. The second instance at t=0.001s is during the impact. The last instance at t=0.002s is after the impact.

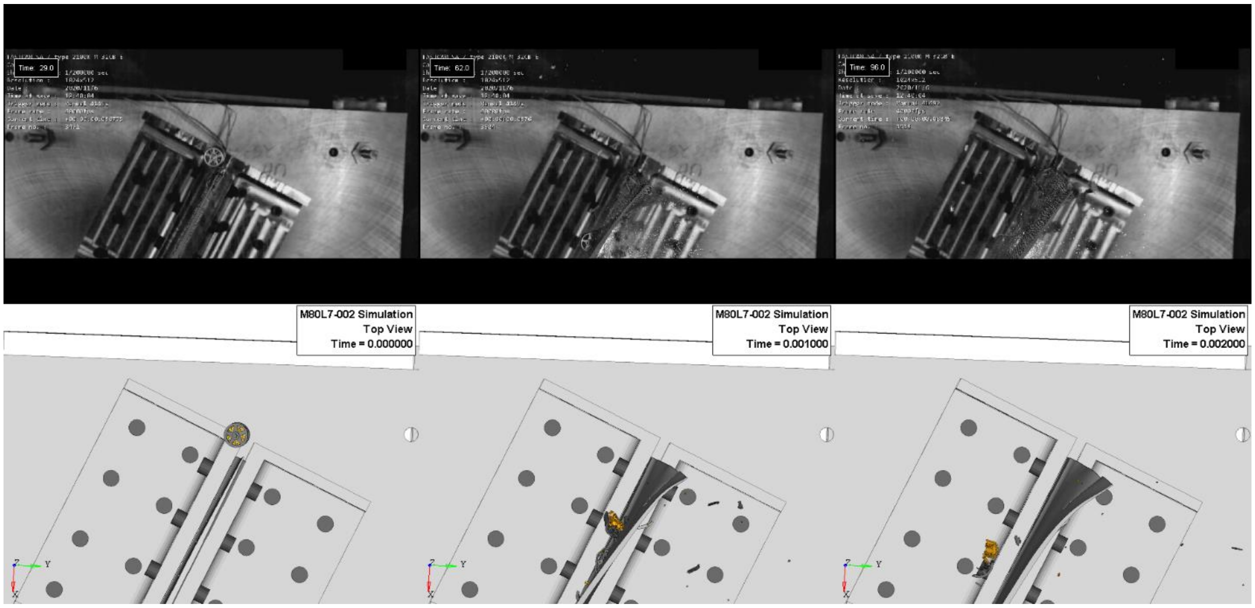

Figure 21. M80L7-002 top view kinematics comparison.

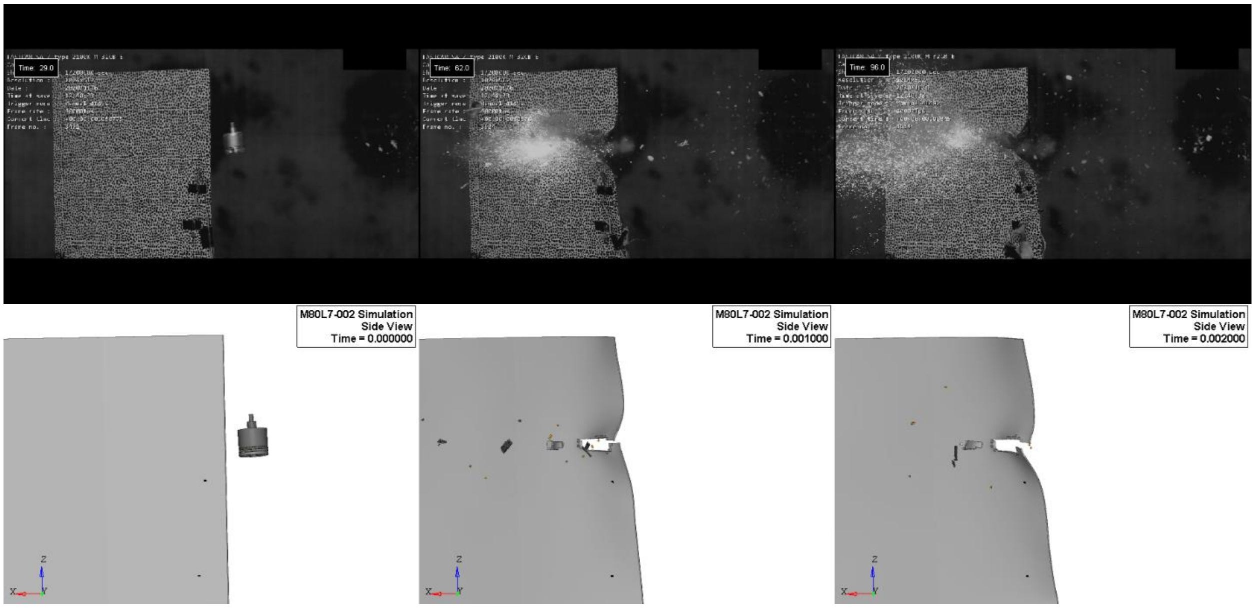

Figure 22. M80L7-002 side view kinematics comparison.

After 2ms of the shown simulation, the blade continued vibrating due to the impact's residual energy. Thus, an additional spring back analysis was performed on the blade to obtain its final deformed shape at its equilibrium state. Figure 23 compares the final blade damage between the spring back analysis prediction and the physical test damage. The FE result for the blade’s LE after spring back analysis shows a good correlation with the final deformed shape of the physical blade's LE.

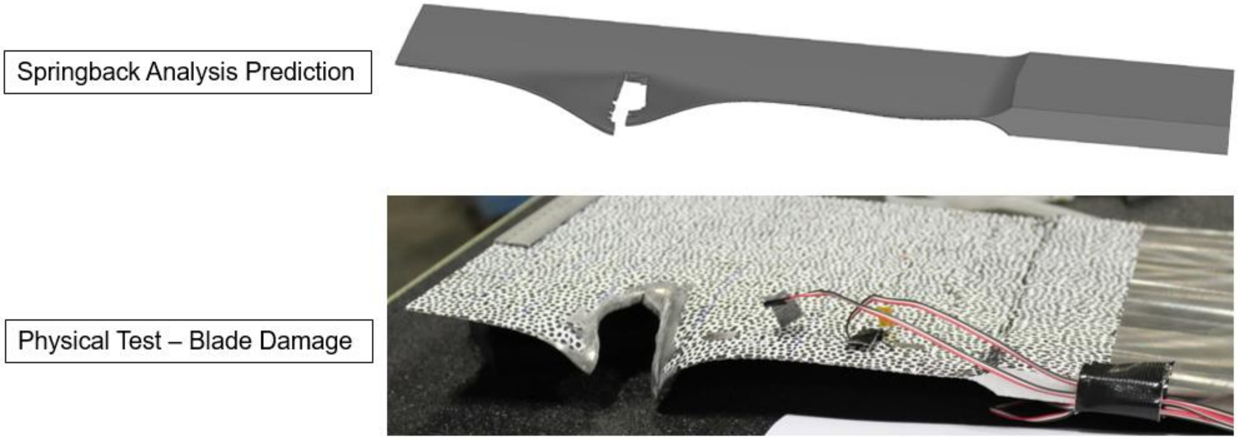

Figure 23. Spring back analysis prediction of blade damage vs. physical test damage.

Due to the slicing nature of the test, parts of UAS debris obstructed the blade surfaces during the impact, making it challenging to process the DIC data. Therefore, only partial blade surfaces were selected where DIC data collection was deemed possible. Figure 24**Error! Reference source not found.** shows the selective areas of the blade for the DIC processing in this test M80L7-002.

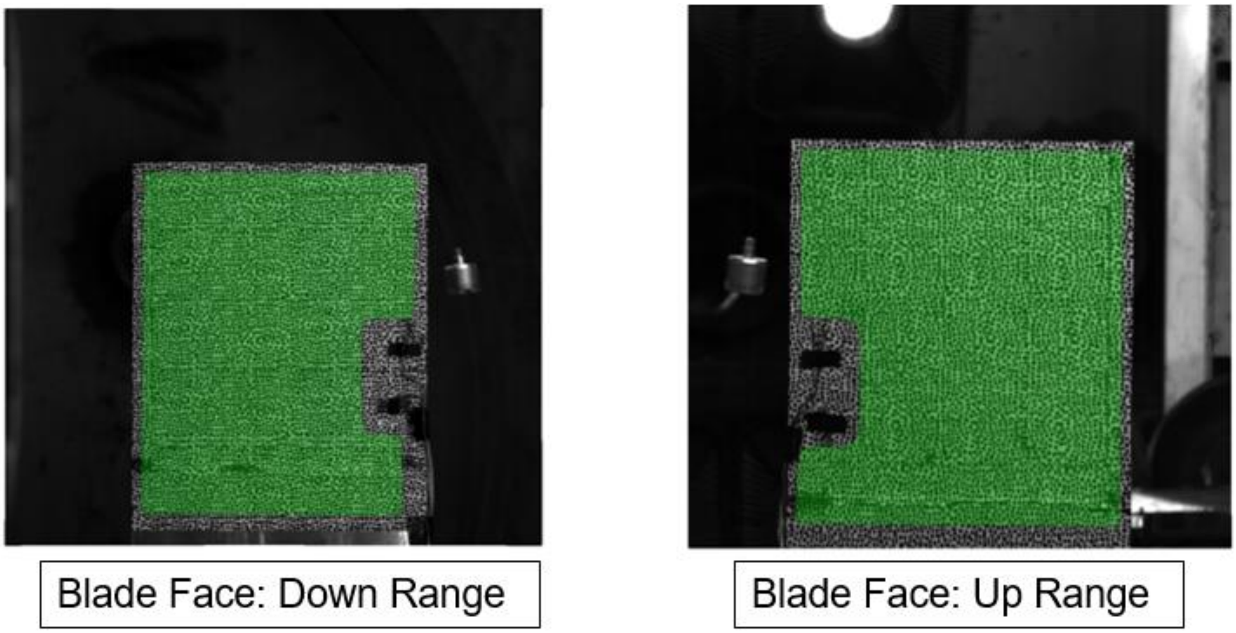

Figure 24. Test M80L7-002 selective areas of the blade for DIC processing.

Figure 25 and Figure 26 show the X (blade chord direction) strains, Z (blade span direction) strains, and Y out-of-plane displacement comparison between the DIC test data and simulation during the impact. Although the UAS debris blockage compromised the quality of the DIC data, the contour comparison around the impact region shows a good correlation.

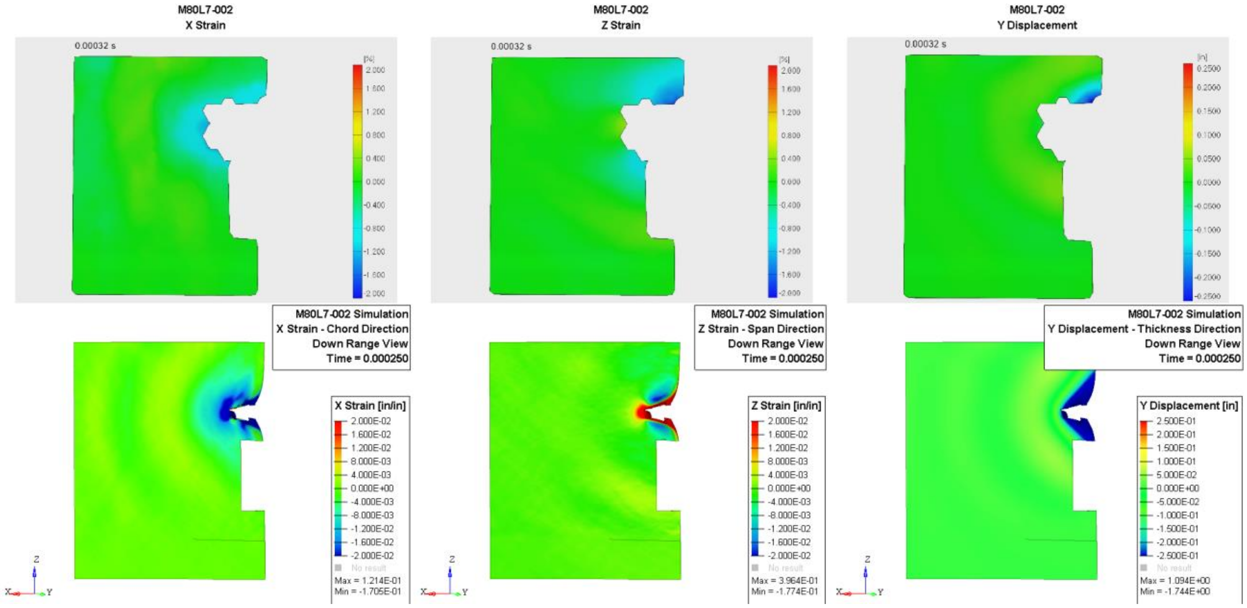

Figure 25. Test M80L7-002 DIC comparison on down range face of the blade – Experimental data (top) and simulation (bottom).

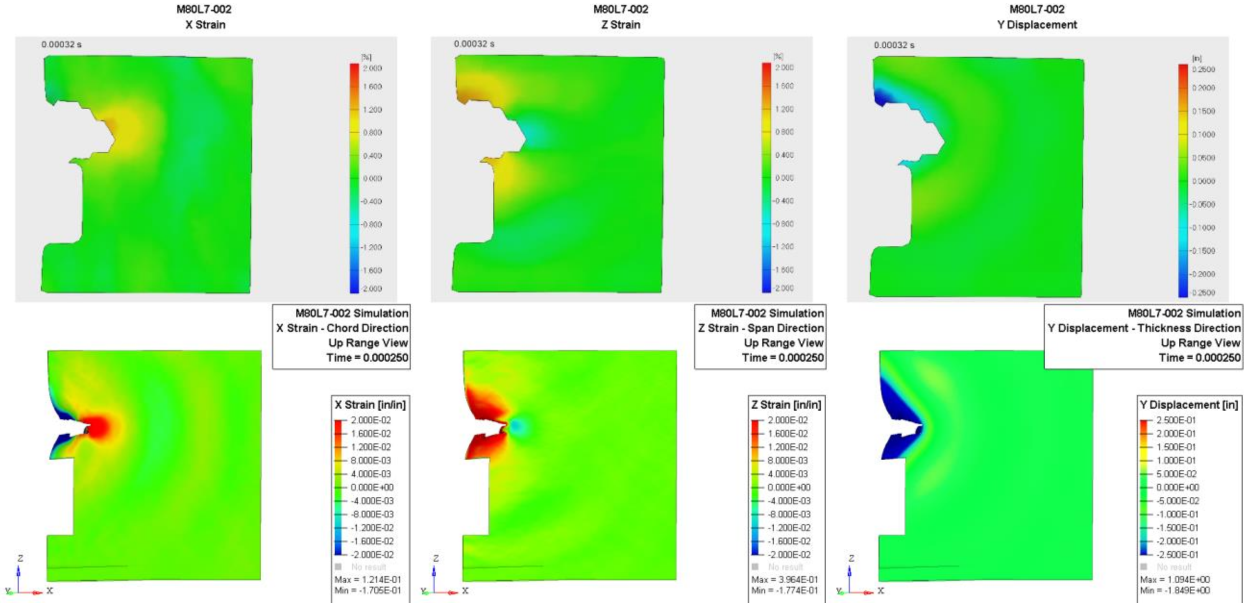

Figure 26. Test M80L7-002 DIC comparison on up range face of the blade– Experimental data (top) and simulation (bottom).

In addition to DIC contour data, the time history, showing the resultant displacement for two points (B and G), was obtained and compared with the simulation for all the tests. Figure 27 and Figure 28 show these points' locations and the displacement comparison results. The simulation displacement results correlate well with the M80L7 tests.

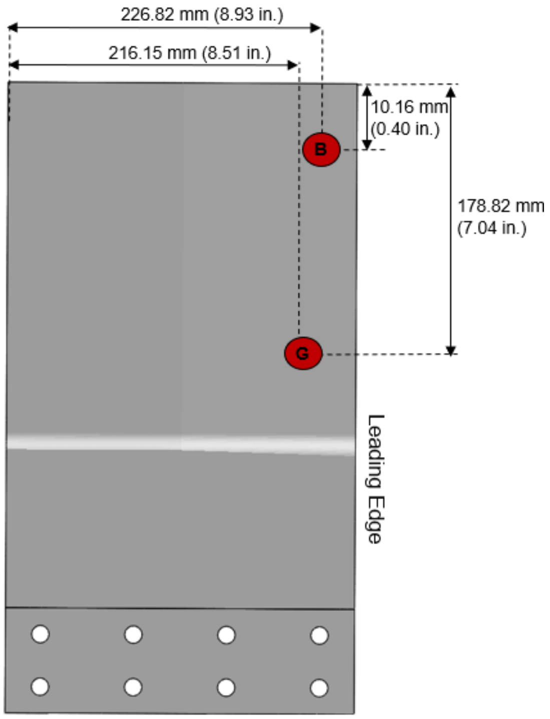

Figure 27. Location of points B and G for extraction of DIC out of plane displacement time history.

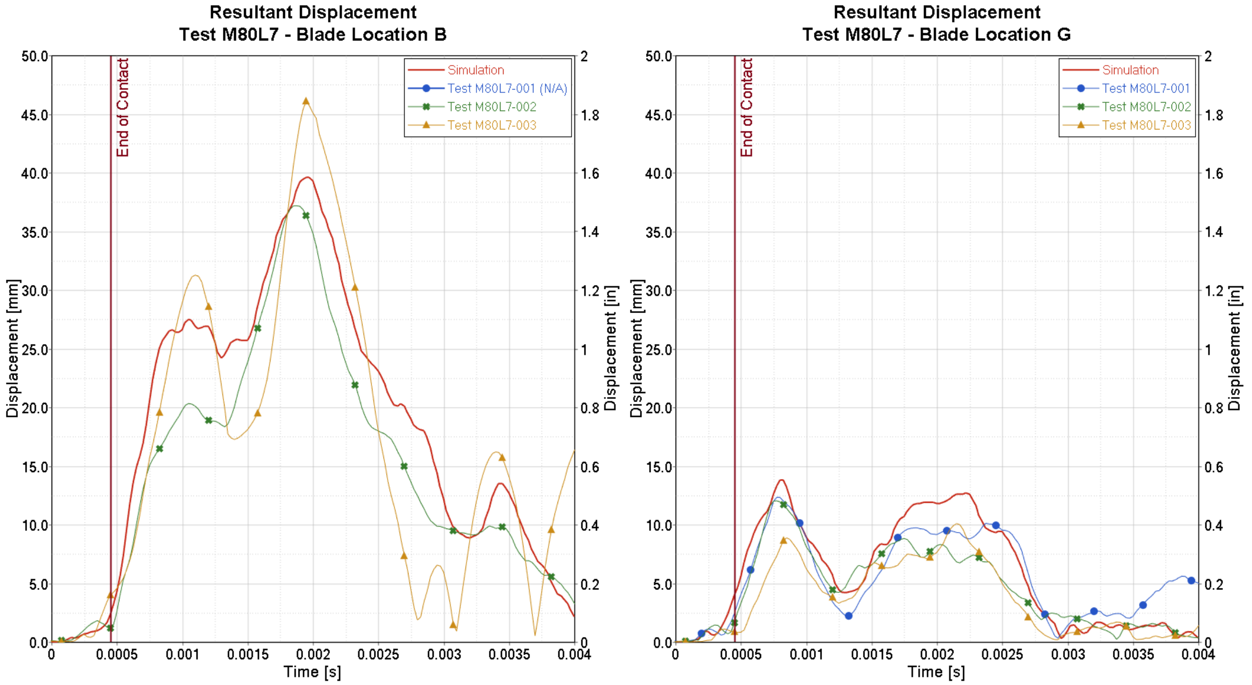

Figure 28. Resultant displacement time history comparison between simulation and M80L7 tests.

Figure 29 shows the load cells' data comparison between the simulation and the three test repetitions. The data has no filter, and its sampling rate was 1MHz for both the simulation and tests. The simulation results agree with the test data. The strain gages' data comparison was not possible due to corrupted test data.

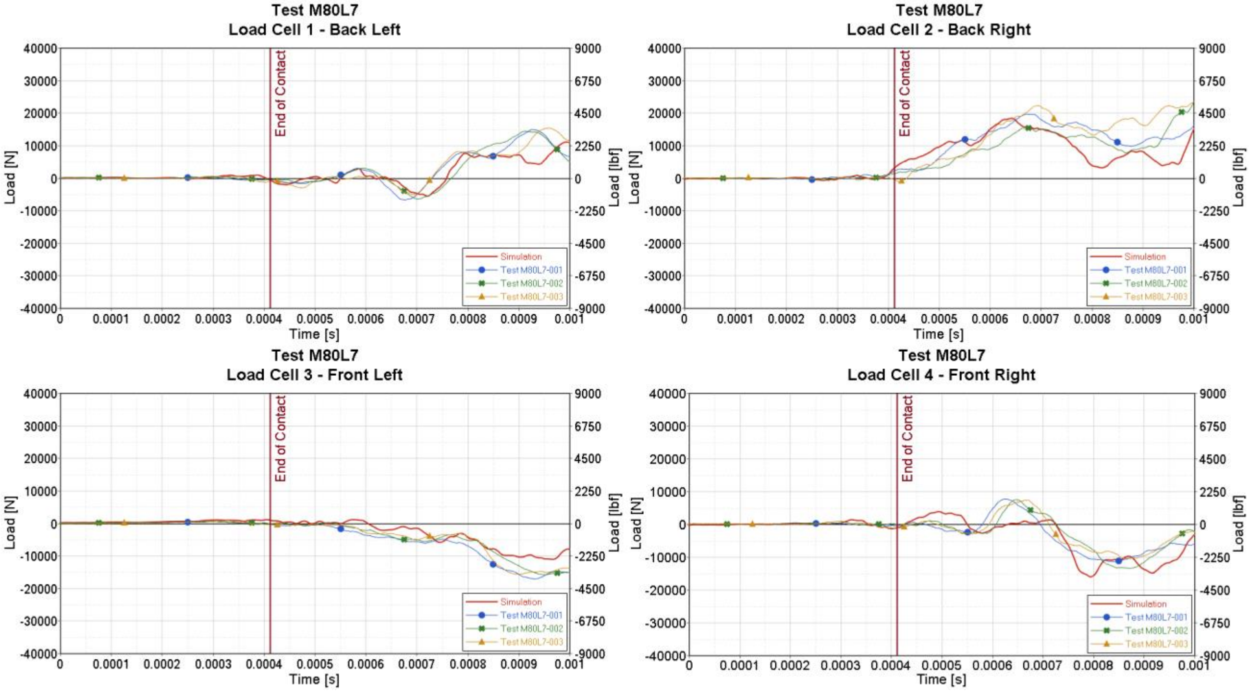

Figure 29. Test M80L7 configuration load cells data comparison.

The results for this test case show a good qualitative correlation between simulation and physical test data in terms of blade damage, loads, and DIC. Thus, for this M80L7 configuration, the motor component of the UAS is considered validated. Similar results and validation were carried out for every other component test configuration and are detailed in Annex B to Task A17[16].

There were updates to each of the UAS component computational models from these experiments. The main update for the motor was on the refinement of material failure definitions for the magnets and stator components. They were re-calibrated for better correlation with the current study test conditions. The main update for the camera was the addition of the lens and its body to improve the fidelity of the camera model for the blade slicing impacts under the current study. The main updates for the battery were the addition of the internal electronics and divisions of battery cells to capture the buckling behavior better. Once updated, the three most important A3 component level tests were rerun for each component to guarantee that these small changes did not significantly affect the previous validation effort, thus proving the robustness of the models.

6.3 FULL UAS EXPERIMENTS

UAH conducted a total of six full UAS impact tests. Table 3 shows the full-scale test matrix. Similar to the component level test matrix, there are two test configurations at 80% and 50% radial span impact locations on the blades, respectively. Each configuration has three test repetitions for a total of 6 tests. The nomenclature of the test case follows the same principles as the component tests described in the previous section. The only difference in this section is the first letter of the test case name, which is the letter D (short for DJI) for all the tests. The draft test matrices had used 711 kts as the target impact velocity for full aircraft impact tests[11]; however, the full aircraft launcher system was unable to achieve this launch velocity. The maximum achievable velocity for a DJI Phantom 3 aircraft in the Aerophysics Research Facility (ARF) at UAH for the full aircraft launch system, at the time of testing, was 425 kts.

Table 3. Full scale test matrix.

Test Case	Test Number	Projectile	Target	Span (%)	Relative Angle (°)	Impact Location	Designed Speed	Performed Speed
D80L7-001	21-82	DJI Body	Ti Blade OPT A-2 Rev 4	80	25	LE	425 kts (218.64 m/s)	406 kts (208.86 m/s)
D80L7-002	21-83	DJI Body	Ti Blade OPT A-2 Rev 4	80	25	LE	425 kts (218.64 m/s)	394 kts (202.69 m/s)
D80L7-003	21-84	DJI Body	Ti Blade OPT A-2 Rev 4	80	25	LE	425 kts (218.64 m/s)	434 kts (223.27 m/s)
D50L5-004	21-52	DJI Body	Ti Blade OPT B-5 Rev 3	50	30	LE	425 kts (218.64 m/s)	433 kts (222.75 m/s)
D50L5-005	21-56	DJI Body	Ti Blade OPT B-5 Rev 3	50	30	LE	425 kts (218.64 m/s)	419 kts (215.55 m/s)
D50L5-006	21-85	DJI Body	Ti Blade OPT B-5 Rev 3	50	30	LE	425 kts (218.64 m/s)	428 kts (220.18 m/s)

Figure 30 and

Table 4 show the projectile (DJI Phantom 3 body) geometry and its detailed specifications. The DJI body excludes the propellers, legs, gimbal, and camera assembly normally present in a full DJI Phantom 3.

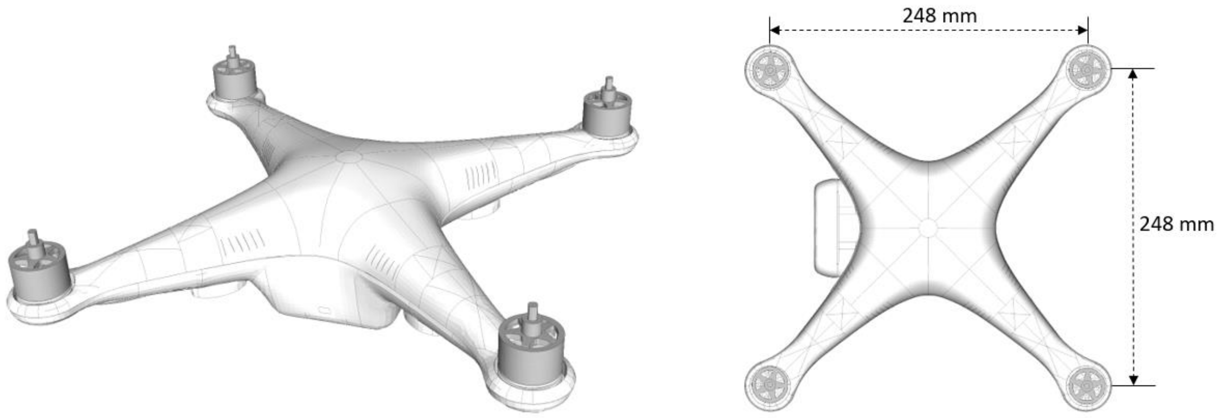

Figure 30. Geometry features of the DJI Phantom 3 body.

Table 4. Specifications of the DJI Phantom 3 body.

Mass	930 g	2.05 lb.
Diagonal (center of the motors)	350 mm	13.8 in
Height	98 mm	3.86 in
Max. Motor Speed	1,240 rad/s	11,840 rpm
Motors	4x brushless DC motors; mass: 54 g	
Battery	4x LiPo cells; capacity: 4480 mAh; mass: 363 g	

Table 5 and Figure 31 show the targets' details and geometry, respectively.

Table 5. Target details.

Target Description	**Material**	**Target size [in]**	**Instrumentation**	**Quantity Needed**
Titanium Blade Opt A-2 Rev 4(for 80% radial impact)	Ti-6Al-4V	10x18 (including 3’’ extension for bolts connection)	Linear Strain Gauge and DIC	3
Titanium Blade Opt B-5 Rev 3(for 50% radial impact)	Ti-6Al-4V	10x18 (including 3’’ extension for bolts connection)	Linear Strain Gauge and DIC	3

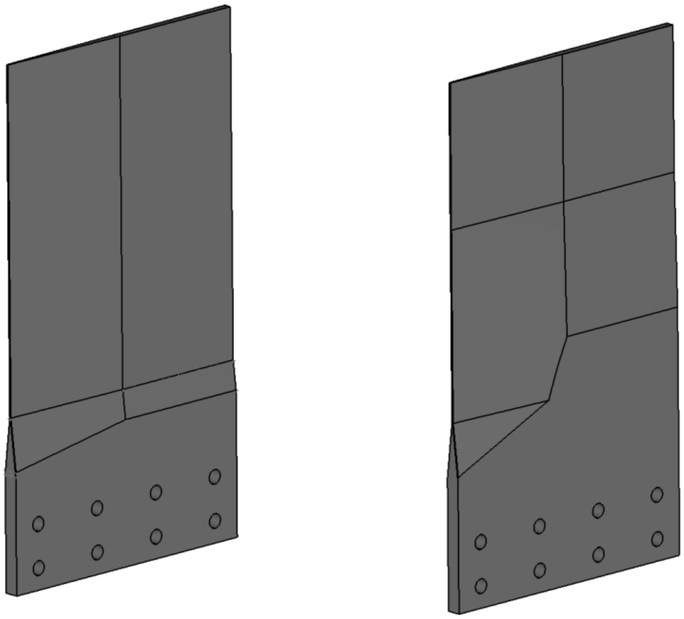

Figure 31. Titanium blade opt A-2 rev 4(left) and titanium blade opt B-5 rev 3(right).

UAH prepared for individual full UAS impact tests by moving the component test fixture and instrumentation from the component impact test range to the full aircraft impact test range. To determine gun conditions (reservoir pressures), ARF personnel conducted developmental shots prior to the actual record tests. Gas gun, instrumentation, data acquisition, and lighting triggering were executed in the same manner during full UAS testing as during component-level impact tests. UAH transferred the full UAS impact test data sets that include strain gauge and load cell signal data, high speed videos, and still images to NIAR for model calibration following each individual test.

6.4 FULL UAS MODEL VALIDATION

Following the Building Block Approach, after the main UAS components were validated, the next step was to validate the complete UAS. The experimental data from each of the full UAS experiments were compared with computational simulations and the full models were adjusted to improve the match. The details of all the validation results are provided in Annex B to Task A17[16]. Below is an example of the validation effort matching the kinematics, load cell, and DIC experimental data for the D80L7 test configuration.

For this test configuration, the UAS body impacts the leading edge of the titanium blade Opt A-2 rev 4 at the desired velocity of 218.64 m/s (425 knots). The impact location is at 80% radial span of the blade, and the blade is angled at 25 degrees relative to the impact direction. Three repetitions – D80L7-001, D80L7-002, and D80L7-003 – were conducted. Due to the high variability of the UAS trajectory from launch for all the tests, they were all selected to corroborate with simulations. Figure 32 shows the schematic setup of the D80L7 test configuration.

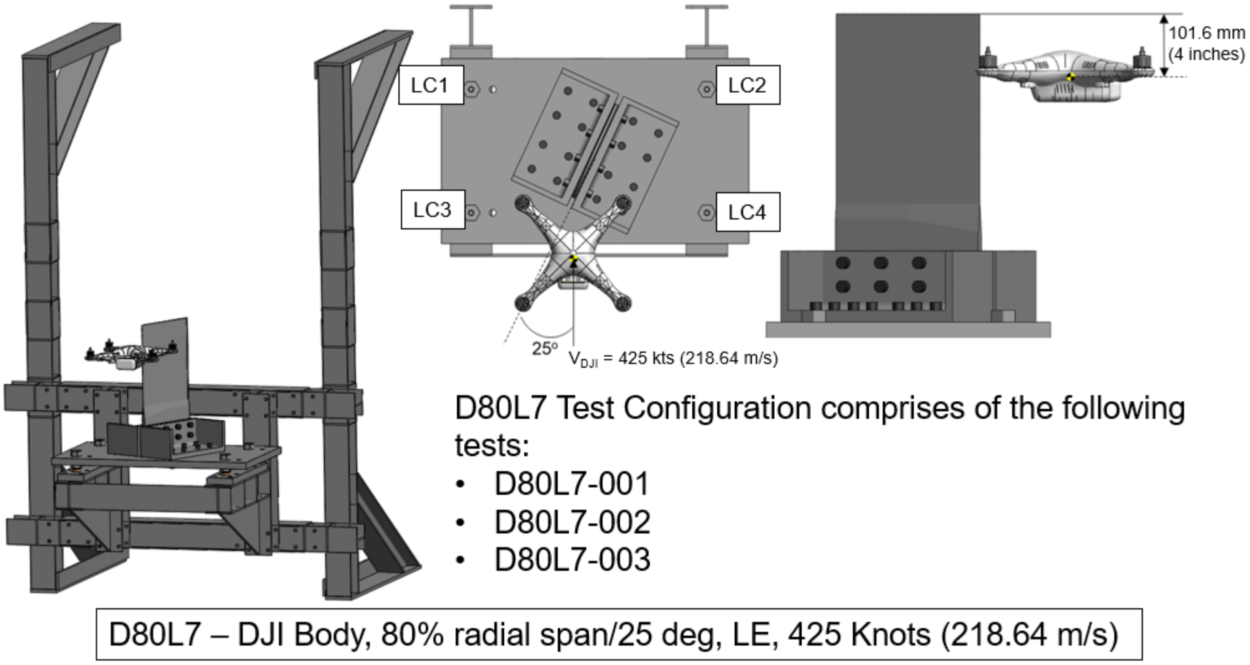

D80L7 Test Configuration comprises of the following tests:

- D80L7-001
- D80L7-002
- D80L7-003

D80L7 – DJI Body, 80% radial span/25 deg, LE, 425 Knots (218.64 m/s)

Figure 32. D80L7 test configuration setup.

The simulations were set up to match the testing conditions for all the tests shown in

Table 6.

Table 6. D80L7 test conditions.

Test Case	Actual Impact Velocity	UAS Pitch	UAS Roll	UAS Yaw	Impact Location w.r.t UAS C.G.
D80L7-001	403 kts (207.32 m/s)	-45 deg	25 deg	-8 deg	2.5 in. from the top of the blade
D80L7-002	394 kts (202.69 m/s)	46 deg	25 deg	25 deg	Only one arm of the UAS hit the blade LE
D80L7-003	433 kts (222.75 m/s)	-37 deg	-11.6 deg	6.4 deg	2.5 in. from the top of the blade

Figure 33 to Figure 35 show the top view kinematics comparison between the D80L7 tests and simulations from the start to the end of the impact. Three instances were compared. The first instance at t=0s is the start of the simulation before the impact. The second instance at t=0.001s is during the impact. The last instance at t=0.002s is after the impact.

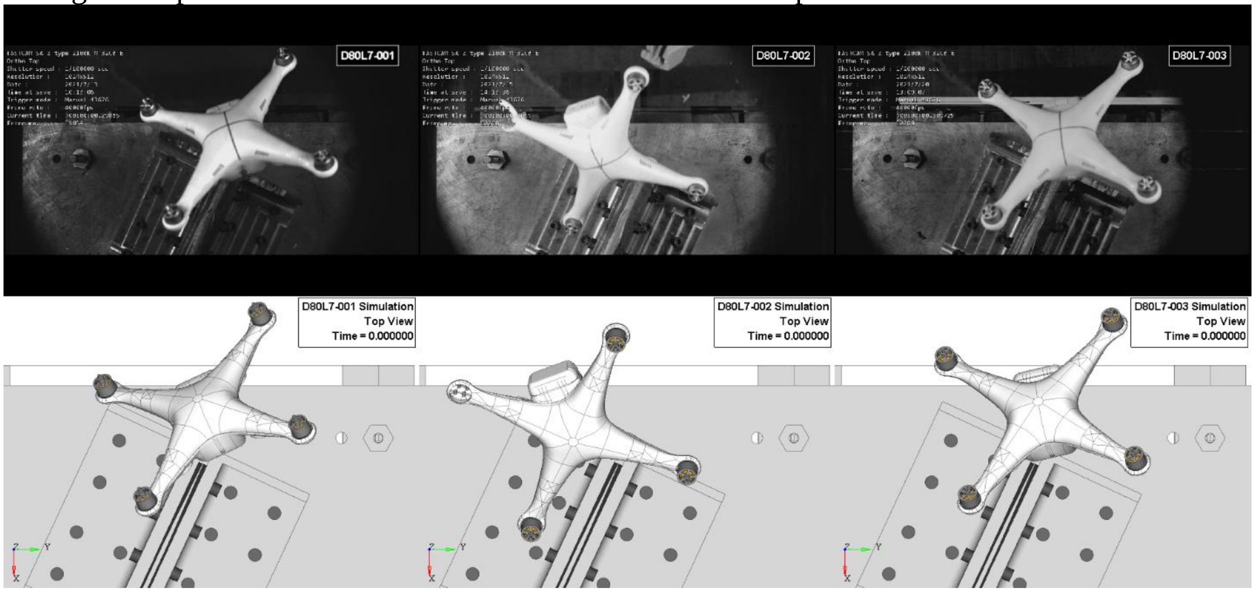

Figure 33. D80L7 tests top view kinematics comparison at t=0s.

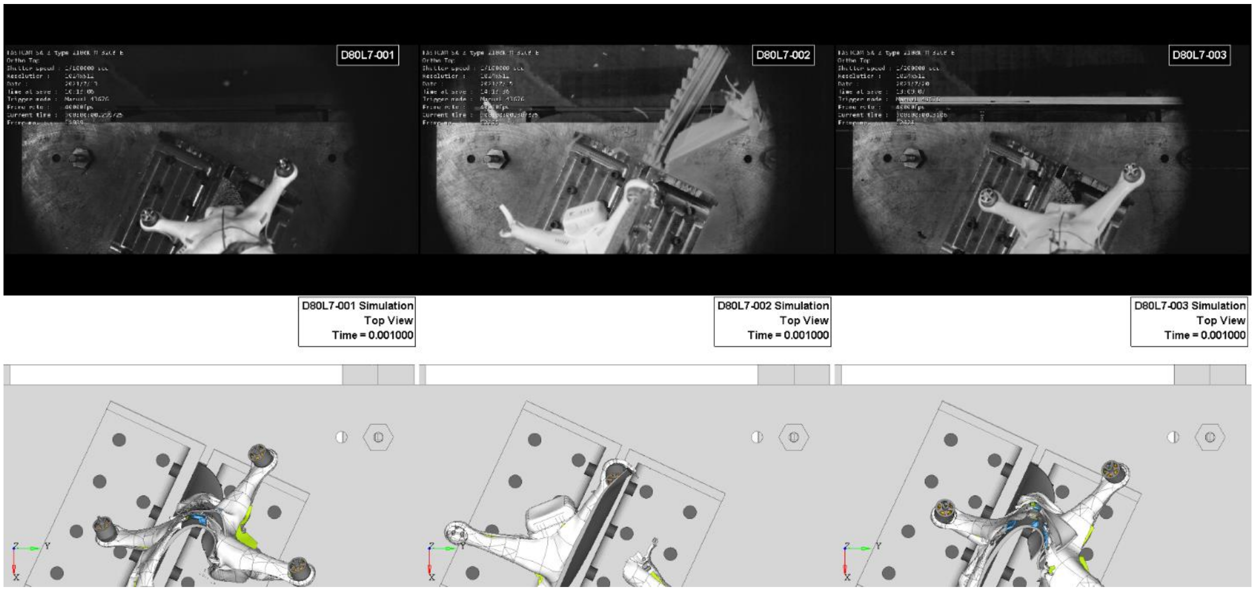

Figure 34. D80L7 tests top view kinematics comparison at t=0.001s.

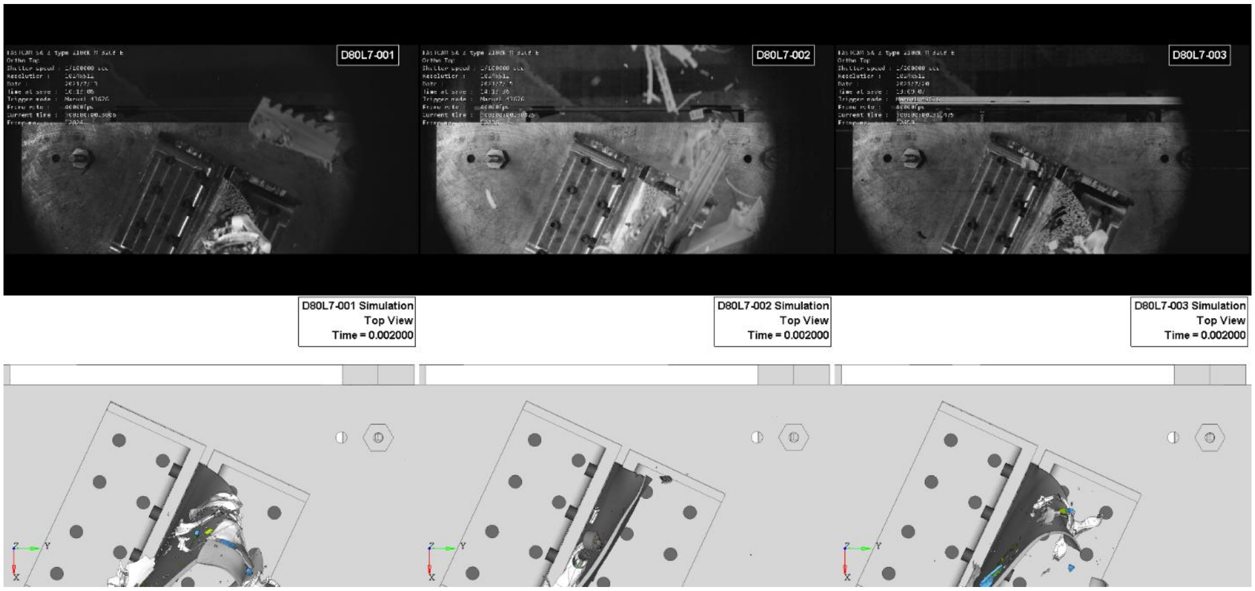

Figure 35. D80L7 tests top view kinematics comparison at t=0.002s.

All the simulations show that the blade continued vibrating after 2ms due to the impact's residual energy. Thus, an additional spring back analysis was performed on the blade to obtain its final deformed shape at its equilibrium state. Figure 36 compares the final blade damage between the spring back analysis prediction and the physical test damage for all the tests. The FE result for the blade's LE shows a good correlation with the final deformed shape of the physical blade's LE.

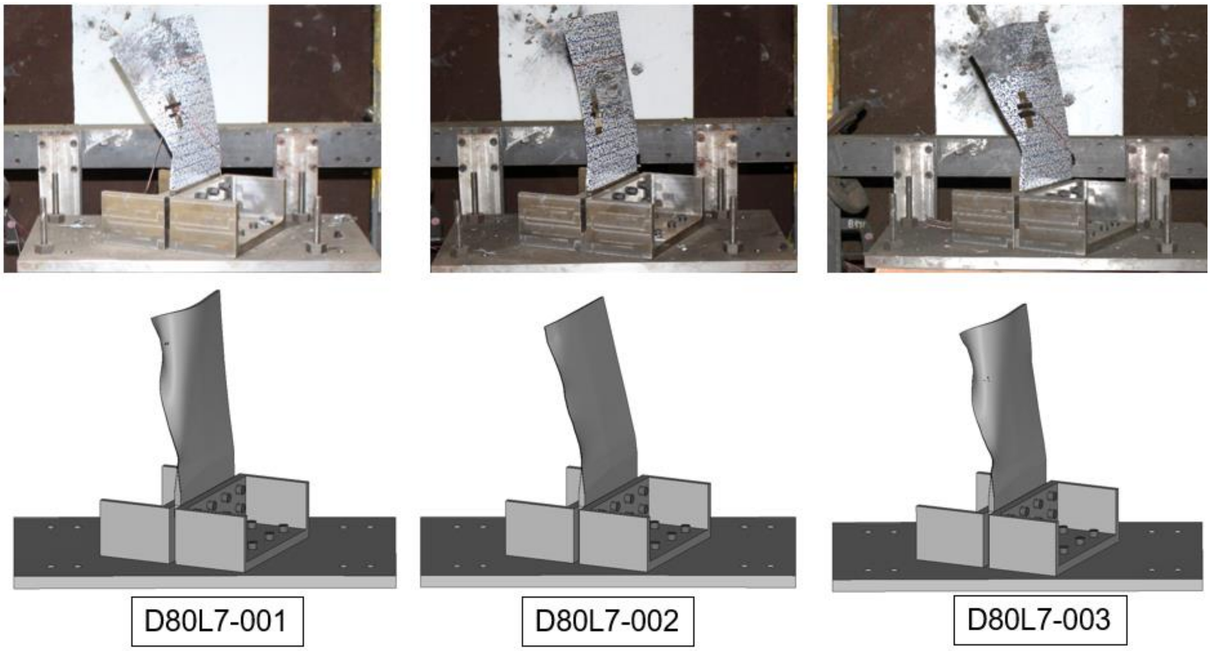

Figure 36. Spring back analysis prediction of blade damage vs. physical test damage for all D80L7 tests.

Similar difficulty observed in components level tests in processing DIC data was present for the full-scale tests. In fact, the UAS body being larger than its components, produced much more debris that covered most of the blade surface during the impact obstructing the DIC camera views. As a result, it was not possible to obtain good DIC contour data to compare with the simulations. Nevertheless, the time history of the resultant displacements from specific points on the blade surfaces was obtained and used to compare the simulation and the three D80L7 tests where possible. Due to the debris obstruction, the complete test time history curves were sometimes unavailable for the entire impact duration. Figure 37 to Figure 39 show these points' locations and the displacement comparison results for D80L7-001. Similar results can be found for the other impact cases and the complete results can be found in Annex B[16]. The comparison of point B (close to the impact area) shows some discrepancies after the impact with the UAS because of the low fidelity DIC data in the impact area, and the LE damage, although similar, is not identical between the test and simulation. Overall, the simulation displacement agrees well with the D80L7 tests for the duration of the impact. After the end of the contact, depending on the debris obstructions, some test data points show noticeable difference to the simulation results.

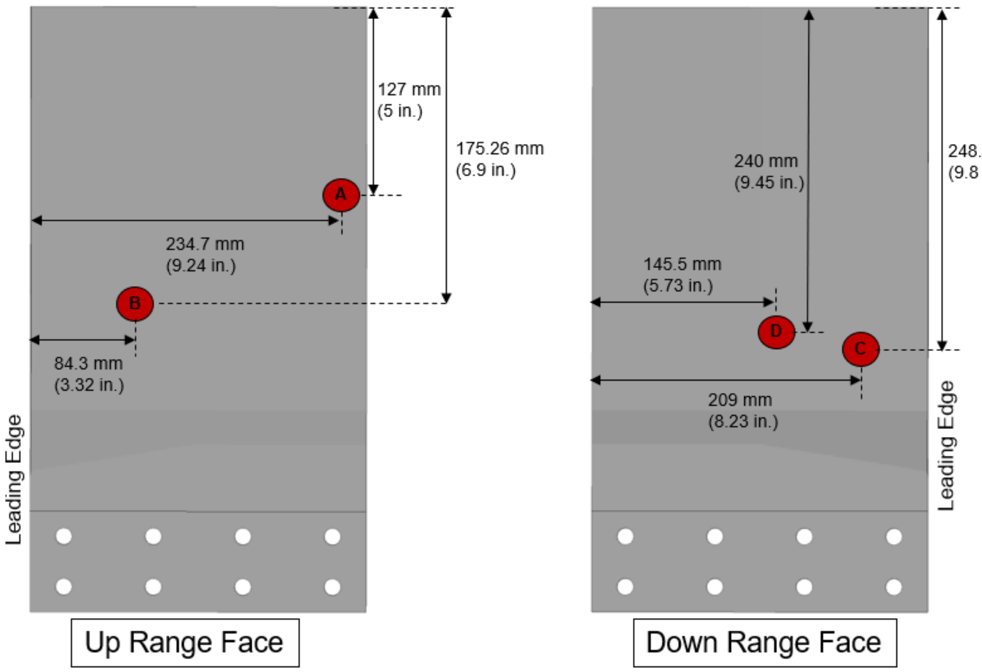

Figure 37. Location of points A,B,C, and D for extraction of DIC resultant displacement time history for test D80L7-001.

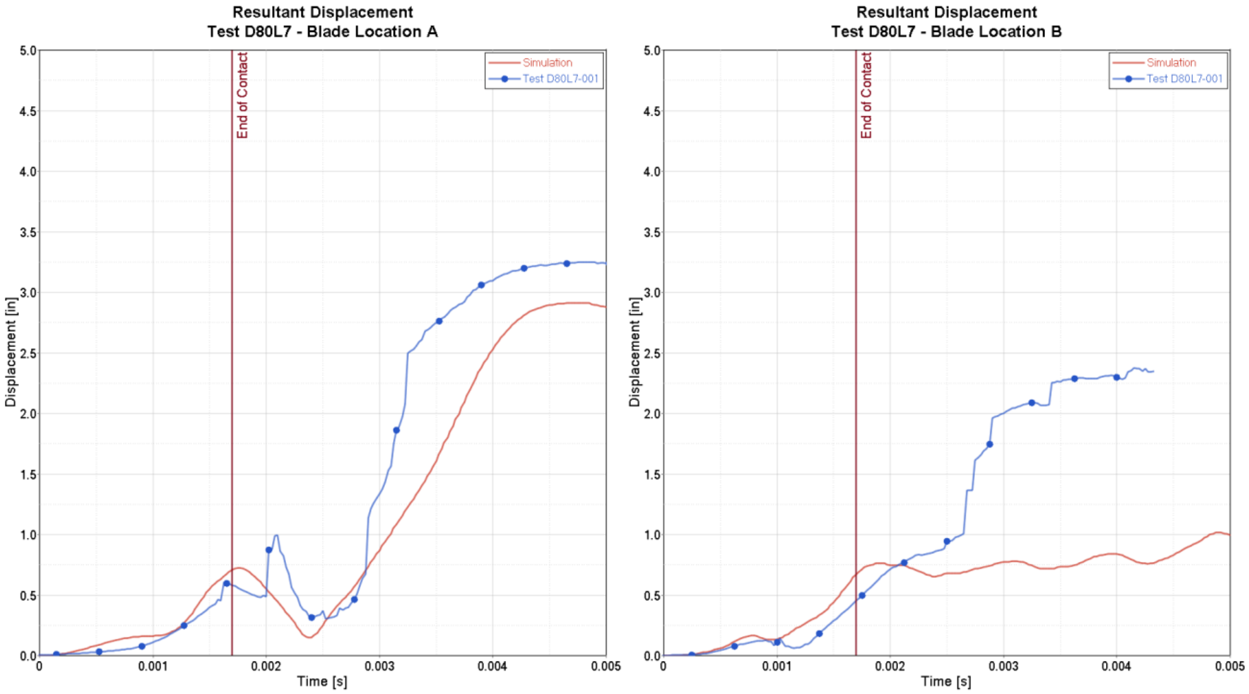

Figure 38. Resultant displacement of location A and B time history comparison between simulation and test D80L7-001.

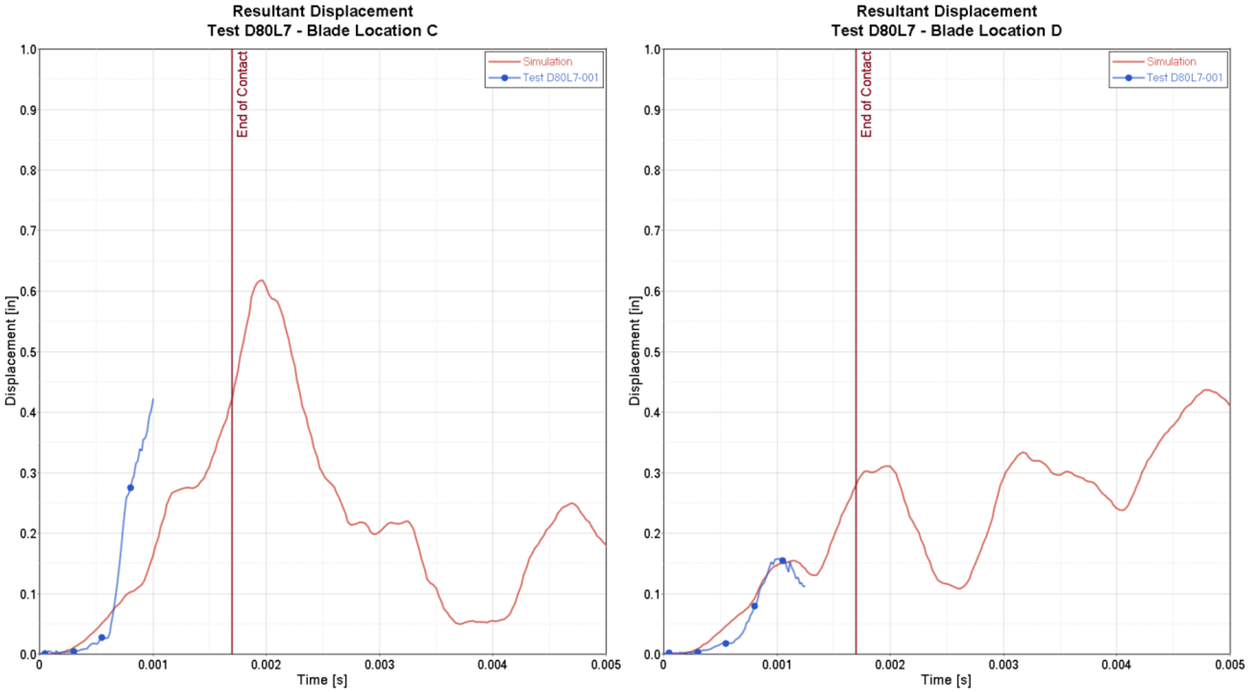

Figure 39. Resultant displacement of location C and D time history comparison between simulation and test D80L7-001.

Due to the data acquisition system not being triggered, there was no load cell test data for test D80L7-001. Figure 40 and Figure 41 show the load cells' data comparison between the simulation and the two remaining tests. The load cell 3 in test D80L7-002 experienced failure near the time of 0.004s resulting in the “noise” observed in Figure 40. The data has no filter, and its sampling rate was 1MHz for both the simulation and tests. The simulation results for the two remaining tests agree well with the test data. The strain gages' data comparison was not possible due to corrupted test data.

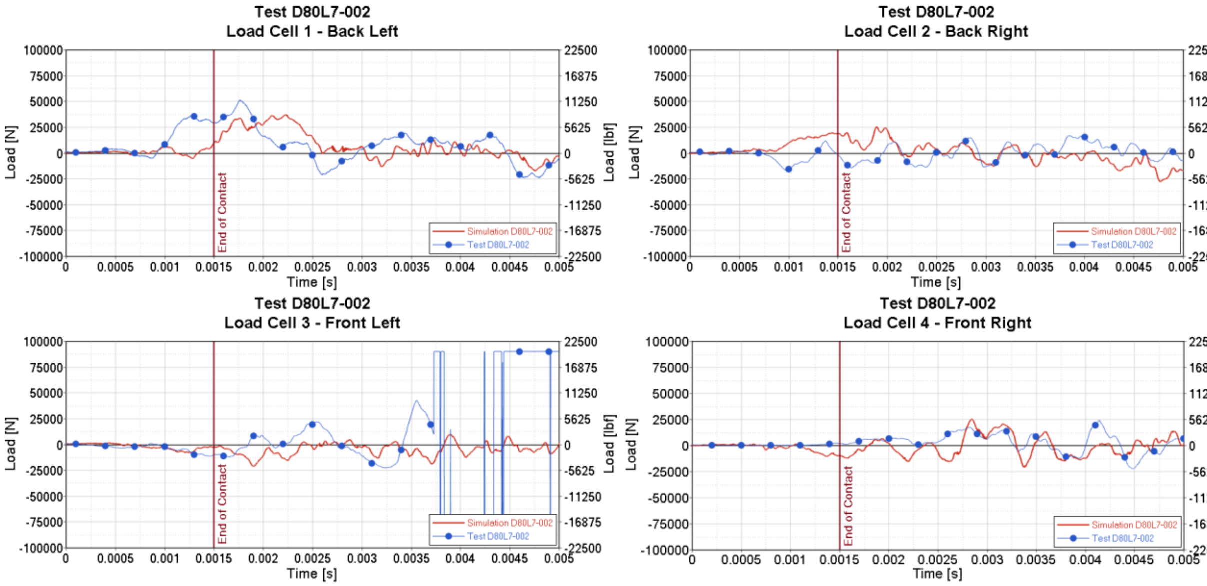

Figure 40. Test D80L7-002 load cells data comparison.

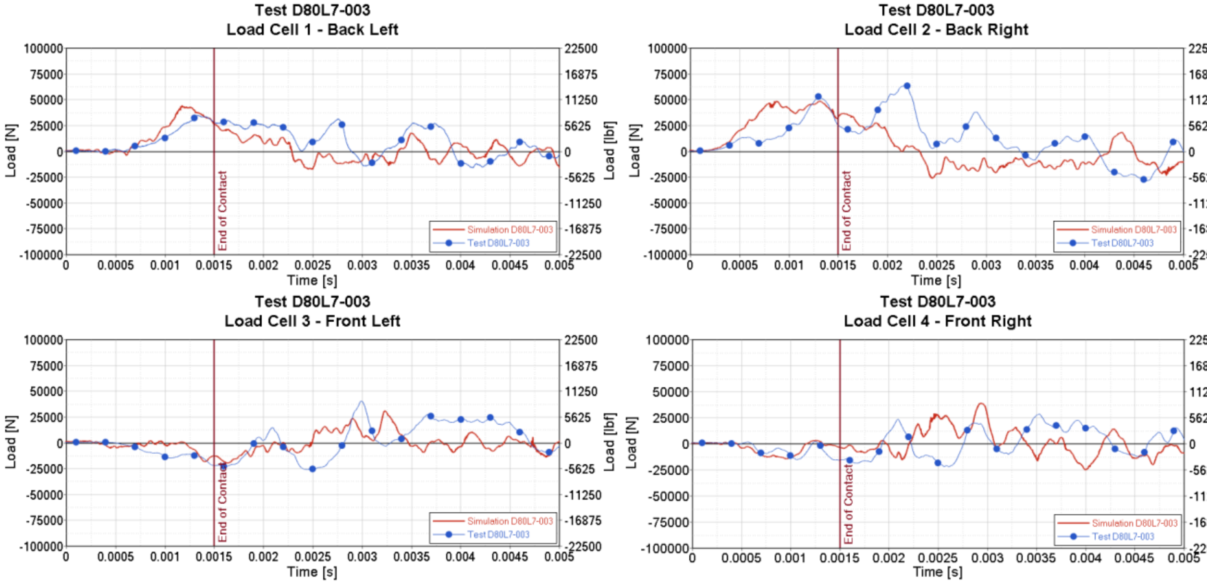

Figure 41. Test D80L7-003 load cells data comparison.

The results in this section show a good qualitative correlation between simulation and physical test data in terms of blade damage, loads, and DIC points' time histories. Thus, for this D80L7 configuration, the UAS body is considered validated.

Through the validation works documented in Section 6.2 and in Annex B[16], the full UAS FE model leveraged from A3[2] was updated with the validated key components (motor, battery, and camera) and considered validated under the current study conditions. Figure 42 shows the UAS geometry and the location of the updated components. Besides the updates of these components, the rest of the FE model definition remains the same as the one in the A3 program[2].

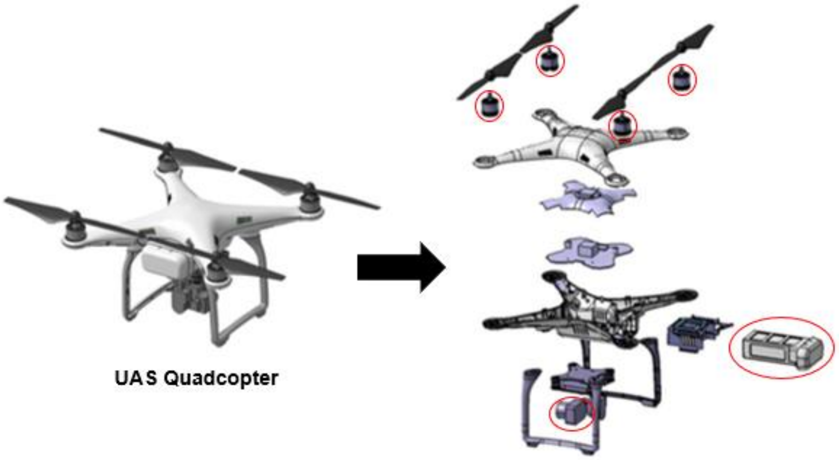

Figure 42. Geometry of UAS quadcopter and validated components (highlighted in red).

7. SUMMARY OF UAS INGESTION RESULTS

This section will discuss the results of the experimentally validated UAS model described in Section 6**Error! Reference source not found.** impacting the representative fan rig assembly model described in Section 5. First, the computational set-up of the ingestion simulations will be discussed in Section 7.1. Note that many of the settings and processes described in the bird ingestion simulation described in Section 5.4.3 were also used for the UAS ingestions in this section. Next, the data processing and analyses for the different cases are presented in Section 7.2. Then, the damage severity evaluation matrix is given in Section 7.3. After that the test matrix for the sensitivity study for a few cases are highlighted in Section 7.4. Section 7.5 then summarizes all the sensitivity study results identifying critical factors in the ingestion. Finally, the critical factors from the sensitivity study are used to run few phases of flight simulations with the expected worst-case conditions in Section 7.6.

7.1 SETTING UP THE INGESTION SIMULATIONS

For the UAS ingestion simulations, the fan was prescribed with the desired rotational speed after a pre-stress analysis was conducted (as described in Section 5.4.2). The UAS was given an initial orientation and placed with its center of mass at the desired radial span location. These locations were chosen such that the UAS would hit either towards the outer radius of the blade (without hitting the casing) or the inner radius of the blade (without hitting the nose cone) for each of the selected orientations. The nominal orientation of the UAS before it hits the fan is defined in Figure 43. Rotations of the UAS in roll, pitch and yaw angles from the nominal orientation are also shown in Figure 43. Motors of the UAS are shown in different colors, and the same color representation is used to plot the velocities of the motors in each simulations.

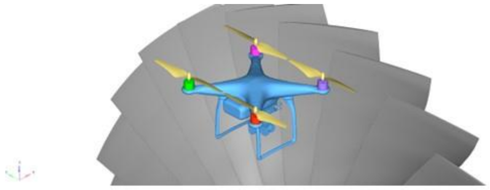

UAS nominal orientation

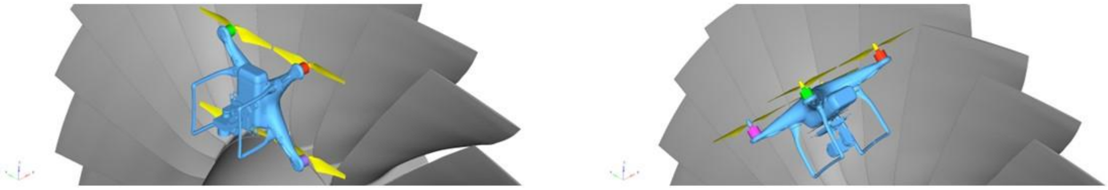

90° Pitch = UAS rotated 90° about y-axis

45° Roll = UAS rotated 45° about x-axis

45° Yaw = UAS rotated 45° about z-axis

180° Roll = UAS rotated 180° about x-axis

Figure 43. Orientation of UAS.

Note that the UAS shown in front of the fan in Figure 43 would be prescribed with the desired initial velocity normal to the face of the fan. Depending on the rotational speed of the fan and the translational speed of the UAS, the overall simulation times and the time when contact first occurs varies. For the high-speed fan rotations, one fan revolution was used. For the low-speed fan rotations, approximately half a revolution was used. Also, due to the complexity of the computational models and the resulting computational cost of the simulations, there was a need to delete the UAS after it passes through the fan for the remainder of the simulation.

7.2 ANALYSIS OF INGESTION SIMULATIONS

After the completion of each ingestion simulation, several types of analyses were conducted. First, several steps were taken to ensure the stability and accuracy of the solution. Then, the simulation data was processed in several ways to provide useful metrics to understand and compare the different ingestion scenarios.

To ensure the stability and accuracy of the solution, several steps were taken for each simulation. First, the animations of the simulations were carefully inspected to ensure that all the contacts were behaving properly, and parts of the UAS and fan did not fictitiously pass through each other. Also, the total energy in the system as well as energy in individual components were analyzed to ensure reasonable transmission of energy between components as well as the overall stability of the simulation.

To analyze and compare the results of the different ingestion simulations, several analyses were performed to assess the relative difference between cases in terms of (i) overall damage to the fan, (ii) imbalance in the rotor, (iii) loads on the retention systems, and (iv) containment.

(i) Two metrics will be used to understand the overall damage in the system. Both metrics are important in understanding the ability of the fan to continue to provide thrust. The first is a plot of the effective plastic strain in the fan at the end of the simulation. This will show the distribution of the damage over the entire fan surface and can be used to understand the localized damage in each blade to understand how close it is to failure. The second is a quantitative measure of the overall damage in the fan using the damage indicator D that is defined on each element as

$$D = \int \frac{\dot{\epsilon}_p}{\epsilon_{pf}} dt, \tag{1}$$

where $\dot{\epsilon}_p$ is the plastic strain evolution and ϵ_{pf} is the plastic failure strain. Note that D varies from 0 (no damage) to 1 (element failure) and is a measure of the cumulative plastic strain in the element. In order to get a quantitative assessment of the whole fan a mass weighted average of D is used for all elements to get a composite D_{fan}

$$D_{fan} = \frac{\sum_i^N m_i D_i}{\sum_i^N m_i}, \tag{2}$$

where N is the number of elements in the fan, m_i is the mass of the i^{th} element and D_i is the cumulative plastic strain in the i^{th} element. The D_{fan} metric quantifies the damage in the fan as a whole structure.

(ii) To understand the imbalance in the rotor due to the ingestion two analyses are carried out. Understanding the imbalance loads is important since it defines the structural and mount loads of the fan on the shaft. The first is to identify the center of gravity of each of the blades. A comparison of the pre- and post-impact center of gravities shows where damage occurs in the fan and how it relates to imbalance in the rotor. The second is to compute the forces in the disk that are acting on the rigid shaft. These forces give the overall imbalance load acting on the shaft.

(iii) To understand the loads on the retention systems several loads in the fan rig assembly model are tracked. Understanding retention loads is important to prevent the possibility of multiple blade release. First, the resultant force acting on each retainer based on its contact with the nosecone, dovetail and disk is computed using the RCFORC command in LS-DYNA. Second, the resultant force on the retention ring from its contact with the disk and dovetail was also computed using the RCFORC command. Finally, resultant forces and moments from a sectional plane in the dovetail and airfoil of a damaged and undamaged blade are also computed. Figure 44 indicates the airfoils and the plane where the forces and moments are computed.

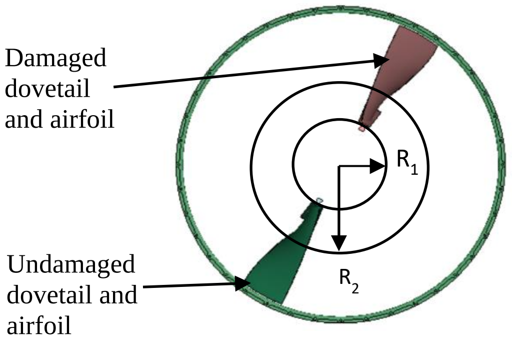

Radial distance of plane on dovetail (R_1) = 229 mm
Radial distance of plane on airfoil (R_2) = 369 mm

Figure 44. Damage and undamaged airfoil separated by 180 degrees and the sectional plane where the force and moments are computed.

(iv) To understand the relative difference between the UAS ingestions with relation to containment, the energy imparted to the casing is tracked using the MATSUM card in LS-DYNA. It is important to understand if the ingestion is likely to produce high energy debris beyond the capability of the containment system.

7.3 DAMAGE SEVERITY EVALUATION

The simulations conducted in this study are focused on understanding the effect of the UAS collision with an aircraft engine as it relates to damage in the fan in particular. This fan damage has implications on rotor imbalance, blockage (which impacts thrust), containment, and retainment mechanisms. Note that the fan rig assembly model does not contain most of the downstream components of the fan (i.e., compressor, combustor and turbine), and therefore any damage in these components is out of scope of this research.

The damage was separated into four severity levels based on discussion with the research team and the industrial partners and are detailed in Table 7. Table 7 has four columns: (i) the damage severity level; (ii) the fan damage and its corresponding likely effect on the engine; (iii) the corresponding aircraft operational impact for that same level of engine damage; and (iv) the typical associated damage in the fan for the damage severity level. Note that severity levels 1-3 are within the engine certification envelope and correspond to damage that would be typically seen up to a single blade-out event, which engines must be certified to be able to contain and shut down safely. Severity level 4 is outside the certification envelope, which means the engine is not certified for these damage levels but makes no claims about the danger or safety at this level since it is unknown.

Table 7. Damage Severity Level Classification.

Severity	**Fan (Engine) Damage**	**Aircraft Operational Impact**	**Typical Associated Damage**

Level 1	Slight damage – Continued operation with negligible to small reduced thrust Within engine certification envelope	Minimal effect – Continued flight to destination. Inspection after landing.	• Small deformation of fan blades • No crack initiation (blade or disk)
Level 2	Moderate damage – More significant reduced thrust Within engine certification envelope	Moderate effect – Continued flight or rerouting as needed. Inspection after landing.	• Significant deformation of fan blades • Material loss of leading edges of blades • Visible cracking in **single** blade above mid-span • No disk crack initiation
Level 3	Significant damage – Potential engine shutdown Within engine certification envelope	Significant effect – Fewer options for rerouting. Emergency landing may be needed if damage occurs at critical flight phase. Inspection after landing.	• Significant material loss leading to an imbalance that is less than or equal to a single blade loss • Visible cracking in **single** blade below mid-span • Visible cracking in **multiple** blades above mid-span • No disk crack initiation
Level 4	Damage outside of design criteria and certification – Potential hazardous engine effect Beyond engine certification envelope	Significant effect – Ranging from need to reroute to emergency landing to catastrophic failure. Inspection after landing.	• Significant material loss in blades leading to an imbalance that is more than a single blade loss • High energy forward arc debris • Visible cracking of **multiple** blades below mid-span • Crack initiation in **disk**

It is important to note that Table 7 is only providing an initial assessment of the fan damage and is not classifying overall engine damage (since the model does not include most of the downstream components of the engine). The four classification levels are meant to span a large range of outcomes and not all of these levels will necessarily occur in the cases investigated with this one specific UAS (i.e., a smaller UAS could result in less damage and larger UAS could lead to greater damage). Table 7 provides a general damage severity classification for the fan rig assembly that can be used in future studies.

7.4 SENSITIVITY STUDY

A test matrix was defined to study how different parameters of the ingestion affect the fan damage. Lessons from previous research on UAS ingestions into a generic fan model[3] were used to inform the selection of the test matrix. Namely, the focus of the ingestions is on the high fan speed rotation with the highest relative translational velocity of the UAS impacting at the outer radius. It has been shown in the previous research that the greatest damage is expected to occur in these scenarios since it results in the highest relative velocity between the fan blades and the UAS. However, each of these parameters (i.e., fan rotational speed, relative translational velocity, and radial impact location) were also investigated in this project. Moreover, several different UAS impact orientations were also considered. The test matrix used for the sensitivity study is shown in Table 8.

Table 8. Test matrix for sensitivity study.

Simulation ID	**Fan speed** (FS)	**Translational relative velocity** (RV)	**Radial Span** (RS)	**Orientation of UAS**
Fan Blade Out (FBO)	High	-	-	-
Bird (UAS mass)	High	High	High	-
LFS_LRV_LRS_90P	Low	Low	Low	90˚ pitch
LFS_LRV_HRS_Nom	Low	Low	High	0˚
LFS_HRV_LRS_90P	Low	High	Low	90˚ pitch
LFS_HRV_HRS_Nom	Low	High	High	0˚
HFS_LRV_LRS_90P	High	Low	Low	90˚ pitch
HFS_LRV_HRS_Nom	High	Low	High	0˚
HFS_HRV_LRS_90P	High	High	Low	90˚ pitch
HFS_HRV_HRS_Nom	High	High	High	0˚
HFS_HRV_HRS_45R	High	High	High	45˚ roll
HFS_HRV_HRS_90R	High	High	High	90˚ roll
HFS_HRV_HRS_45Y	High	High	High	45˚ yaw
HFS_HRV_HRS_90Y	High	High	High	90˚ yaw
HFS_HRV_HRS_180R	High	High	High	180˚ roll
HFS_HRV_LRS_Nom	High	High	Low	0˚

Note that for the fan speed, relative translational velocity and impact locations there is a high (H) and low (L) value assigned. For the fan speed, the high value corresponds to 5175 RPM, the max speed at take-off for this engine, while the low value corresponds to 1139 RPM, the rotational speed during approach for this engine. For the relative translational velocity, the high value corresponds to 250 kts (the maximum speed for an aircraft for flight below 10,000 ft.) and the low value corresponds to 130 kts, the minimum speed for take-off for this engine. The UAS was considered in the hover state with no translational velocity. For the radial impact location, the high and low correspond to the highest and lowest radial locations on the blade that can be impacted without directly hitting the nosecone or casing for the various orientations. Note that for the nominal orientation case the low value corresponds to the center of mass of the UAS impacting near the 10% radial span while the high value would impact near the 80% radial span. The different orientations correspond to rotations about the respective axis with respect to the direct orientation case, with those orientations defined in Figure 43.

In addition to the UAS ingestions two reference cases were also added for comparison purposes. The first is the blade-out simulation, since this serves as a useful reference point with regards to how much energy the containment system would need to be certified to contain and imbalance loads, etc. that the fan rig assembly model would need to handle to be certified for flight. The second case is a bird ingestion case where the bird model is similar to the one presented in Section 5.4.3 except that the weight has been scaled to match the UAS model weight of 1.22 kg (2.68 lbs).

The bird ingestion is at the high fan speed, high translational relative velocity and the center of mass impacts at about 80% radial span such that it is a good comparison point for many of the UAS impact cases from the sensitivity study.

A brief review overview of the reference cases (FBO and bird ingestion) and the UAS ingestion with the highest damage are highlighted before discussing the summary of all the cases in Section 7.5.

7.4.1 Reference 1: Blade-Out Simulation

Similar to bird ingestion requirements, the FAA requires new engine designs to demonstrate that they can contain a fan blade-out event by undergoing blade-out testing before they are certified. Due to the variety of proprietary containment systems used by each of the engine manufacturers, developing a truly representative containment system for the fan rig assembly model was outside the scope of this work. Instead, as was previously discussed, a casing that provides appropriate boundary conditions that would not restrict the ingestion of the UAV was used. Moreover, a reasonable hot clearance was used between the rotating blades and the casing, and the thickness of the casing was chosen so that it would be reasonable to withstand a high-speed blade impact for the selected titanium alloy.

The purpose of including this blade out simulation is to provide a reference for UAV simulations in terms of the amount of energy imparted to the casing as well as other loads acting on retention systems that occur during a blade-out event.

The FBO simulation was carried out with the pre-stressed model of the fan at the high fan speed of 5175 rpm (541.9 rad/s). For the FBO simulation, in accordance with industry standards, the first dovetail part is separated into two parts and the top platform section is rigidly tied with the airfoil root. The tied blade and dovetail section detach from the fan assembly at the start of the simulation (t = 0) and the fan is simulated for one full revolution.

The kinematics of the blade-out simulation is shown in Figure 45. The ejected blade is red and the two trailing blades are orange.

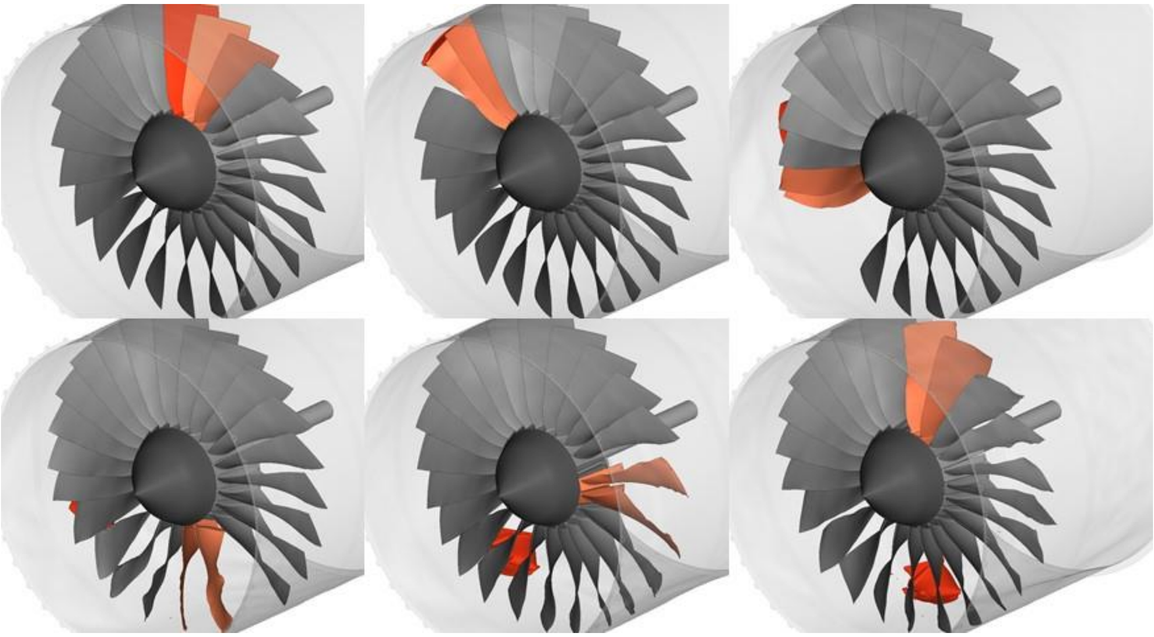

Figure 45. Kinematics of blade out event.

The effective plastic strain in the fan is shown in Figure 46.

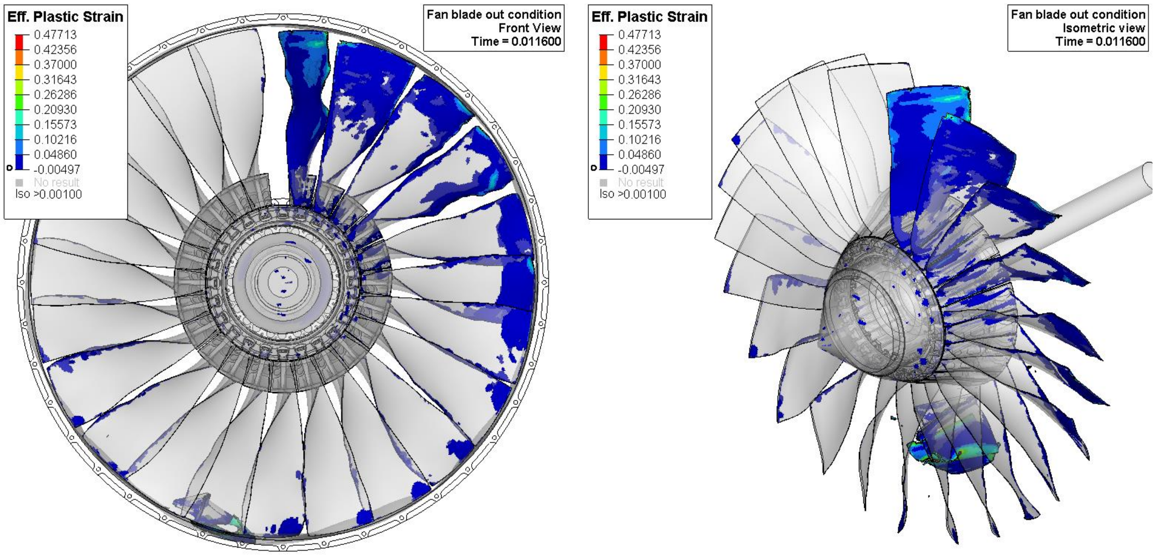

Figure 46. Effective plastic strain after a blade-out event.

Each blade's radial center of mass comparison pre- and post-blade-out are shown in Figure 47. The fan model post-blade-out is also shown for comparison. The damage level *D* (defined in Section 7.2) in the area of the fan with the most damage after the FBO event is also shown. The damage correlates well with the effective plastic strain. The loss of a blade and platform as well as the deformation in the other blades corresponds to damage severity level 3.

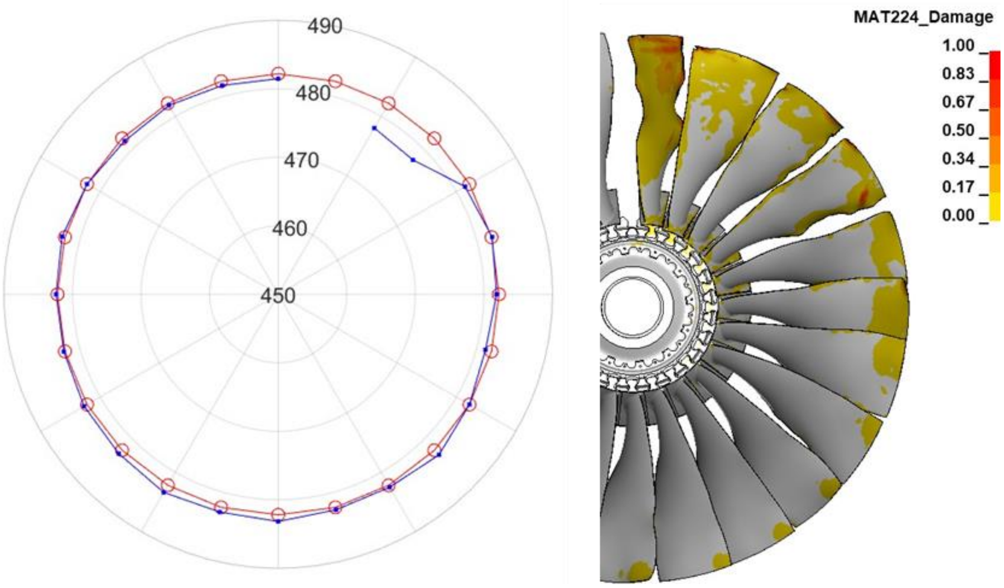

Figure 47. Center of mass of blades and fan model post blade-out.

7.4.2 Reference 2: Bird Ingestion Simulation

The bird ingestion simulation was carried out with very similar conditions as many of the UAS ingestions with a high fan speed, high relative translational velocity and high radial span location with a 1.22kg (2.68 lb) bird. The bird has the same properties as the bird discussed in Section 5.4.3 with a smaller mass equal to that of the UAS. The kinematics of the ingestion are shown in Figure 48.

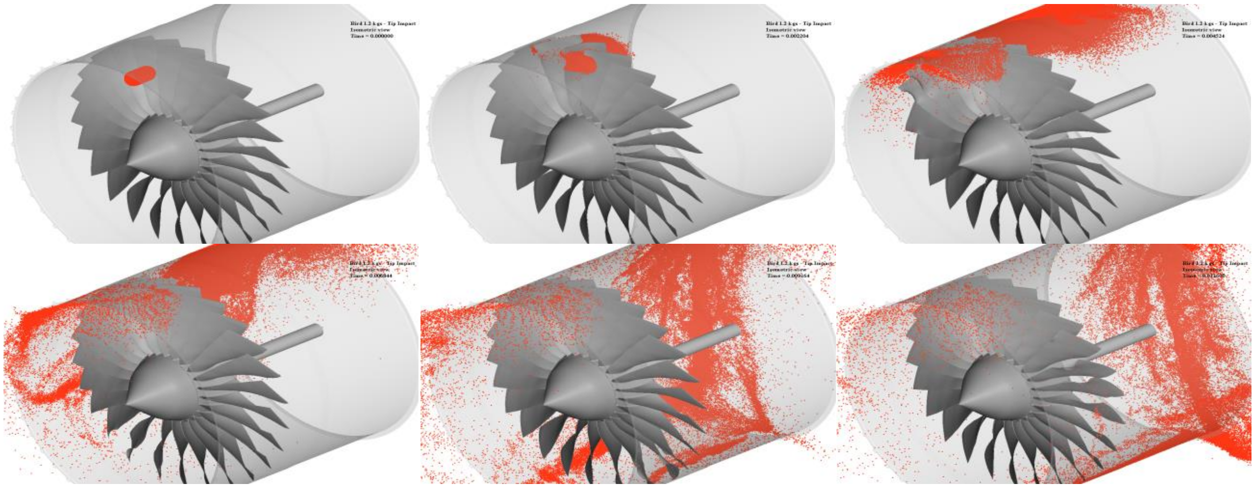

Figure 48. Kinematics of bird ingestion simulation.

The effective plastic strain in the fan is shown in Figure 49. There is significant deformation and cupping of the leading edges of multiple blades.

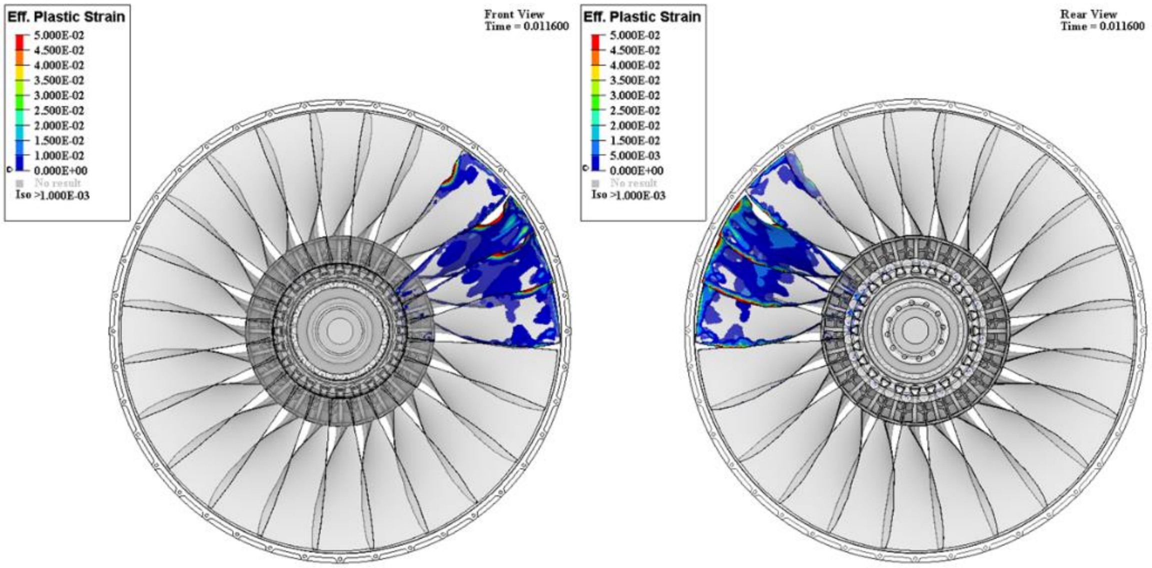

Figure 49. Effective plastic strain after a bird ingestion simulation.

Each blade’s radial center of mass comparison pre- and post-blade-out are shown in Figure 50. The damage level D (defined in Section 7.2) in the area of the fan with the most damage after the bird ingestion is also shown. The damage correlates well with the effective plastic strain. The significant plastic deformation and cupping of the leading edge of multiple blades corresponds to damage severity level 2.

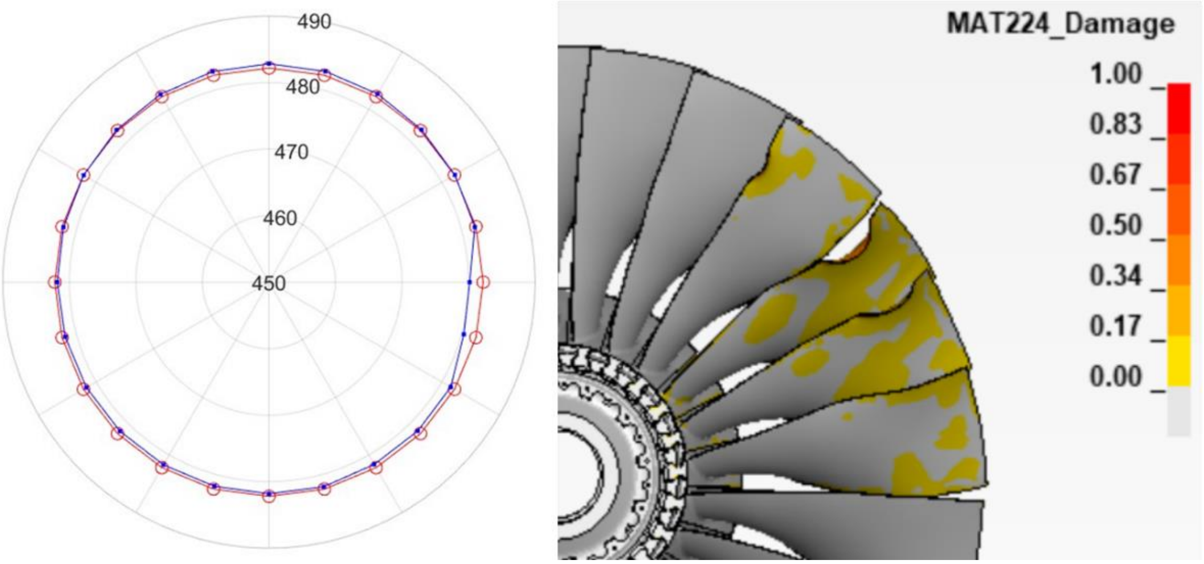

Figure 50. Center of mass of blades and fan model after bird ingestion.

7.4.3 Simulation HFS_LRV_HRS_Nom

This case corresponded to a UAS ingestion with a high fan speed, low relative translational velocity, high radial span location, and the nominal orientation (see Figure 43). The kinematics of the ingestion are shown in Figure 51. In all of the high fan speed simulations the fan was simulated for a full fan rotation, about 11.6 ms. The UAS parts were also deleted in these cases once they had cleared the fan region, in this case at approximately 7 ms, to improve the computational efficiency of the simulation.

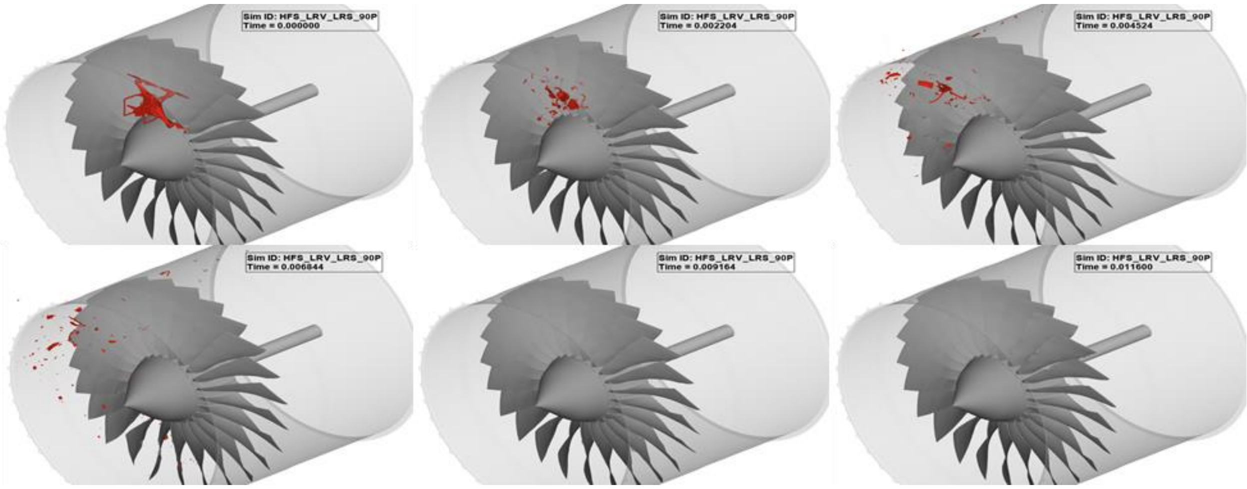

Figure 51. Kinematics of UAS ingestion simulation HFS_LRV_HRS_Nom.

The effective plastic strain in the fan at the end of one fan rotation is shown in Figure 52 (front and rear views).

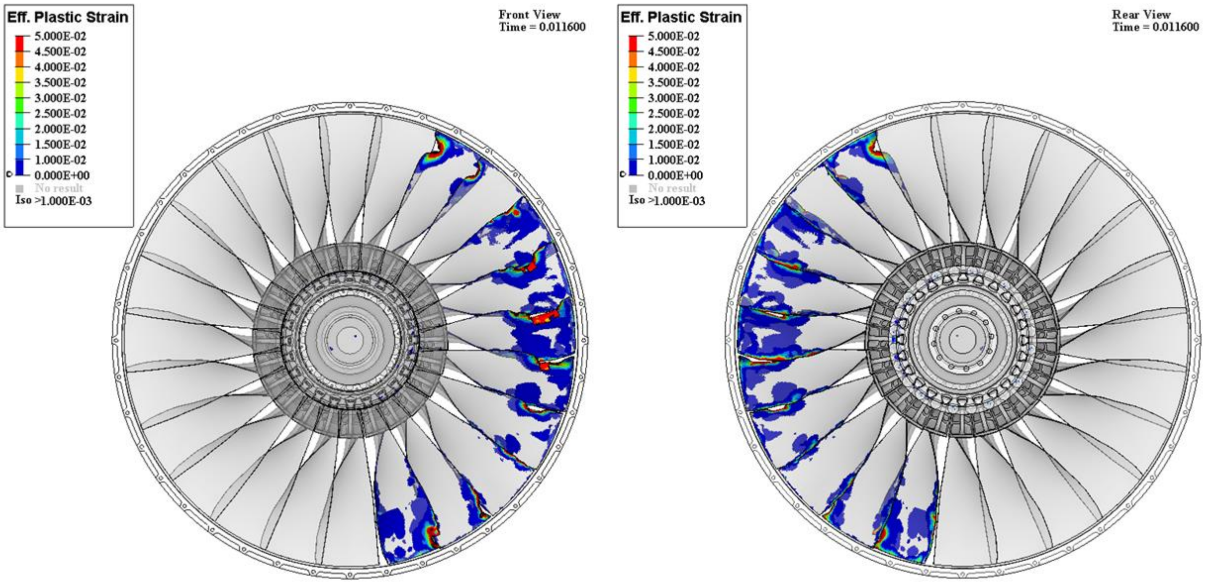

Figure 52. Effective plastic strain after UAS ingestion simulation HFS_LRV_HRS_Nom.

Each blade's radial center of mass pre- and post-ingestion are shown in Figure 53. The damage level D (defined in Section 7.2) in the damaged area of the fan model after the UAS ingestion is also shown. The damage clearly shows significant material loss on the leading edge of multiple blades, this corresponds to damage severity level 3.

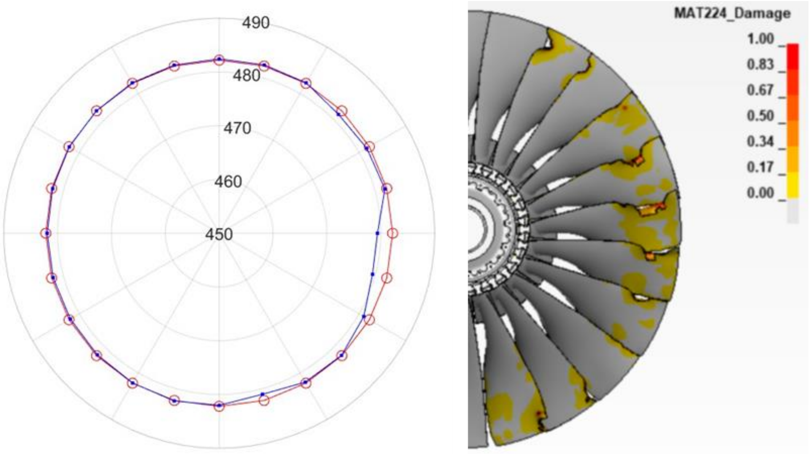

Figure 53. Center of mass of blades and fan model damage after UAS ingestion simulation HFS_LRV_HRS_Nom.

7.5 SUMMARY OF SENSITIVITY STUDY RESULTS

In this section, each of the cases from the sensitivity study are compared based on their overall damage in the fan, imbalance loads, forces on retention systems, and energy imparted to the casing and then the severity evaluation is given for each case.

The overall damage in the fan D_{fan} defined in Eq. (2) for each of the cases is summarized in Figure 54. Note that the FBO simulation is approximately 0.045. This is to be expected since it includes the loss of a full blade and platform (1/24 = 0.0417) and the plastic deformation of the adjacent blades that come into contact with it.

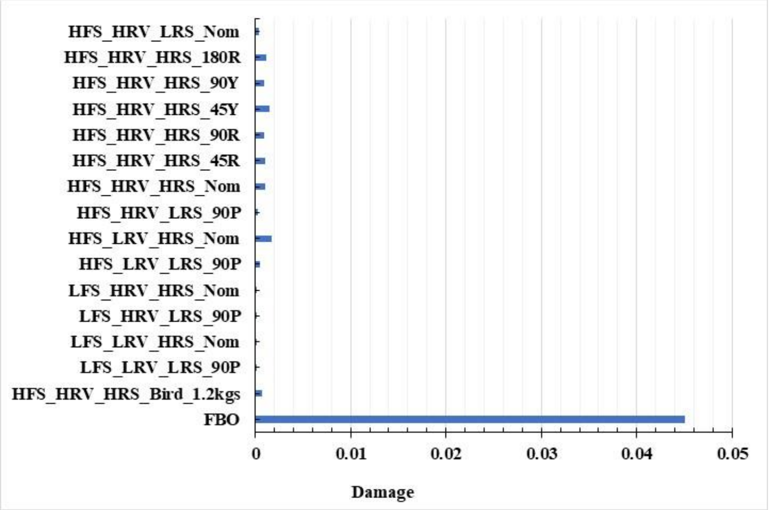

(a) D_{fan} for all cases

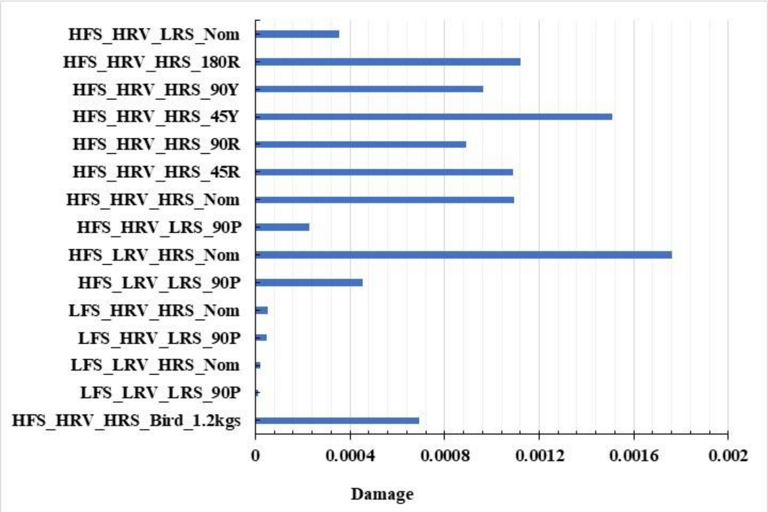

(b) D_{fan} for all cases except FBO

Figure 54. Comparison of damage levels for each of the cases.

First, it should be noted that the high fan speed case consistently has significantly more damage than the low fan speed, which is expected since the impacts happen at a much higher speed imparting more energy into the UAS and fan blades. Second, the higher radial span impact causes significantly more damage than the lower radial span impact since at the higher radial span the relative velocity between the UAS and fan blades is much higher than at the lower radial span. Third, the case that causes the most damage to the fan is the lower translational relative velocity case HFS_LRV_HRS_Nom. This is due to the fact that the additional energy from the translational velocity for the UAS at the high fan speed and high radial span is less significant for this case, and the fact that it actually does not pass through the fan quickly leads to more blades impacting the UAS and being damaged. This factor is not consistent for all cases. If one were to consider the lower fan speed and high radial impact location, the high translational relative velocity case (i.e., LFS_HRV_HRS_Nom) does more damage to the fan than the lower translational relative velocity case (i.e., LFS_LRV_HRS_Nom) because at lower fan speeds the relative translational velocity is significant. Finally, in comparing the orientations the 45-degree yaw orientation caused the most damage by a significant margin for the HFS_HRV_HRS condition.

The loads acting on the shaft due to the impact and imbalance over time is shown in Figure 55. A node set is defined at the rear of the disk to apply the axial boundary and disk rotation conditions. The resultant total force in different simulations is obtained using this node set through BNDOUT file output. It is clear that the FBO corresponds to a much larger imbalance than any of the cases investigated in the sensitivity study.

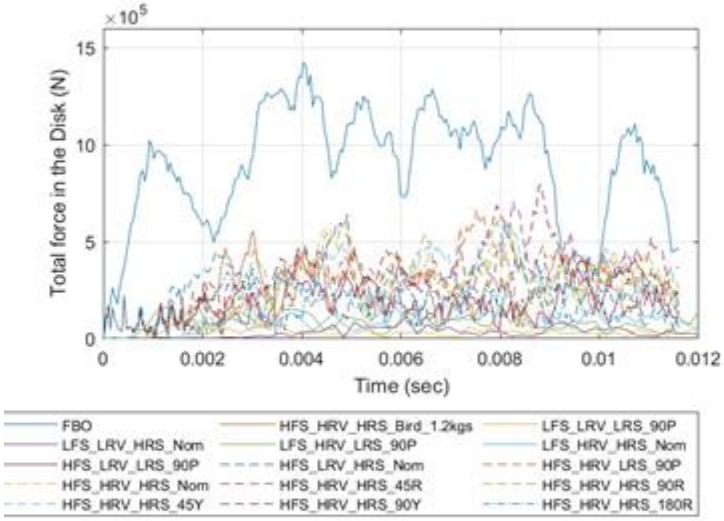

Figure 55. Forces acting from the disk on to the shaft due to the impact and imbalance loads.

The corresponding average and peak loads acting on the shaft are given in

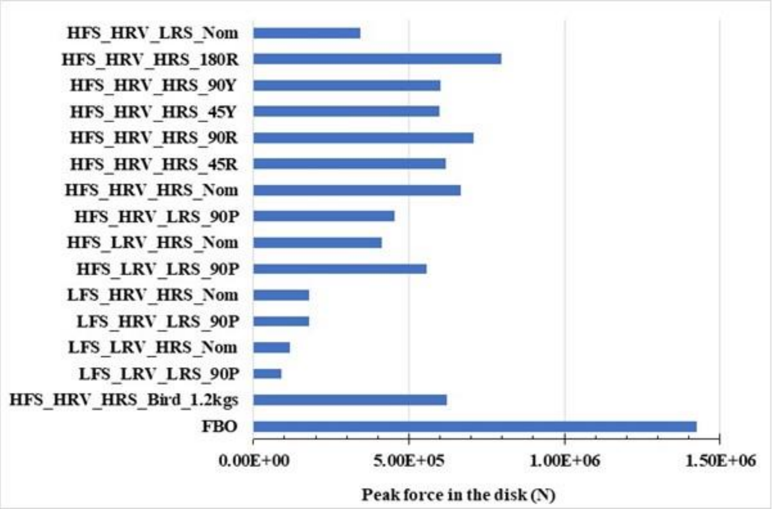

(b) peak force

Figure 56. This again highlights that the fan blade-out leads to higher imbalance loads than any of the UAS ingestion simulations. It should be noted that most of the high fan speed and high radial impact cases (UAS and bird) have a similar value. It should be noted that the imbalance does not directly correlate with the damage level in the fan (e.g., the bird ingestion has a fairly low damage level, but a relatively large imbalance due to the plastic deformation in some blades).

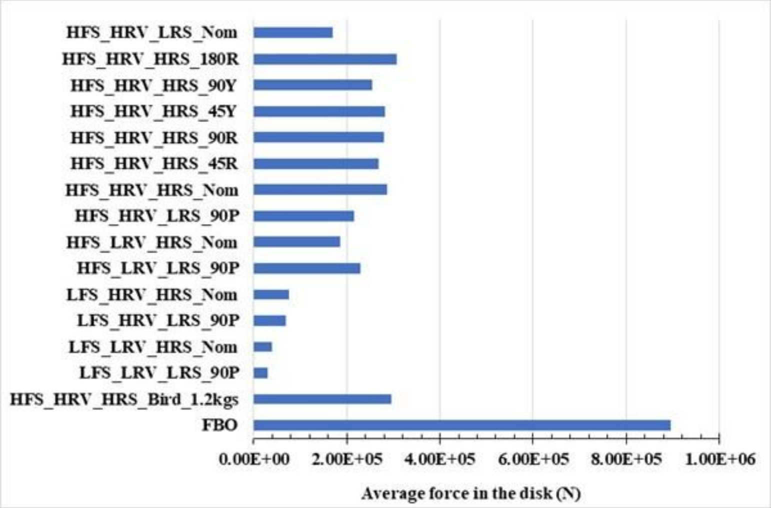

(a) average force

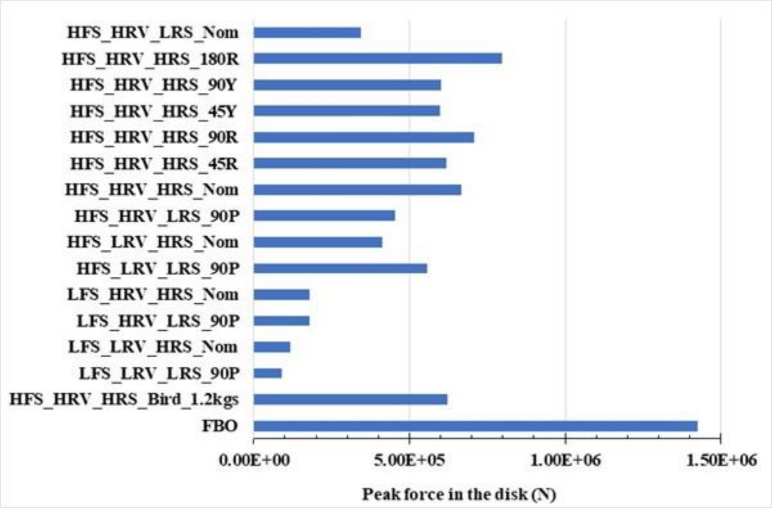

(b) peak force

Figure 56. Average force acting from the disk onto the shaft.

(a) The resultant forces on the retainer and retention ring over time are shown in Figure 57. Moreover, the average and peak loads on the retainer and retention ring are shown in

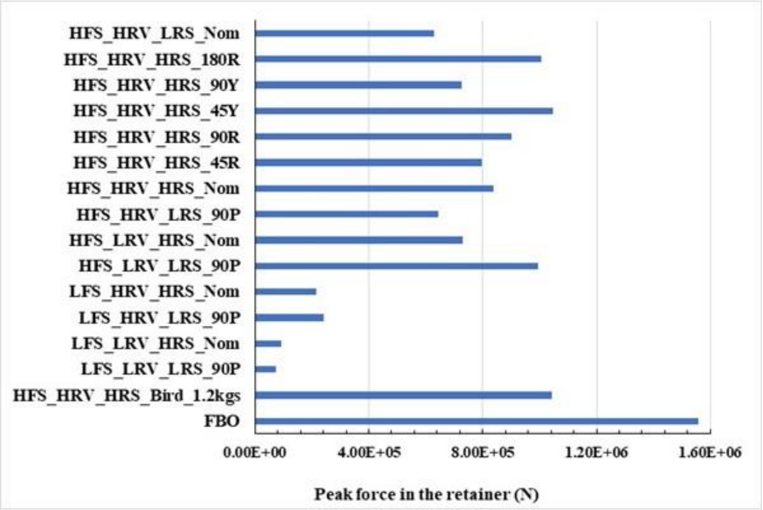

(b) peak force

Figure 58 and

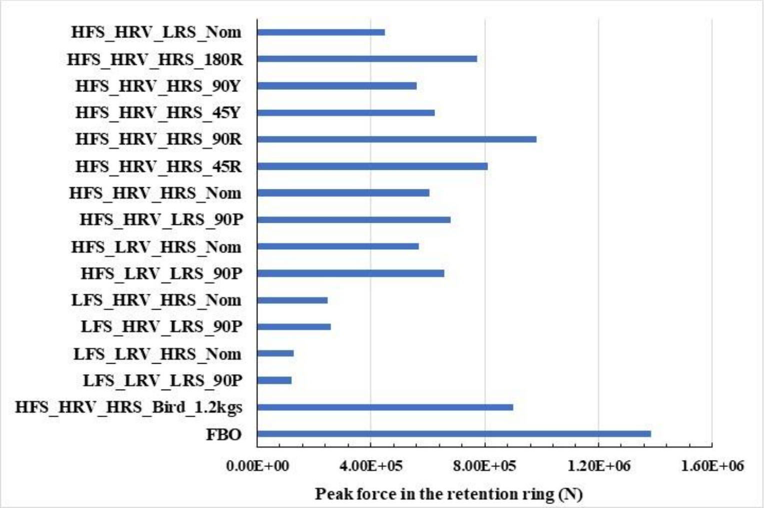

(a) peak force

Figure 59, respectively. It should be noted that the fan blade-out has a larger load for the retainer and the retention ring than the ingestion simulations. The bird ingestion simulation has a similar load as the UAS for the high fan speed, high translational relative velocity, and outer radial impact cases.

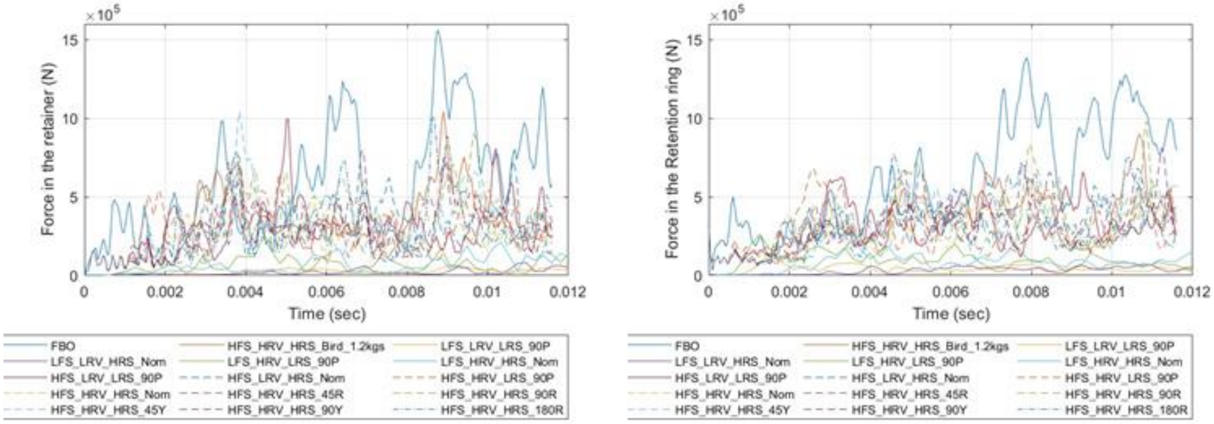

(a) retainer (b) retention ring

Figure 57. Resultant forces on the retainer and retention ring over time.

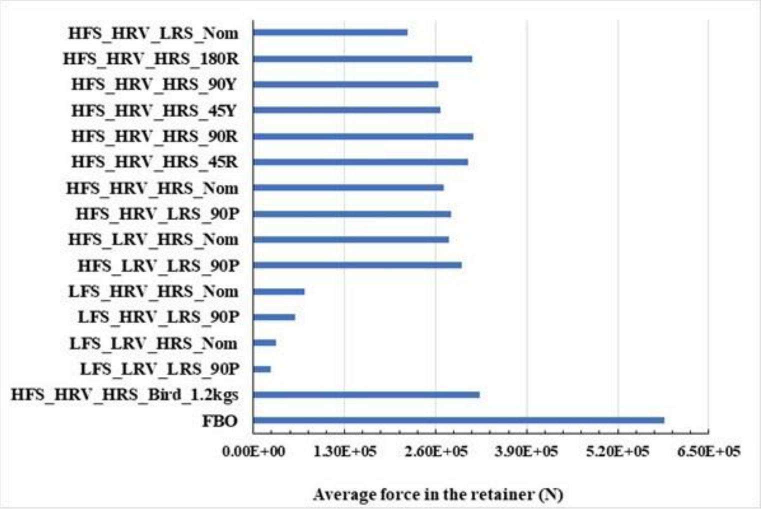

(b) average force

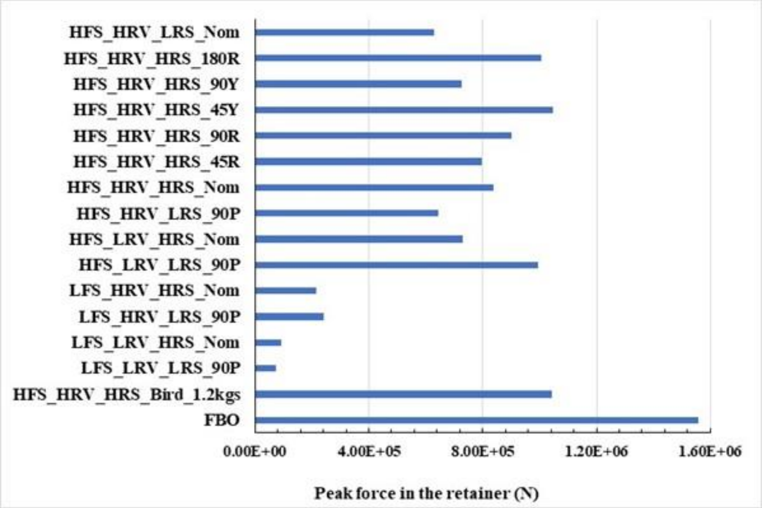

(b) peak force

Figure 58. Average force acting on retainer.

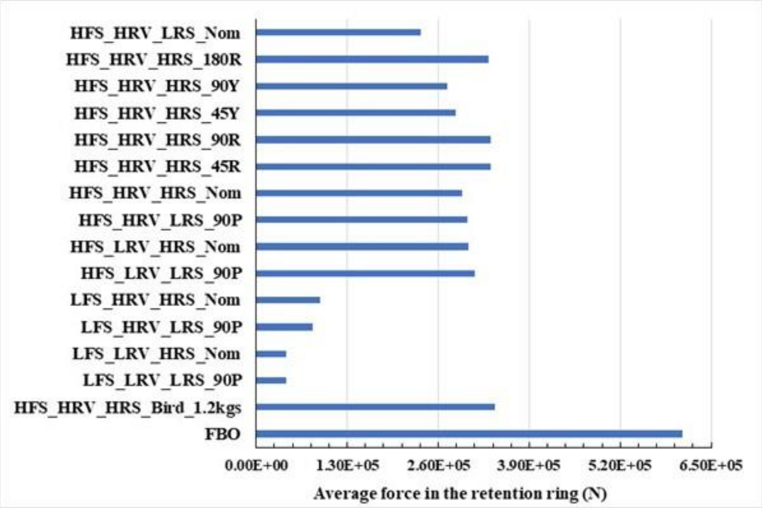

(b) average force

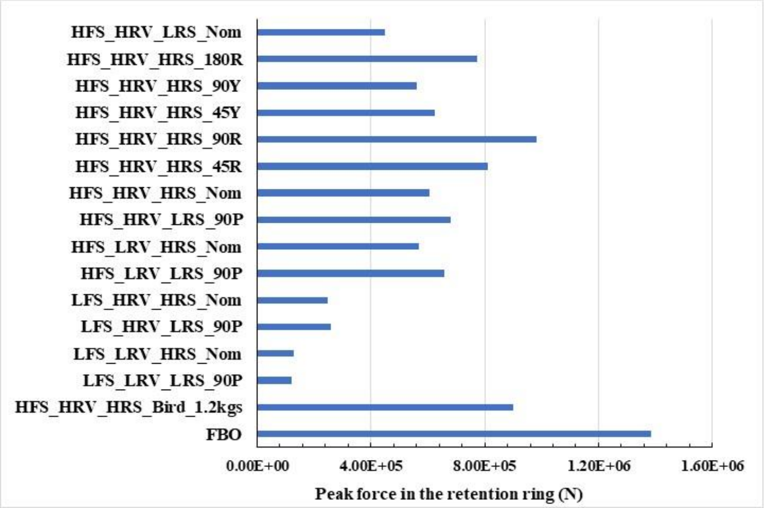

(c) peak force

Figure 59. Average force acting on retention ring.

The average energy imparted to the casing is shown in Figure 60. From these results the energy imparted to the casing is much lower than the FBO case. It should be noted that no analysis was conducted to extrapolate the damage and material loss predicted by the end of the simulation. It should be noted that the kinetic and internal energies in the casing have very similar values for most of the cases, which has been reported before[25].

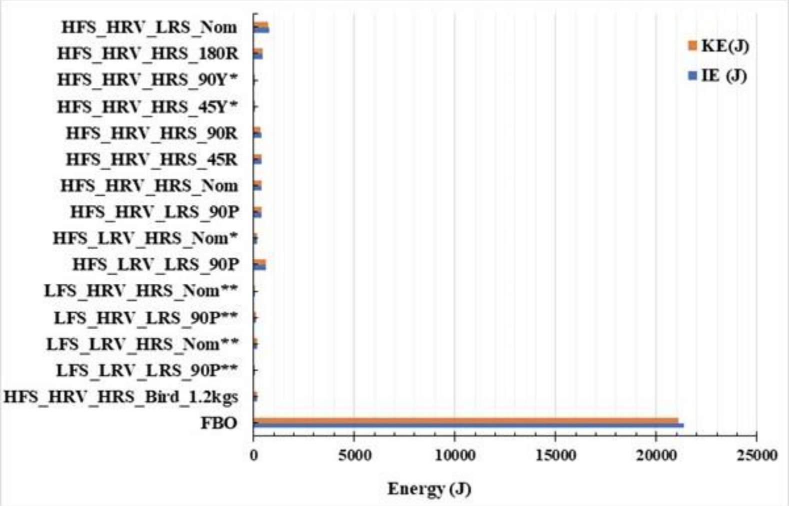

(a) all simulations

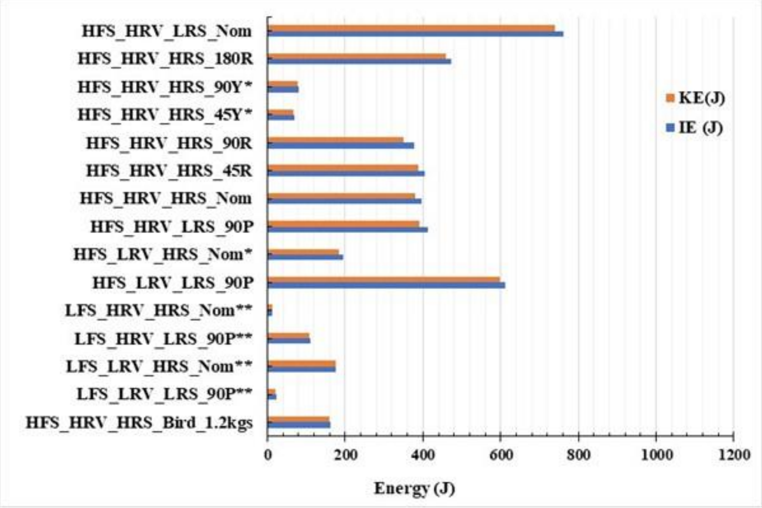

(b) all simulations except FBO

Figure 60. Average energy imparted to casing (* indicates that the UAS parts are deleted as they moved away from the fan model and prior to many parts hitting the casing, ** indicates simulations at different time scales, since low fan speed simulations are conducted for less than a fan rotation).

A summary of each of the simulations and severity level evaluation from Table 7 is given in Table 9. The largest forces in the disk and retention systems, and highest damage in the fan is for the FBO case. Note that the comparison of the UAS ingestion cases with the FBO is done since that is part of the current regulatory framework where engine designs are certified to demonstrate safe containment and shutdown from an FBO event. The largest for the ingestion cases are emphasized with the bold red font, and the second largest are denoted by the red font.

Table 9. Summary of sensitivity results and severity level evaluation.

Simulation ID	Average force in disk (N)	Average force in retention ring (N)	Average force in retainer (N)	Damage in blade model	Severity level	Associated damage
FBO	**8.98E+05**	**6.10E+05**	**5.86E+05**	**0.04508**	Level 3	Significant material loss leading to an imbalance that is equal to a single blade loss and additional plastic deformation
HFS_HRV_HRS_ Bird_1.2kgs	2.95E+05	**3.41E+05**	**3.24E+05**	0.000692	Level 2	Cupping of leading edge of multiple blades
LFS_LRV_LRS_90P	3.09E+04	4.27E+04	2.53E+04	1.04E-05	Level 1	Small deformation of blades and no crack initiation
LFS_LRV_HRS_Nom	3.84E+04	4.32E+04	3.18E+04	2.27E-05	Level 1	Small deformation of blades and no crack initiation

LFS_HRV_LRS_90P	6.96E+04	8.03E+04	5.99E+04	4.75E-05	Level 1	Small deformation of blades and no crack initiation
LFS_HRV_HRS_Nom	7.65E+04	9.09E+04	7.28E+04	5.24E-05	Level 1	Small deformation of blades and no crack initiation
HFS_LRV_LRS_90P	2.31E+05	3.12E+05	2.97E+05	0.000452	Level 2	Material loss and deformation along leading of multiple blades
HFS_LRV_HRS_Nom	1.85E+05	3.04E+05	2.79E+05	**0.001763**	Level 3	Significant material loss on leading edge of multiple blades
HFS_HRV_LRS_90P	2.16E+05	3.02E+05	2.82E+05	0.000227	Level 1	Small deformation of blades and no crack initiation
HFS_HRV_HRS_Nom	2.87E+05	2.94E+05	2.72E+05	0.001096	Level 3	Significant material loss on leading edge of multiple blades
HFS_HRV_HRS_45R	2.69E+05	3.35E+05	3.06E+05	0.001091	Level 3	Significant material loss on leading edge of multiple blades
HFS_HRV_HRS_90R	2.80E+05	3.34E+05	3.14E+05	0.000892	Level 3	Significant material loss on leading edge of multiple blades
HFS_HRV_HRS_45Y	2.81E+05	2.85E+05	2.67E+05	0.001509	Level 3	Significant material loss on leading edge of multiple blades
HFS_HRV_HRS_90Y	2.54E+05	2.73E+05	2.64E+05	0.000961	Level 3	Significant material loss on leading edge of multiple blades
HFS_HRV_HRS_180R	**3.08E+05**	3.32E+05	3.13E+05	0.00112	Level 3	Significant material loss on leading edge of multiple blades
HFS_HRV_LRS_Nom	1.71E+05	2.34E+05	2.20E+05	0.000353	Level 2	Material loss and deformation along leading of multiple blades

It should be noted that LS-DYNA is not a crack propagation tool (it is capable of accurately predicting damage, but it is not capable of predicting any subsequent fracture mechanics growth), and significant damage in the leading edge of the blades in some cases could lead, in practice, to breaking off of portions of such blades. The results being presented are focused on what is being providing by LS-DYNA and are not assessing the possibility of portions of the blades breaking off after the initial damage is initiated. So, in this way the results could be non-conservative since damage may progress due to crack propagation or aeromechanical effects, which could change the severity level evaluation of some cases.

Overall, the damage severity tracks closely with the D_{fan} parameter. The high fan speed case consistently has significantly more damage than the low fan speed, which is expected since the impacts happen at a much higher speed imparting more energy into the UAS and fan blades.

Second, the higher radial span impact causes significantly more damage than the lower radial span impact since at the higher radial span the relative velocity between the UAS and fan blades is much higher than at the lower radial span (which are severity level 1 or 2). All the high fan speed with high radial impact cases for the UAS ingestion are severity level 3 as opposed to the bird of the same mass which is severity level 2. The case that causes the most damage to the fan is the lower translational relative velocity case (with high fan speed and high radial span location), which has been previously noted. Finally, in comparing the orientations the 45-degree yaw orientation caused the most damage for the studied cases which is focused on the HFS_HRV_HRS condition.

7.6 PHASE OF FLIGHT INGESTION STUDIES

In general, there are three phases of flight where a manned aircraft is most likely to encounter a UAS: take-off, flight below 3,048 m (10,000 ft), and approach.

The take-off condition is a critical flight condition since the fan is rotating at full speed during this condition, which is the most important parameter with regard to damage to the fan as discussed in the sensitivity study. The outer radial span was another critical factor in understanding damage to the fan, so that will be the location chosen for this impact case. Also, it was determined that for this high fan speed the low relative translational velocity actually does more damage to the fan than the high translational velocity because more of the hard components like the motors and camera tend to impact more blades. Finally, the orientation that caused the most damage in the sensitivity study was the 45-degree yaw orientation case. The critical takeoff case can be designated as HFS_LRV_HRS_45Y.

The flight below 3,048 m (10,000 ft) has the fan rotating at 70% speed, which is a mid-level fan speed (MFS). The other options for this critical case will be chosen to match the take-off case. The critical flight below 3,048 m case can be designated as MFS_LRV_HRS_45Y.

The approach case has the lowest fan speed. From the sensitivity study it was shown that the low fan speed resulted in minimal damage. Due to the long computational time of these low fan speed simulations and understanding that minimal damage would occur, no additional approach case was simulated.

7.6.1 Takeoff: HFS_LRV_HRS_45Y

This case corresponded to a UAS ingestion with a high fan speed, low relative translational velocity, high radial span location, and the 45-degree yaw orientation (see Figure 43). The kinematics of the ingestion are shown in Figure 61. The simulation is focused on understanding the damage in the fan and was therefore focused on the impact of the UAS and fan and was terminated around 6 ms.

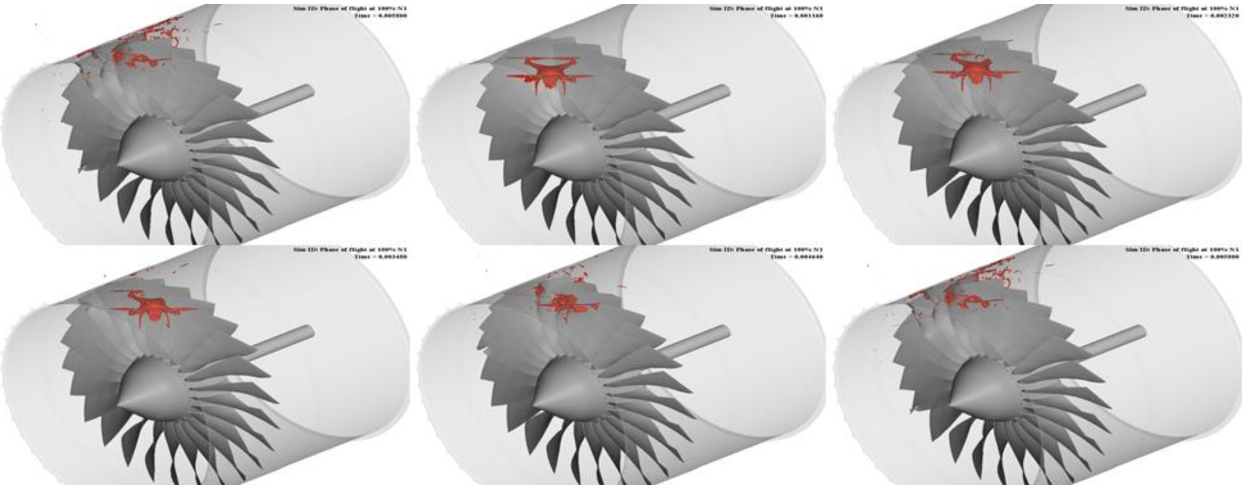

Figure 61. Kinematics of UAS ingestion simulation HFS_LRV_HRS_45Y.

The effective plastic strain in the fan at the end of the simulation is shown in Figure 62 (front and rear views).

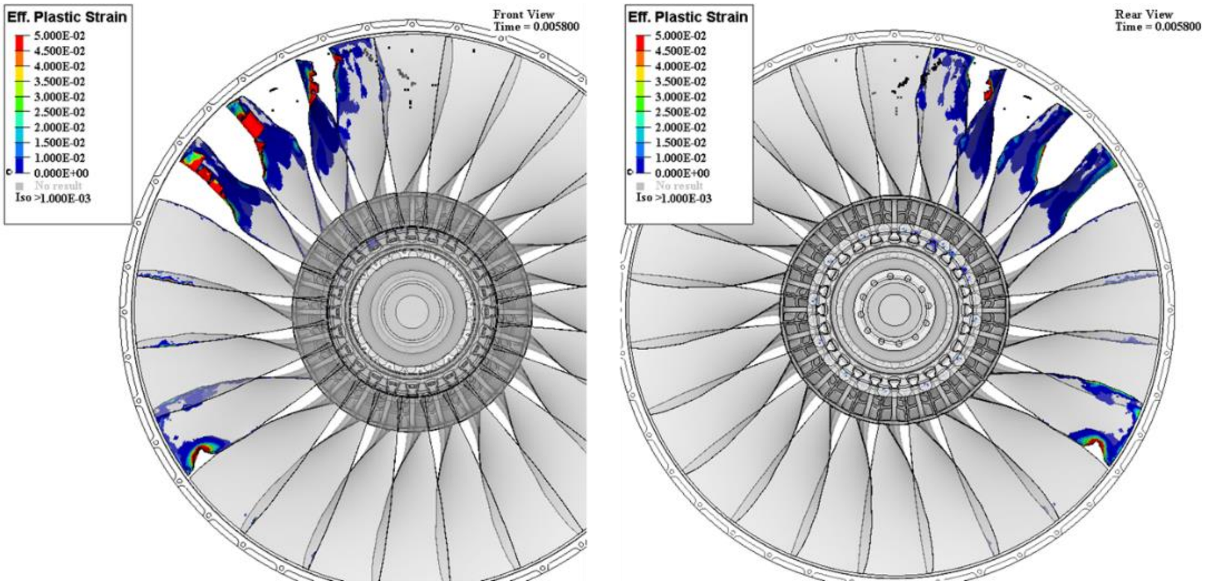

Figure 62. Effective plastic strain after UAS ingestion simulation HFS_LRV_HRS_45Y.

Each blade's radial center of mass pre- and post-ingestion are shown in Figure 63. The damage level *D* (defined in Section 7.2) in the damaged area of the fan model after the UAS ingestion is also shown. The damage clearly shows significant material loss on the leading edge of multiple blades, which corresponds to damage severity level 3, since the imbalance would be less than that of a loss of a full blade.

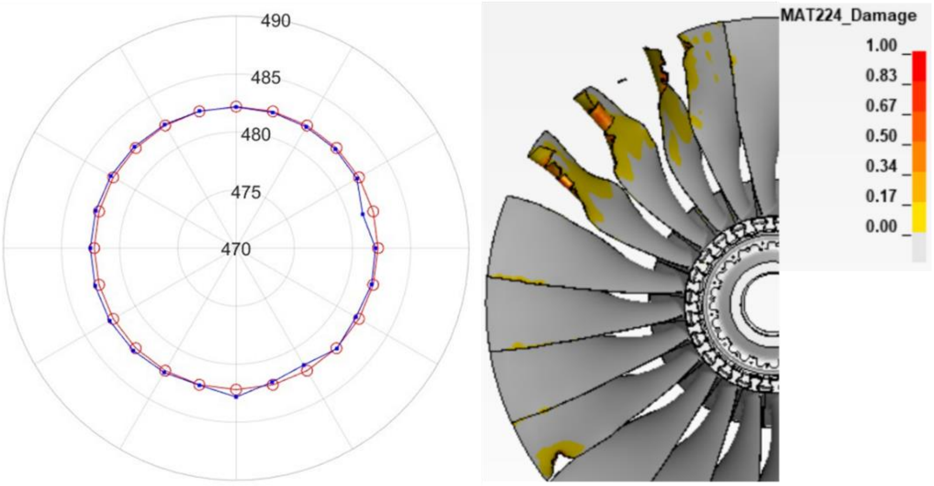

Figure 63. Center of mass of blades and fan model damage after UAS ingestion simulation HFS_LRV_HRS_45Y.

7.6.2 Flight Below 3048 m: MFS_LRV_HRS_45Y

This case corresponded to a UAS ingestion with 70% fan speed, low-relative translational velocity, high radial span location, and the 45 degree yaw orientation (see Figure 43). The kinematics of the ingestion are shown in Figure 64. The simulation is focused on understanding the damage in the fan and was therefore focused on the impact of the UAS and fan and was terminated around 8.25 ms.

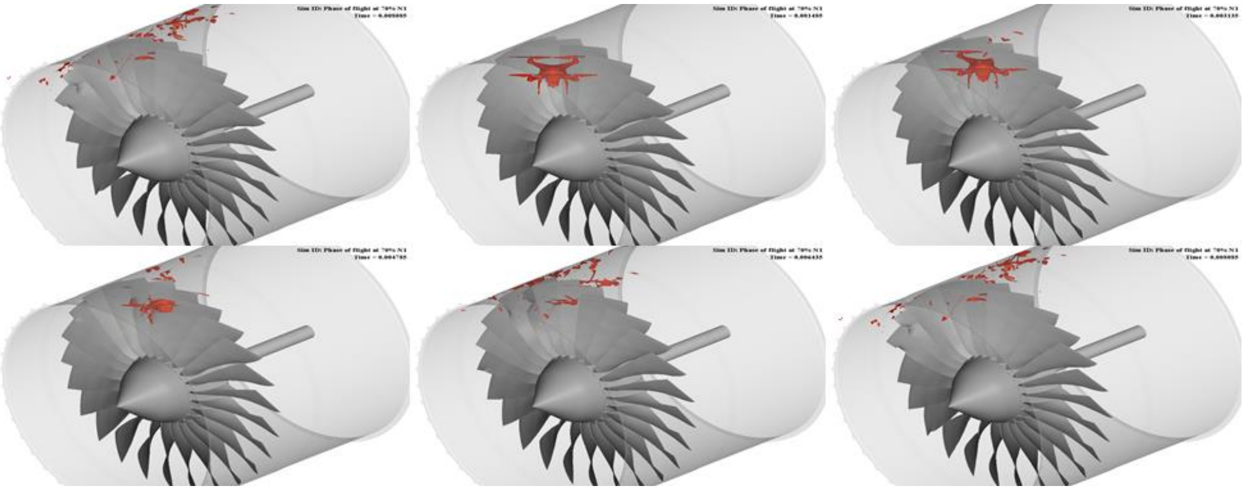

Figure 64. Kinematics of UAS ingestion simulation MFS_LRV_HRS_45Y.

The effective plastic strain in the fan at the end of one fan rotation is shown in Figure 65 (front and rear views).

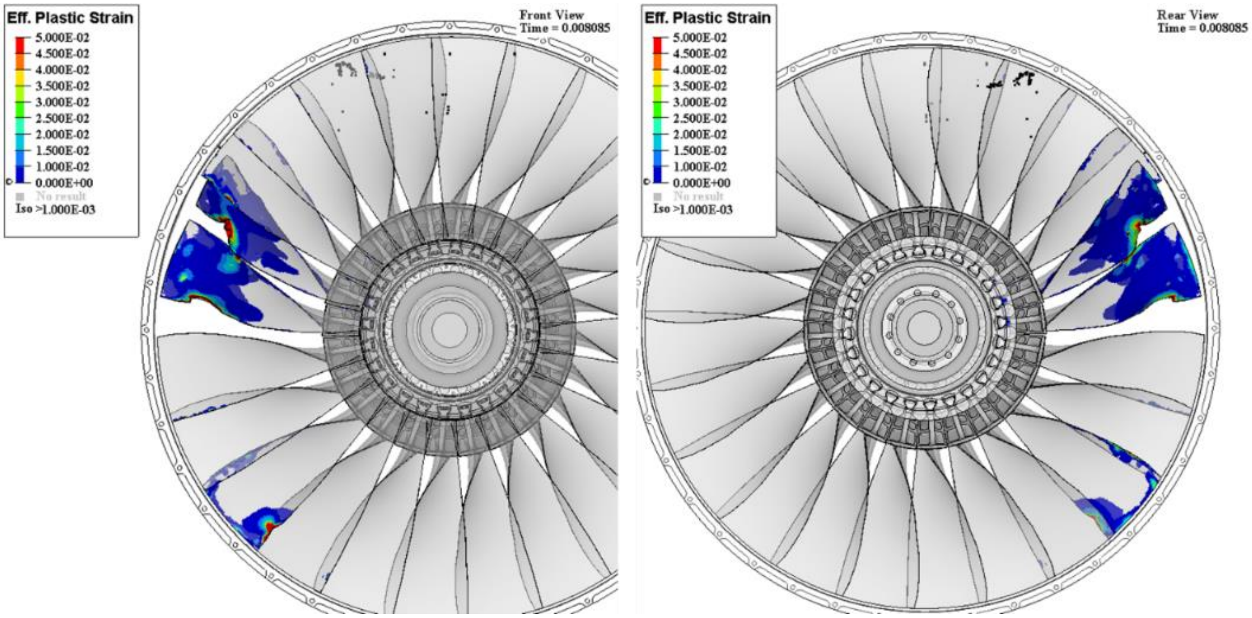

Figure 65. Effective plastic strain after UAS ingestion simulation MFS_LRV_HRS_45Y.

Each blade's radial center of mass pre- and post-ingestion are shown in Figure 66. The damage level D (defined in Section 7.2) in the damaged area of the fan model after the UAS ingestion is also shown. The damage clearly shows significant material loss on the leading edge of two blades, which corresponds to damage severity level 3, since the imbalance would be less than that of a loss of a full blade..

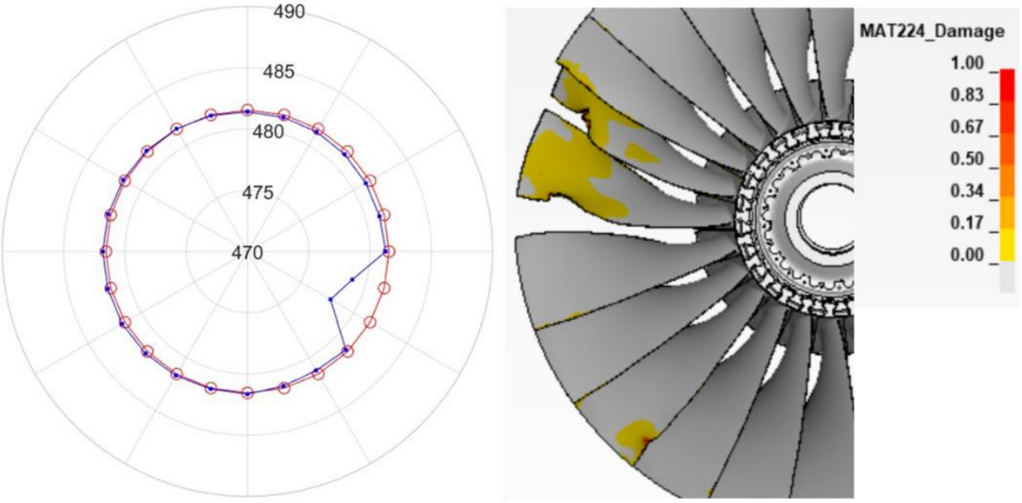

Figure 66. Center of mass of blades and fan model damage after UAS ingestion simulation MFS_LRV_HRS_45Y.

7.6.3 Summary of Phase of Flight Cases

A summary of the average forces in the disk, retainer and retention ring, damage in blades, and severity level for the reference cases, cases with the highest values for the ingestion studies and the phase of flight simulations are summarized in Table 10.

Table 10. Summary of phase of flight results and severity level evaluation.

Simulation ID	Average force in Disk (N)	Average force in retention ring (N)	Average force in retainer (N)	Damage in blade model	Severity level	Associated damage
FBO	**8.98E+05**	**6.10E+05**	**5.86E+05**	**0.04508**	Level 3	Significant material loss leading to an imbalance that is equal to a single blade loss and additional plastic deformation
HFS_HRV_HRS_ Bird_1.2kgs	2.95E+05	**3.41E+05**	**3.24E+05**	0.000692	Level 2	Cupping of leading edge of multiple blades
HFS_LRV_HRS_Nom	1.85E+05	3.04E+05	2.79E+05	**0.001763**	Level 3	Significant material loss on leading edge of multiple blades
HFS_HRV_HRS_45R	2.69E+05	3.35E+05	3.06E+05	0.001091	Level 3	Significant material loss on leading edge of multiple blades
HFS_HRV_HRS_90R	2.80E+05	3.34E+05	3.14E+05	0.000892	Level 3	Significant material loss on leading edge of multiple blades
HFS_HRV_HRS_45Y	2.81E+05	2.85E+05	2.67E+05	0.001509	Level 3	Significant material loss on leading edge of multiple blades
HFS_HRV_HRS_180R	**3.08E+05**	3.32E+05	3.13E+05	0.00112	Level 3	Significant material loss on leading edge of multiple blades
Phase of flight: Takeoff HFS_LRV_HRS_45Y	1.16E+05	2.00E+05	1.49E+05	0.001712	Level 3	Significant material loss on leading edge of multiple blades
Phase of flight: Flight below 3048 m MFS_LRV_HRS_45Y	1.18E+05	1.47E+05	1.27E+05	0.000627	Level 3	Material loss and deformation along leading of multiple blades

These two phases of flight simulations fall in line with the sensitivity study results. The level of damage and the damage to the fan indicate a damage severity level 3 is possible and quite likely in outer radial UAS impacts during takeoff and general flight below 3,048 m (10,000 ft).

8. KEY CONCLUSIONS AND RECOMMENDATIONS

The work presented in this cover report highlights the main results from each of the individual university Annexes, which describe the completion of three main tasks.

Task A: The OSU team worked closely with industry to develop an open fan model that is representative of the structural and vibratory features of high bypass ratio fans commonly used for commercial transport. The fan rig model consisted of the fan blades and disk, which were analyzed to ensure that it would meet stress loads when rotating at full speed (Section 5.4.2), bird ingestion requirements for a fan of its size (Section 5.4.3), and did not have any engine order one crossing on the Campbell diagram (Section 5.4.1). Each fan blade was held in place with a retention ring in the rear and a retainer in the front. The model was driven by a rigid shaft. For the boundary conditions for the fan model in this study, a bi-conic nose cone was connected to the disk through a flange, and a cylindrical casing encompassed the fan. Containment was not investigated in this work and a linear elastic material model was chosen for the casing to capture first-order effects and provide information about the expected loads transferred to the casing during the events. The work leveraged past FAA research programs development of a titanium alloy model for the fan material. Multiple meshes were generated for the fan model and could be used for different cases depending on the fidelity of the simulation and ingested object.

Task B: The research team worked closely with industry to help define relevant experiments that would represent a UAS ingestion (particularly with the representative fan rig model developed in this study). The UAH team carried out these challenging experiments that required accelerating key UAS components and a full UAS body up to high speeds and launching them at angled titanium test articles at precise locations. The experimental results included high speed video data from multiple views, digital image correlation data, strain gauge data, and load cell data. The experiments were done in close collaboration with the NIAR team who then analyzed the data, compared it with their computational analysis, and then updated their computational models to create a validated UAS model for engine ingestion conditions.

Task C: The OSU team worked closely with the NIAR team to ensure the compatibility and stability of ingestion simulations with their experimentally validated UAS model from Task B with the representative fan model from Task A. Moreover, the mesh sizing for the fan blades was determined based on the experimental validation with the UAS. The OSU team also worked closely with industry and research partners to determine what information should be extracted and analyzed from the UAS ingestion simulations. An initial sensitivity study was completed to identify the importance of a number of parameters during the ingestion such as the fan rotational speed, the relative translational velocity of the UAS and fan, the radial location of the UAS impact on the fan, and the orientation of the UAS during the impact. Based on the sensitivity study two phase of flight simulations were defined to study some of the expected worst case ingestions an aircraft might encounter during feasible flight conditions.

This work led to the development of a damage severity index for the fan rig assembly model subject to foreign object ingestion that consists of four levels. Level 1 is minor damage to the fan blades and would likely lead to minimal impact on engine performance. Level 2 is significant deformation of the blades with minimal loss of elements in the blades. Level 3 is deformation in blades and loss of blade material that leads up to an imbalance due to a single blade loss. Levels

1-3 are all within the engine certification envelope. Level 4 damage is loss of material leading to an imbalance greater than a single blade loss or disk crack initiation. The sensitivity study and all the phase of flight cases in this work resulted in severity levels between levels 1-3.

Overall, the damage severity in each of the cases tracks closely with the accumulation of the overall plastic strain in the whole fan (D_{fan} parameter defined in this work). The high fan speed case consistently has significantly more damage than the low fan speed, which is expected since the impacts happen at a much higher speed imparting more energy into the UAS and fan blades. The higher radial span impact causes significantly more damage than the lower radial span impact since at the higher radial span the relative velocity between the UAS and fan blades is much higher than at the lower radial span (which are severity level 1 or 2). All the high fan speed with high radial impact cases for the UAS ingestion are severity level 3 as opposed to the bird of the same mass which is severity level 2. The case that causes the most damage to the fan is the lower translational relative velocity scenario (with high fan speed and high radial span location). Finally, in comparing the orientations the 45-degree yaw orientation caused the most damage in the sensitivity study for the HFS_HRV_HRS condition.

The two phase of flight cases studied in this work focused on what were expected to be worst ingestion cases. For the take-off case, the worst-case impact was maximum rotational speed (100% N1), high radial span impact and a low relative translational velocity. The nominal orientation case for this condition was done in the sensitivity study and resulted in the worst damage. An additional take-off case with a 45 degree yaw orientation case was also conducted since that orientation caused the most damage in the HFS_HRV_HRS condition. This resulted in a slightly lower damage than the nominal orientation. It should be noted that the translational relative velocity and orientation are secondary factors in the damage level and depend on the other parameters of the ingestion. For the flight below 3,048 m (10,000 ft), corresponding to the mid-level rotational speed (70% N1), high radial span impact with the 45 degree yaw orientation case, and a low relative translational velocity, a significant but lower level of damage was observed. Both of the additional phase of flight simulations studied resulted in a severity level 3 damage, and were in line with the damage seen during the sensitivity study.

The completion of this research program provides an open representative fan rig model that can be used for additional foreign object ingestion studies in industry and academia to improve models and compare results through this work. Moreover, the UAS has been experimentally validated at the conditions of an ingestion and can be used in industry on their proprietary models to better understand the threat posed to their engines.

9. REFERENCES

[1] http://osc.edu/ark:/19495/f5s1ph73. Ohio Supercomputer Center. Columbus, OH: Ohio Supercomputer Center; 1987.

[2] Olivares G, Gomez L, Monteros JE, Baldridge R, Zinzuwadia C, Aldag T. Volume II – UAS Airborne Collision Severity Evaluation – Quadcopter. FAA; 2017.

[3] D’Souza K, Lyons T, Lacy T, Kota K. Volume IV: UAS Airborne Collision Severity Evaluation: Engine Ingestion. FAA; 2017.

[4] Lyons T, D'Souza K. Parametric Study of an UAV Ingestion into a Business Jet Size Fan Assembly Model. ASME Journal of Engineering for Gas Turbines and Power 2019;141(7).

[5] Haight S, Wang, L., Du Bois, P., Carney K., Kan C. D. Development of a Titanium Alloy Ti-6Al-4V Material Model Used in LS-DYNA. FAA.

[6] http://awg.lstc.com/tiki/tiki-index.php?page=MGD. LS-DYNA Aerospace Working Group Modeling Guidelines Document. 2016.

[7] Sinha SK, Turner KE, Jain N. Dynamic Loading on Turbofan Blades Due to Bird-Strike. Journal of Engineering for Gas Turbines and Power 2011;133.

[8] Lawrence C, Carney K. Simulation of Aircraft Engine Blade-out Structural Dynamics. NASA Glenn Research Center; 2001.

[9] Dewhurst TB. The Impact Load on Containment Rings During a Multiple Blade Shed in Aircraft Gas Turbine Engines. International Gas Turbine and Aeroengine Congress and Exposition. Orlando, FL; 1991.

[10] Stepanov GV. Speed of Propagation of Elasto-Plastic Shock Waves in Metals. Institute for Study of Strength of Materials (Translated from Problemy Prochnosti) 1971;2(109-112).

[11] D’Souza K, Sirivolu D, Wong M, Kurstak E. Annex A to Task A17: OSU Representative Fan Model and sUAS Ingestion Studies. 2023.

[12] CFM. Training Manual CFM56-5B, Basic Engine. 2000.

[13] Hammer JT. Plastic Deformation and Ductile Fracture of Ti-6Al-4V under Various Loading Conditions. FAA Report DOT/FAA/TC-TT14/2; 2014.

[14] LS-DYNA Keyword User’s Manual Vol. 1. Livermore, California; 2016.

[15] http://awg.lstc.com/tiki/tiki-index.php?page=Resources. LS-DYNA Aerospace Working Group *Mat_224 User Guide. 2016.

[16] Olivares G, Gomez L, Ly H. Annex B to Task A17: NIAR/WSU sUAS Numerical Model Validation (Component and Full-Scale Level) for Engine Ingestion Analysis. 2023.

[17] Duling C, Zweiner M, Arteburn D. Annex C to Task A17: UAH High Speed Impacts of Full sUAS and Components with Angled Plates 2023.

[18] Seidt JD. Part 3: Plastic Deformation and Ductile Fracture of 2024 Aluminum under Various Loading Conditions. Development of a New Metal Material Model in LS-DYNA: FAA Report DOT/FAA/TC-13/25, P3; 2014.

[19] https://awg.lstc.com/tiki-index.php?page=Material+Parameter+Sets. LS-DYNA Aerospace Working Group *Mat_224 User Guide. 2016.

[20] Sengoz K, Kan S, Eskandarian A. Development of a Generic Gas Turbine Engine Fan Blade-out Full Fan Rig Model. FAA Report DOT/FAA/TC-14/43; 2015.

[21] FAA. Wildlife Strikes to Civil Aircraft in the United States, 1990 - 2021. FAA; 2022.

[22] FAA. Code of Federal Regulations, Part 33 - Airworthiness Standards: Aircraft Engines. US; 2011.

[23] https://awg.lstc.com/tiki-index.php?page=Test+Case+Suite. Awg Erif Test Case Suite Overview. LS-DYNA Aerospace Working Group.

[24] Lyons T, Sirivolu D, D'Souza K. Stress State Characterization for a Generic Titanium Fan During Bird Ingestion. AIAA Journal 2022:1-12.

[25] Vintilescu IV. Explicit Finite Element Modeling of Multilayer Composite Fabric for Gas Turbine Engine Containment Systems, Phase II - Part 4: Model Simulation for Ballistic Tests, Engine Fan Blade-out, and Generic Engine. FAA Report DOT/FAA/AR-08/37,P4; 2009.